

DEVELOPMENT OF NEW HIGH ENTROPY ALLOYS

FOR BRAZING OF NI-BASE

SUPERALLOYS

by

Minrui Gao

A thesis submitted to the Faculty and the Board of Trustees of the Colorado School of Mines in partial fulfillment of the requirements for the degree of Master of Science (Metallurgical and Materials Engineering).

Golden, Colorado

Date \_\_\_\_\_

Signed: \_\_\_\_\_  
Minrui Gao

Signed: \_\_\_\_\_  
Dr. Zhenzhen Yu  
Thesis Advisor

Golden, Colorado

Date \_\_\_\_\_

Signed: \_\_\_\_\_  
Dr. Angus Rockett  
Professor and Head  
George S. Ansell Department of Metallurgical and Materials Engineering

## ABSTRACT

High entropy alloys (HEAs), also called multi-principal component alloys, are novel alloys containing at least five elements with an atomic percent ranging between 5% and 35%. HEAs have attracted attention due to their unique properties such as high strength, good ductility, and high resistance to corrosion and wear. However, applications of HEAs still need to be explored.

In this study, a new HEA filler metal ( $\text{Fe}_5\text{Co}_{20}\text{Ni}_{20}\text{Mn}_{35}\text{Cu}_{20}$ ) was designed for brazing of Inconel 600 alloy. Thermodynamic simulation, using Thermo-Calc software, was performed to design the composition of the HEA. A face-centered cubic (FCC) crystal structure was achieved that balanced strength, ductility and a melting range lower than the solidus temperature of Inconel 600. Differential thermal analysis (DTA) confirmed that the as-cast HEA had a solidus temperature of 1080 °C and a liquidus temperature of 1150 °C, which were in good agreement with the melting range predicted by Thermo-Calc using the newly published “HEA 1.0” database. Only a 10 °C discrepancy was identified. Through wetting angle tests at various temperatures, the optimum brazing temperature for this HEA was determined to be 1200 °C. The as-cast HEA button was cold rolled into foils with different thickness ranging from 50 to 300  $\mu\text{m}$  for brazing tests. The brazing time was varied from 15 to 120 min. Effect of brazing time and foil thickness on the shear strength of the brazed joint were evaluated. A maximum shear strength of 530 MPa was achieved with a brazing time of 90 min and a foil thickness of 300  $\mu\text{m}$ . With a fixed brazing time of 90 min, the shear strength reduced continuously to a minimum value of 302 MPa with decreasing foil thickness. Microscale digital image correlation (DIC) was used to map localized strain distribution at the brazed joints during the shear test. Moreover, metallurgical characterizations including optical microscopy (OM), scanning electron microscopy (SEM), and energy dispersive spectroscopy (EDS) were carried out at the interface to explain the observed mechanical behaviors.

In addition, interface reactions between as-cast, oxidized  $\text{FeCoNi}(\text{AlSi})_{0.2}$  HEA and aluminum melt at 700 °C were investigated to evaluate the alloy’s potential for use as mold material for casting of aluminum alloys. It was found that, compared with Fe, the as-cast and oxidized HEA have a thinner reaction products layer. Oxidized HEA had the thinnest layer. Pre-oxidation treatment of HEA is an effective and economical way to improve the mold material’s resistance to aluminum melt attack.

## TABLE OF CONTENTS

Abstract .....	iii
List of Figures .....	vi
List of Tables .....	ix
Acknowledgements .....	x
Chapter 1: Introduction .....	1
Chapter 2: Literature review .....	1
2.1 Design and phase formation of HEA .....	3
2.2 Properties of HEAs .....	8
2.3 Fabrication, preparation and applications of HEAs .....	11
2.4 Properties and Welding of Ni-base superalloys .....	19
2.5 Brazing of Ni-base superalloy .....	21
2.5.1 Ag, Au-based filler metals for brazing of Ni-base superalloys .....	21
2.5.2 Ni-based filler metals for brazing of Ni-base superalloys .....	21
2.5.3 Cu-based filler metals for brazing of Ni-base superalloys .....	23
2.5.4 Advantages of HEA as filler metal for brazing of Ni-base superalloy .....	23
Chapter 3: Experiments .....	25
3.1 Brazing of Inconel 600 alloy by Fe <sub>5</sub> Co <sub>20</sub> Ni <sub>20</sub> Mn <sub>35</sub> Cu <sub>20</sub> HEA filler .....	25
3.1.1 Design of HEA filler .....	25
3.1.2 Arc melting fabrication of HEA .....	28
3.1.3 HEA/Inconel 600 wetting angle test .....	29
3.1.4 Fabrication of HEA foils .....	31
3.1.5 Brazing of Inconel 600 alloy by HEA filler foils .....	31
3.2 Interface reaction between HEA and aluminum melt .....	33
3.2.1 Arc melting fabrication of HEA .....	33
3.2.2 Oxidation of HEA .....	34
3.2.3 HEA-aluminum melt interface reaction .....	35
Chapter 4: Brazing of Inconel 600 by HEA filler foil .....	36
4.1 Design of the composition of HEA filler .....	36
4.2 Fabrication and characterization of Fe <sub>5</sub> Co <sub>20</sub> Ni <sub>20</sub> Mn <sub>35</sub> Cu <sub>20</sub> HEA .....	40
4.3 Wetting angle test between Inconel 600 and HEA .....	46
4.4 Characterization of joints brazed by HEA filler foil .....	49

4.4.1 Effect of brazing time on the shear strength of the brazed joint .....	49
4.4.2 Effect of filler foil thickness on the shear strength of the brazed joint .....	67
Chapter 5: HEA/Al melt interface reaction.....	73
5.1 Selection of the HEA composition.....	73
5.2 Fabrication and characterization of FeCoNi(AlSi) <sub>0.2</sub> HEA.....	74
5.3 Effect of temperature on the oxidation layer on the surface of FeCoNi(AlSi) <sub>0.2</sub> HEA.....	78
5.4 Interface reaction between Al melt and as-cast HEA, and oxidized HEA.....	82
Chapter 6: Research summary and conclusions.....	86
Chapter 7: Future work .....	88
7.1 Development of new HEA fillers.....	88
7.2 Development of new phase diagram calculation software.....	88
7.3 Brazing of Ni-bas superalloys, ceramics or other alloys.....	88
7.4 New method to test the shear strength of the brazed joint .....	88
7.5 Microstructure characterization of the brazed joint .....	89
7.6 Development of HEA nanoscale powder for brazing .....	89
7.7 Development of mold materials for Al alloy casting .....	89
References.....	90
Appendix A: Supplemental electronic files .....	98

## LIST OF FIGURES

Figure 2.1 Schematic diagram of the arc melting set-up .....	15
Figure 2.2 Schematic diagram of the Bridgman solidification set-up.....	16
Figure 3.1 Phase diagram of $Fe_xCo_{20}Ni_{20}Mn_yCu_{20}$ system calculated by Thermo-Calc using HEA 1.0 database.....	25
Figure 3.2 Scheil diagram of the $Fe_5Co_{20}Ni_{20}Mn_{35}Cu_{20}$ system calculated by Thermo-Calc using HEA 1.0 database.....	26
Figure 3.3 Photograph showing positions of the HEA samples and Ti buttons in arc melting furnace .....	29
Figure 3.4 Photographs of (a) the arc melting furnace and (b) argon gas tank used in this study .....	29
Figure 3.5 Temperature-time curves of wetting angle tests at 1160, 1180, 1200,1250 °C for 30 min .....	30
Figure 3.6 Top view of the wetting angle sample.....	30
Figure 3.7 Rolling mill used to fabricate HEA foils in the physical metallurgy lab.....	31
Figure 3.8 Sample arrangement of the brazing tests. HEA foil is used as filler metal and Inconel 600 alloy is used as the base metal .....	32
Figure 3.9 Temperature-time curves of brazing test at 1200 °C for 15, 30, 45, 60, 90, and 120 min.....	32
Figure 3.10 Schematic diagram of brazed sample shear test .....	33
Figure 3.11 Temperature-time curves for oxidation of as-cast $FeCoNi(AlSi)_{0.2}$ HEA .....	34
Figure 3.12 Temperature-time curves of the interface reactions between as-cast HEA, oxidized HEA, pure Fe and aluminum melt .....	35
Figure 4.1 Phase diagram for $Fe_xCo_{20}Ni_{20}Mn_yCu_{20}$ system calculated by Thermo-Calc using HEA 1.0 database.....	39
Figure 4.2 (a-d) Microstructure showing the microstructure of as-cast $Fe_5Co_{20}Ni_{20}Mn_{35}Cu_{20}$ HEA .....	42
Figure 4.3 XRD curve of (a) as-cast $Fe_5Co_{20}Ni_{20}Mn_{35}Cu_{20}$ HEA and (b) $FeCoNi(AlSi)_x$ ( $x:0-0.8$ ) <sup>156</sup> .....	42
Figure 4.4 (a) Microstructure and (b-g) EDS mapping of the five elements in as-cast $Fe_5Co_{20}Ni_{20}Mn_{35}Cu_{20}$ HEA.....	43
Figure 4.5 DTA curve of as-cast $Fe_5Co_{20}Ni_{20}Mn_{35}Cu_{20}$ HEA (the sample is heated in argon gas atmosphere at a rate of 15 °C/min) .....	45
Figure 4.6 Engineering stress-strain curves during compression tests of as-cast $Fe_5Co_{20}Ni_{20}Mn_{35}Cu_{20}$ HEA (geometry: $\varnothing 2 \times 4$ mm) in a strain rate of $4 \times 10^{-4}$ /s on Alliance Machine.....	45
Figure 4.7 True stress-strain curves during compression tests of as-cast $Fe_5Co_{20}Ni_{20}Mn_{35}Cu_{20}$ HEA (geometry: $\varnothing 2 \times 4$ mm) in a strain rate of $4 \times 10^{-4}$ /s on Alliance Machine.....	46
Figure 4.8 Spreading morphologies observed after wetting angle tests between $Fe_5Co_{20}Ni_{20}Mn_{35}Cu_{20}$ HEA and Inconel 600 substrate at different temperature (a) 1160°C (b) 1180°C (c) 1200°C (d)1250°C ...	48
Figure 4.9 (a)Macrostructure and (b) measurement of wetting angle on both of left and right sides of 1200°C wetting angle test sample .....	48
Figure 4.10 (a-c) Schematic diagram of the hardness (d)hardness distribution in different areas of the 1200°C wetting angle test sample between $Fe_5Co_{20}Ni_{20}Mn_{35}Cu_{20}$ and Inconel 600 alloy substrate.....	49

Figure 4.11 Microstructure of the joint brazed at 1200 °C for by a filler foil with a thickness of 300µm for different brazing time (A1-A5)30min, (B1-B5)60min, (C1-C5)90min, and (D4-D5)120min.....	56
Figure 4.12 EDS Mapping of elements in joints brazed at 1200 °C for 90 min using HEA filler foil with different thicknesses (300, 200, 100, and 50 µm).....	57
Figure 4.13 EDS line scanning of joint brazed at 1200 °C for different time (30, 90, and 120 min) using 300 µm HEA filler foils. (A1-A2) 30min (A2-B2) 90min (A3-B3) 120min .....	58
Figure 4.14 Phase diagram for $Fe_xCo_{20}Ni_yMn_{35}Cu_{20}$ system ( $x+y=25$ ) calculated by Thermo-Calc using HEA 1.0 database.....	59
Figure 4.15 Phase diagram for $Fe_xCo_{20}Ni_{20}Mn_{35}Cu_y$ system ( $x+y=25$ ) calculated by Thermo-Calc using HEA 1.0 database.....	59
Figure 4.16 Phase diagram for $Fe_xCo_yNi_{20}Mn_{35}Cu_{20}$ system ( $x+y=25$ ) calculated by Thermo-Calc using HEA 1.0 database.....	60
Figure 4.17 Shear strength of the Inconel 600/ $Fe_5Co_{20}Ni_{20}Mn_{35}Cu_{20}$ HEA/Inconel 600 braze joint of different brazing time (15, 30, 45, 60, 90, and 120 min, filler metal foil thickness and brazing temperature were fixed at 300 µm and 1200 °C).....	60
Figure 4.18 (a, b) Hardness distribution in joint brazed at 1200 °C for 30 min by $Fe_5Co_{20}Ni_{20}Mn_{35}Cu_{20}$ filler with a thickness of 300 µm. (c)Hardness distribution in different areas of the brazed sample (d)Schematic diagram of the hardness test .....	61
Figure 4.19 (a, b) Hardness distribution in joint brazed at 1200 °C for 90 min by $Fe_5Co_{20}Ni_{20}Mn_{35}Cu_{20}$ filler with a thickness of 300 µm. (c)Hardness distribution in different areas of the brazed sample (d)Schematic diagram of the hardness test .....	62
Figure 4.20 (a, b) Hardness distribution in joint brazed at 1200 °C for 120 min by $Fe_5Co_{20}Ni_{20}Mn_{35}Cu_{20}$ filler with a thickness of 300 µm. (c)Hardness distribution in different areas of the brazed sample (d)Schematic diagram of the hardness test.....	63
Figure 4.21 Hardness variation of the joints brazed by HEA filler foil with a thickness of 300µm for different time. (a) 30min (b)90min (c)120min.....	64
Figure 4.22 Cu-Mn phase diagram with the composition of Cr-Mn rich phase observed.....	65
Figure 4.23 Cr-Mn phase diagram with the composition of Cr-Mn rich phase observed.....	65
Figure 4.24 Strain distribution during shear test of the sample brazed at 1200 °C for 60 min by HEA filler foil with a thickness of 50 µm. (a, b) strain distribution in the whole brazed sample (c, d, e) strain distribution in the local area marked in (a). .....	66
Figure 4.25 Microstructure of the joint brazed at 1200 °C for 90 min by a filler foil with a thickness of (A1-A5)300 µm, (B1-B5)200 µm, (C1-C5)100 µm, and (D4-D5)50 µm.....	69
Figure 4.26 EDS element maps in joints brazed at 1200 °C for 90 min using HEA filler foil with 300, 200, 100, and 50 µm thicknesses .....	70
Figure 4.27 EDS line scanning of joint brazed using HEA filler foil with different thicknesses when brazing temperature and brazing time are fixed at 1200 °C and 90 min. (A1-A2)300µm (B1-B2)200µm (C1-C2)100µm (D1-D2)50µm .....	71
Figure 4.28 Shear strength of the Inconel 600/ $Fe_5Co_{20}Ni_{20}Mn_{35}Cu_{20}$ HEA/Inconel 600 joint brazed by 50, 100, 200, and 300 µm thick foils with brazing time and brazing temperature fixed at 90min and 1200 °C. ....	72
Figure 5.1 OM images showing the microstructure of the as-cast $FeCoNi(AlSi)_{0.2}$ HEA.....	76

Figure 5.2 XRD curve of the as-cast FeCoNi(AlSi) <sub>0.2</sub> HEA.....	76
Figure 5.3 DTA curve of the as-cast FeCoNi(AlSi) <sub>0.2</sub> HEA.....	77
Figure 5.4 Engineering stress-strain curves of the as-cast FeCoNi(AlSi) <sub>0.2</sub> HEA during compression tests on Alliance and Instron machine. Strain rate is fixed at 4×10 <sup>-4</sup> /s.....	77
Figure 5.5 True stress-strain curves of the as-cast FeCoNi(AlSi) <sub>0.2</sub> HEA during compression tests on Alliance and Instron machine .....	78
Figure 5.6 (a-c) Microstructure and composition of FeCoNi(AlSi) <sub>0.2</sub> HEA after oxidation at 800 °C for 5 hours in the regular furnace. The composition of the as-cast HEA is Fe:29.4at%, Co:29.4at%, Ni:29.4at%, 29.4at%, Al: 5.9at%, Si: 5.9at%.....	80
Figure 5.7 (a-c)Microstructure and composition of FeCoNi(AlSi) <sub>0.2</sub> HEA after oxidation at 1000C after 5 hours in the regular furnace. The composition of the as-cast HEA is Fe:29.4at%, Co:29.4at%, Ni: 29.4at%, Al: 5.9at%, Si: 5.9at%.....	81
Figure 5.8 (a-d) Microstructure and composition of the interface between as-cast HEA and solidified pure Al .....	83
Figure 5.9 (a-b) Microstructure of the interface between pure Fe and solidified Al (c) average thickness of reaction layer varying with immersion time for pure Fe, FeCoNiMnCr (5-HEA) and FeCoNiCrMnAl (6-HEA) <sup>17</sup> .....	84
Figure 5.10 (a-c) Microstructure and composition of the interface between oxidized (800 °C, 5h) HEA and solidified pure Al .....	85

## LIST OF TABLES

Table 2.1 Mechanical properties and phases formations of refractory HEAs. YS is yield strength and PS means peak strength) .....	17
Table 2.2 Melting ranges of typical HEAs .....	24
Table 3.1 Mixing enthalpy, mixing entropy, atomic size difference, linear thermal expansion and valance electron concentration for Fe <sub>5</sub> Co <sub>20</sub> Ni <sub>20</sub> Mn <sub>35</sub> Cu <sub>20</sub> HEA system.....	27
Table 4.1 Mixing enthalpy ( $\Delta H_{mix}$ ), mixing entropy( $\Delta S_{mix}$ ), atomic size difference ( $\delta$ ), linear thermal expansion coefficient and valance electron concentration of Fe <sub>5</sub> Co <sub>20</sub> Ni <sub>20</sub> Mn <sub>35</sub> Cu <sub>20</sub> system. ....	40
Table 5.1 Mixing enthalpy ( $\Delta H_{mix}$ ), mixing entropy ( $\Delta S_{mix}$ ), atomic size difference ( $\delta$ ), linear thermal expansion coefficient and valance electron concentration of FeCoNi(AlSi) <sub>0.2</sub> HEA system .....	74

## ACKNOWLEDGEMENTS

I would like to acknowledge and thank those who helped me to finish my master thesis.

My advisor, Dr. Zhenzhen Yu, who makes students think how to do research in high efficiency.

Dr. Stephen Liu, who has rich experience in welding and brazing and provides many useful suggestions to my research.

Dr. Kaufman, a questioner who makes me think deeply.

My fellow students of CWJCR, their advice, help and suggestions helped me to make my research easier and efficiency.

Fellow professors and students from other centers and other departments, their help and support made my research possible. For example, Dr.Kip Findley and Dr. Steve Van Hall's help on my shear test.

The Center for Welding, Joining, Coating research (CWJCR), many thanks for providing the funding for my research.

My family and friends, whose support and encouragement helped me finish the study and research.

And to my girlfriend, Yaping, who helped me overcome the most difficult time in my second year.

## CHAPTER 1

### INTRODUCTION

Different from conventional alloys based on one or two principal elements, HEAs (HEA) are defined as novel alloys containing at least five main elements with an atomic percent ranging from 5% to 35%. It was first defined by Yeh et al<sup>1</sup> in 1995 and named as multicomponent alloys by Cantor et al<sup>2</sup> in 2004. It has attracted much attention due to the combination of excellent properties such as good thermal stability, high strength, high hardness, high resistance to corrosion, oxidation and wear.<sup>3,4,5,6,7</sup>

Ni-base superalloys are complex materials with the ability to maintain their high strength, good ductility, high resistance to corrosion and oxidation at elevated temperatures.<sup>8</sup> They have been widely used in many different fields such as aerospace, marine propulsion, submarines and nuclear reactors, and powder generation industries.<sup>9</sup> It is of significance to develop a feasible, reliable and economical technique to join Ni-base superalloys. Fusion welding typically causes cracking issues in joining Ni-base superalloys, for example liquidation cracking and solidification cracking.<sup>10,11,12,13,14</sup> Moreover, distortion and residual stress is inevitably induced by fusion welding, which is not desirable for Ni-base superalloy components with sophisticated geometries. In comparison, brazing technique joins two pieces of metals together by melting the filler metal below the solidus temperature of the base metals,<sup>15</sup> which potentially avoids the cracking issues and distortion associated with solidification and high heat input. In addition, brazing has also been used to repair narrow/wide gaps in the components made of Ni-base superalloy in order to prolong the service life of components.<sup>16</sup> The existing commercial brazing alloys are mainly Ag-based and Ni-base alloys containing melting point depressant elements such as Si, P and/or B.<sup>17,18,19,20,21</sup> The silver-based brazing alloys are relatively expensive and the melting point depressants could form brittle boride, silicide or phosphide, which are detrimental to the mechanical properties of the brazed joint.

HEAs with a simple phase structure, a good balance between strength and ductility, could be designed to achieve a similar melting range with the commercial brazing alloys without adding melting point depressant elements. It is an excellent candidate as filler metal for brazing of Ni-base superalloys. In this study, a new HEA consisted of FCC phases was designed with a narrow melting range and similar thermal expansion coefficient to Inconel 600 alloy with the aid of thermodynamic simulation using ThermoCalc software. It is rolled into filler foils for brazing of Inconel 600 alloy. Effects of brazing time and foil thickness on the shear strength of the brazed joints are evaluated.

On the other hand, HEA's potential to be used as a mold material for aluminum alloy casting is also evaluated in this study. Metallic materials such as ferrous alloys, titanium alloys, nickel alloys can be used as the die or crucible materials for the low melting point metallic melt during casting or hot dipping process.<sup>22,23,24</sup> Ferrous alloy is the most popular die material for production of aluminum alloy components. However, severe reactions between aluminum melt and ferrous alloys are always observed. Different Al-Fe intermetallic such as  $\text{FeAl}_2$ ,  $\text{FeAl}_3$ ,  $\text{Fe}_2\text{Al}_5$  with different morphologies have been reported.<sup>25,26</sup> Such reactions reduce the service life of the die and the quality of the aluminum products. There are rising interests in identifying new candidates for die materials. The thermal stability and oxidation resistance of HEA makes it a potential candidate die or container material for Al melt. In addition, the effectiveness of surface treatments on the developed HEA, such as surface coating or surface oxidation on improving the heat resistance were evaluated. In this work, a new HEA was designed for this purpose. Effect of temperature on its microstructure and composition of the oxidation layer was evaluated. The reactions between pure Fe/Al, as cast HEA/Al, oxidized HEA/Al are compared to evaluate the feasibility of using HEA as a die material for aluminum casting.

## CHAPTER 2

### LITERATURE REVIEW

#### 2.1 Design and phase formation of HEA

HEAs are defined as solid solution alloys which have at least five main elements with atomic percent between 5% and 35%, to distinguish them from conventional alloys which are usually based on one or two main elements, It was first defined by Yeh et al<sup>27</sup> in 1995 and named as multicomponent alloys by Cantor et al<sup>28</sup> in 2004. HEA has attracted much attention because of its better properties than conventional alloys such as higher hardness, strength, oxidation resistance, corrosion resistance, fatigue strength, wear resistance and thermal stability.<sup>29,30,31,32,33</sup>

Ma et al<sup>34</sup> found that the addition of Nb into AlCoCrFeNiNbx could result in the formation (CoCr)Nb type laves intermetallic phase. The microstructure observation shows that the volume fraction of Laves phase increases from 0, 4.25%, 21.10%, 41.55% to 48.69% while x increases from 0, 0.1, 0.25, 0.5 to 0.75, respectively. XRD test shows laves phase appears when x reaches 0.25. The ductility of AlCoCrFeNiNbx decreases with the increase of x. It also turns out that the phase formation of multi-components alloys could be predicted excellently by introducing the definition of  $\delta$ .  $\delta$  evaluates the atomic size difference. It increases with the increase of x.  $\delta$  exceeds 6% when x is larger than 0.25 and according to XRD test laves phase appears when x reaches 0.25, which is consistent with the HEA principle proposed by Liaw et al<sup>35</sup>. The elongation of AlCoCrFeNiNbx from compressive test ( $\phi 5 \times 10$  mm, strain rate:  $2 \times 10^{-4}$ /s) decreases from 27.5% to 10% when x increases from 0 to 0.5. It is also found by Zhou et al<sup>36</sup> that the phase structure of AlCoCrFeNiTix will change from BCC to BCC+Fe<sub>2</sub>Ti Laves when x reaches 1.5. The elongation of AlCoCrFeNiTix from compressive test ( $\phi 5 \times 10$  mm, strain rate:  $10^{-4}$ /s) decreases from 20% to 4.8% when x increases from zero to 1.5.

The topic of how to predict the phase formation of multicomponent alloys has been studied for many years. Hume-Rothery rules, considering the atomic radius, crystal structure, valence and electronegativity of two elements were first proposed and used to predict the phase formation of binary systems<sup>37,38,39,40,41,42</sup>. Later in 1970s the Miedema calculation was proposed to calculate the heats of formation of intermetallic alloys using two parameters, which are electronegativity and electron cell boundary density<sup>43</sup>. It shows a good capability to predict the solubility in case of divalent solvents<sup>44</sup> and even demonstrates a better capability while bringing atomic size in addition to electronegativity and electron cell boundary density<sup>45</sup>. It has been extended to multicomponent systems to distinguish the phase formation domains of amorphous phase and solid solutions.

In early stage of exploring HEAs, most of discussions on phase formation of HEAs are based on the factors such as atomic size, crystal structure, atomic pairs formation enthalpy<sup>46,47,48,49</sup>. However, there were no quantitative criteria to predict the phase formation of multicomponent alloys. Both HEAs and BMGs are multicomponent while BMGs were developed much earlier than HEAs, so efforts have been made to correlate the solid solution formation of HEAs and glass formation of BMGs. Recently thermodynamic parameters like mixing enthalpy ( $\Delta H_{mix}$ ), mixing entropy ( $\Delta S_{mix}$ ), mismatch entropy, atomic size difference ( $\delta$ ) were used to predict the formation of solid solutions, intermetallic and amorphous phases in multi-component alloys<sup>50,51,52,53,54,55,56,57,58,59</sup>. Criteria based on these parameters have been proposed. Although there is some inconsistency between different publications, they basically provide the guidelines to design the composition of multicomponent alloys which tends to form HEAs with solid solution phase. Opposite to the observations above, Otto et al.<sup>60</sup> found the phase formation in HEAs is determined by free energy minimization, neither the mix enthalpy nor mixing entropy independently. In addition, it was also found by Raghavan et al.<sup>58</sup> above that solid solution is preferred if the ration of configuration entropy to fusion entropy ( $\Delta S_{conf}/\Delta S_{fusion}$ ) is larger than 1 and 1.2 in equiatomic and nonequiatomic alloys. It was also shown that BCC structure has more tolerance with the atomic size difference than FCC structure. The effect of some special alloying element on the phase formation of multicomponent alloys are also studied. For example, a phase structure transition from FCC to BCC in Al-Co-Cr-Cu-Fe-Ni-Ti and Al-Co-Cr-Cu-Fe-Ni HEAs when the Al is increased was observed by Wang et al.<sup>57</sup> and Sriharitha et al.<sup>61</sup>. Pettifor map based on the Mendeleev number, is also introduced into the prediction of formation of intermetallic, quasicrystal and glass<sup>62,63,64,65</sup>. Especially Villars et al.<sup>66</sup> reported that compared to atomic number, Mendeleev number is higher effective to predict the former or non-former in binary, ternary and quaternary systems.

The phase selection laws are very useful for the composition design of HEAs. Except the laws above, there is also another way to approach single phase HEA<sup>67</sup>. For example, there is a multicomponent alloy system consisted of  $\alpha$ -phase,  $\beta$ -phase and some other phases. Then the single  $\alpha$ -phase HEA can be fabricated by just using the composition of  $\alpha$ -phase detected from (energy dispersive spectrometer) EDS or (electron probe microanalyzer) EPMA. Also, in order to achieve HEAs with excellent properties, the concentration of each element can be adjusted while still maintaining the single phase structure.

Yeh et al.<sup>68</sup> found that the addition of Al into CoCrCuFeNi HEA could lead to the transition of phase structure from FCC to BCC. For  $Al_xCoCrCuFeNi$ , BCC phase starts to appear when  $x=1.0$  and completely transfers into BCC structure.  $Al_{0.5}CoCrCuFeNi$  and  $CoCrCuFeNi$  have a single FCC solid solution. For  $Al_xCoCrCuFeNi$ , the yielding strength decreases with the increase of  $x$  because BCC solid solution usually has a higher strength than FCC solid solution.

The formation mechanism of HEA has been summarized and reported by Zhang et al.<sup>69</sup>.  $\delta$  and  $\Omega$  are defined to evaluate the formability of a multi-component alloy.

$$\Delta\Delta S_{mix} = \sum_{i=1}^n -RC_i \ln C_i \quad \text{Equation 1}$$

$$\Delta H_{mix} = \sum_{i=1, i \neq j}^n -4C_i C_j \Delta H_{mix}^{AB} \quad \text{Equation 2}$$

$$\Omega = |\Delta S_{mix}| / \Delta H_{mix} \quad \text{Equation 3}$$

$$r = \sum_{i=1}^n C_i r_i \quad \text{Equation 4}$$

$$\delta = \sqrt{\sum_{i=1}^n C_i \left(1 - \frac{r_i}{\sum_{i=1}^n C_i r_i}\right)^2} \quad \text{Equation 5}$$

$\delta$  evaluates the atomic size difference;  $C_i$  is the molar fraction of element  $i$ ;  $r_i$  is the atomic radius of element  $i$ ;  $r$  is the average atomic size of the HEA;  $\Delta H_{AB}^{mix}$  is the change of enthalpy before and after the mixing of A and B;  $T$  is the temperature;  $\Delta H_{mix}$  is the change of enthalpy before and after the mixing of the multi-component alloy and  $\Delta S_{mix}$  is the change of entropy before and after the mixing of the multi-component alloy.  $\Omega$  evaluates the change of Gibbs free energy before and after the mixing of the multi-component alloy. In order to form a HEA, the multi-component alloy should have a  $\delta \leq 6\%$  and  $\Omega \geq 1.1$ .

Although there are several phase formation laws for developed to guide the composition design of HEA, it is still necessary to have more quantitative prediction methods. The Integrated Computational Materials Engineering technology, has been an effective tool to identify and search for new HEAs. Currently there are several types of simulation or calculation methods, which are (phase diagram calculation) CALPHAD, Ab-initio calculation, (Molecular dynamics) MD simulation, (Monte-Carlo) MC simulation and phase field modeling.

The (phase diagram calculation) CALPHAD technique has been developed since 1956<sup>70</sup>. Efforts have been made to use the CALPHAD software such as Thermo-Calc, FactSage to predict phase formation in HEAs, some of the results confirms with the experimental results while some don't<sup>71, 72, 73, 74, 75</sup>. Till now more database with sufficient thermodynamic parameters is required. Ab-initio calculation is also a powerful tool to predict the properties and behaviors of multicomponent alloys by directly calculating the electronic structure of atoms. By using Ab-initio calculation, it has been investigated that how the lattice parameter and phase formation will change with the variety in composition<sup>76, 77</sup>. It has also been hired to predict the properties of HEA such as elastic modulus, atomic radius<sup>78,79</sup>. MD simulation is an atomistic technique to study the physical movements of atoms and molecules. MC simulation has also been applied to build the atomic structure of HEAs composed of four to eight elements by satisfying the maximum

entropy principle. The distance of an atom to its nearest same-element atom in different HEAs was also calculated in this study. Phase field modeling is one of the principle tools to understand and simulate the microstructure evolution during phase transformation such as solidification, deformation behavior, and grain coarsening. Although till now there are no publications on using phase field modeling method to understand or predict the microstructure evolution of HEAs, it is still a good potential method to design the HEAs with desired microstructure.

Some modeling and calculation methods such as Density Function Theory (DFT), Ab Initio Molecular Dynamics (AIMD) and CALPHAD Modeling have been introduced to choose potential elements to form HEAs. For DFT calculation, there are two popular types of models to simulate the disordering solid solutions, which are special quasi-random structure (SQS) model and Kohn-Rostocker-coherent potential approximation (KKR-CPA) model<sup>80, 81</sup>. However, these two methods have only been applied to binary or ternary solid solutions. AIMD method could be used to predict the structure of solid solution. So the reasonable potential elements can be chosen from periodical table of elements to promote the formation of homogenous solid solutions by avoiding strong chemical segregation or detrimental inter-metallic and maintain comparable diffusivity among principal elements to form a homogenous microstructure during cooling. Gao MC et al.<sup>82</sup> calculated the atomic structure of Al<sub>1.3</sub>CoCrCuFeNi alloy by AIMD method and found that Cu-Cu cluster will be formed in this alloy. Zhang C et al.<sup>83</sup> calculated the isopleth of the Al<sub>x</sub>CoCrFeNi alloys and Kim KB et al.<sup>84</sup> calculated the solidification paths for Al<sub>x</sub>CoCrFeNi alloys by Schell model. Sheng Guo et al.<sup>85</sup> investigated the effect of valence electron concentration on the stability of FCC or BCC phases in HEA. It was found that FCC phase was more stable if the alloy had a valence electron concentration higher than 8 while BCC was more stable if the alloy had a valence electron concentration lower than 6.7. That provided an important guide for the design of HEA. Zhisheng Nong et al.<sup>86</sup> calculated the stability of intermetallic compounds in FeTiCoNiVCrMnCuAl HEA by first principle calculation. According to calculation results, FeTi, Fe<sub>2</sub>Ti, AlCrFe<sub>2</sub>, Co<sub>2</sub>Ti and AlMn<sub>2</sub>V intermetallic compounds had the enthalpy less than -0.35eV/atom and a cohesive energy less than -7.0eV/atom, which means these compounds will form during the fabrication process of FeTiCoNiVCrMnCuAl HEA. The formation of these types of intermetallic compounds will improve the hardness and strength of HEA. K. Jasiewicz et al.<sup>87</sup> employed the first principle calculations to estimate the electron-phonon coupling constant of Ta<sub>34</sub>Nb<sub>33</sub>Hf<sub>8</sub>Zr<sub>14</sub>Ti<sub>11</sub> HEA. Ta<sub>34</sub>Nb<sub>33</sub>Hf<sub>8</sub>Zr<sub>14</sub>Ti<sub>11</sub> was the first superconducting HEA with a T<sub>c</sub> of 7.3K. The electron-phonon coupling constant was consisted of electronic part and phonon part. Electronic part of the electron-phonon coupling constant was calculated by using the rigid muffin-tin approximation and the phonon part of the electron-phonon coupling constant was approximated by using both of average atomic mass and experimental Debye temperature. The calculated showed a constant of 1.16, which is close to the

value from specific heat measurements (0.98). It revealed a strong electron-phonon coupling in this HEA. Shiqing Wang et al.<sup>88</sup> investigated the addition of Cr into FeNiCrCuCo HEA by first-principle calculations. Both of the plane-wave pseudopotentials and alchemical pseudo-atom method were realized to model the random lattice occupation of each element in HEA. The key role of Cr in this HEA was confirmed. Addition of Cr increased the formation enthalpy and decreased the lattice constant of FeNiCrCuCo HEA.

The entropy changes before and after mixing of different elements are consisted of four terms, which are configuration entropy, electron excitation entropy, lattice phonon vibration entropy and magnetic spin fluctuation entropy. In the current design of HEA, usually only the configuration entropy is considered<sup>89</sup>.  $\Delta S = \Delta S^{conf} = -R \sum_{i=1}^N x_i \ln x_i$ . Here  $\Delta S$  is the change of mixing entropy,  $\Delta S^{conf}$  is the change of configuration entropy, N is the number of elements in the HEA system,  $x_i$  is the atomic percent of the  $i^{\text{th}}$  element. However, Ma et al.<sup>90</sup> revealed that electron excitation and magnetic spin fluctuation entropy terms were also important to determine the value of mixing entropy, which played an important role in the phase stability of HEA. According to the results from a finite-temperature ab initio method, in the CoCrFeMnNi HEA, electron excitation and magnetic spin fluctuation entropies can reach up to 50% of the configuration entropy. It means the current principle used to design HEA-only consider the contribution of configuration entropy to the mixing entropy, may fail.

Fan Zhang et al. discussed the role of entropy of mixing in determining the phase stability of HEA and the role of phase diagram calculation in design of HEA. The phase diagram calculation results from Pandat<sup>TM</sup> software showed that so-called reported single phase HEA were formed due to the fast cooling of the melt during casting. The primary solidified phase became the casting microstructure after solidification. Other phases will come out if the alloy is annealed at an elevated temperature. The calculated Co-Cr-Fe-Mn-Ni, Co-Cr-Fe-Mn-Cu and Cr-Nb-Ti-V-Zr systems using phase diagram calculation approach explained the experiments well. Michael. Gao et al.<sup>91</sup> used both of the AIMD and phase diagram calculation to search for the new single phase HEA. In the AIMD calculation, it showed that among  $\text{Al}_{1.3}\text{CoCrCuFeNi}$ ,  $\text{HfNbTaTiZr}$  and  $\text{CuNiPPdPt}$  HEAs, only  $\text{HfNbTaTiZr}$  shows no preferred short-range ordering or segregation in liquid.  $\text{HfNbTaTiZr}$  could form a single BCC solid solution while  $\text{Al}_{1.3}\text{CoCrCuFeNi}$  or  $\text{CuNiPPdPt}$  was consisted of four phases. In the phase diagram calculated from Pandat<sup>TM</sup> software, three types of single phase HEAs,  $\text{CoFeMnNi}$ ,  $\text{CuNiPdPt}$  and  $\text{CuNiPdPtRh}$  were predicted. It is also worth to note that a HCP single phase solid solution HEA with the composition of  $\text{CoOsReRu}$  was suggested the first time. Thermo-Calc software also has developed a novel database TCHEA1.0 for HEA phase diagram calculation. Although phase diagram calculation is helpful to explain or predict the phase stability of HEAs, there are also papers reporting the difference between the phase diagram calculation and the experimental results<sup>92,93</sup>. It is more difficult to do the phase diagram calculation for HEAs than traditional alloys because

traditional alloys only require a thermodynamic database for a limited composition space in the main-element corner while HEAs require a thermodynamic database for the entire composition range. Shaoqing Wang et al.<sup>94</sup> built the atomic structure models of several types of HEAs consisted of four to eight by the maximum entropy principle. A Monte Carlo method was developed in his study.

## 2.2 Properties of HEAs

The mechanical properties of the HEA at elevated temperatures have also been investigated. Kuznetsov et al.<sup>95</sup> compared the tensile behavior of AlCrCuNiFeCo HEA in different conditions, as cast and after forging conditions. The alloy was multistep forged at 950 °C so the cast coarse dendrite microstructure was transformed to fine equiaxed grains microstructure. Tensile tests at different temperatures were carried out. It was found the forged alloy showed higher strength and better ductility than as cast alloy at room temperature. Both of the two alloys demonstrated a decreased strength and an increased elongation with the increase of testing temperature. It was of worth to note that the forged alloy had a superplastic deformation behavior in the temperature range of 800-1000 °C. An elongation of 860% was achieved at 1000 °C. The HEAs including refractory elements such as Nb, W, V, Mo are also developed to replace the current superalloys because the operating temperature has already approaching the limit of current superalloys although they have high creep resistance, corrosion resistance and damage tolerance at elevated temperatures. They are named as refractory HEAs<sup>96</sup>. Senkov et al.<sup>97</sup> fabricated two types of refractory HEAs by arc melting, which were NbMoTaW and VNbMoTaW. Both of them showed a single BCC structure and stability below 1400 °C. Compressive tests were carried out in the temperature range from room temperature to 1600 °C. They showed high compressive strength (1250 MPa) and very limited ductility (fracture strain around 2%) at room temperature. The brittle to ductile transformation was observed at 600 °C, proved by a reduction of yield strength of 30%-40% while the strain increased to a level higher than 20%. However, these two alloys had already showed a higher strength than current used superalloys such as Inconel 718 and Haynes 230 at the temperature above 600 °C. The current issue is how to improve their ductility and machinability at room temperature. Senkov et al.<sup>98</sup> fabricated a Nb<sub>20</sub>Cr<sub>20</sub>Mo<sub>10</sub>Ta<sub>10</sub>Ti<sub>20</sub>Zr<sub>20</sub> HEA by arc melting and hot isostatic pressing (HIP) to close the shrink age porosity. The alloy was consisted of three different phases, two BCC phases plus one FCC phase and the volume fraction of three phases are 67% (BCC1), 16% (BCC2) and 17% (FCC). It showed a yield strength of 1595 MPa at room temperature and 983 MPa at 800 °C, which is higher than the strength of current superalloys at 800 °C. Another refractory HEA, TaNbHfZrTi was also developed by Senkov et al.<sup>99</sup>. It was produced by arc melting, HIP and homogenization at 1473 K for 24h. It showed a single BCC structure. Compressive tests were taken in a temperature range of 296-1437 K. Yield strength of the alloy at different temperatures were 929 MPa at 296 K, 790 MPa at 673 K, 675 MPa at 873 K, 535 MPa at 1073 K, 295 MPa

at 1273 K and 92 MPa at 1473 K. In the range of 296-873 K, the alloy showed a continuous strain hardening and strain higher than 50%. The dynamic recrystallization started at 1073 K and completed at 1473 K. The potential of refractory to replace current superalloys have been indicated. However, the cost of HEA is still high although it is lower than that of superalloys because some expensive elements such as Co, Nb, W are used. The micro-mechanical properties of refractory HEA based on Zr, V, Ti, Nb and Hf were predicted by Xiaoqing Li et al.<sup>100</sup> using ab initio alloy theory. Comparing ZrNbHf and ZrNbTiV, it was found the ideal tensile strength in [001] direction decreased with the addition of Ti to ZrNbHf. But the ideal tensile strength was increased by 42% while both of Ti and V were added into ZrNbHf by comparing ZrNbTiV with ZrNbHf. It is more worth to note that the ideal strength was increased by 170% if Ti and V were added to replace Hf. During the uniaxial tensile test, a brittle to ductile transition was observed after Ti and V were added into ZrNbHf by comparing ZrNbTiV with ZrNbHf. It provided a route to fabricate an ideal refractory HEA with good ductility and high ideal strength by controlling the mole ratio of IV group elements to V group elements.

Some HEAs even show the better ductility and higher strength at cryogenic temperature than room temperature. Bernd et al.<sup>101</sup> found that CrMnFeCoNi fabricated by arc melting, cold forge, cross rolling and recrystallization shows a tensile elongation of 71% and a tensile strength of 1200 MPa at 77 K while 293 K it shows a tensile elongation of 56% and a tensile strength of 780 MPa. The nano-twinning mechanism is responsible for the excellent plasticity of HEA at cryogenic temperature instead of slip of dislocations at room temperature. According to the fracture microstructure, there is less necking in the sample of 77 K, which leads to the better ductility of the sample of 77 K. Qiao et al.<sup>102</sup> found that the AlCoCrFeNi HEA shows a compressive strength of 3500 MPa, which is higher than that at room temperature (298 K). However, the compressive elongation almost kept unchanged from 298K to 77K. The high magnification SEM images for the fracture surface indicated both the samples of 298K and 77K show the ductile fracture. Lakionova et al.<sup>103</sup> studied the mechanical properties of Al<sub>0.5</sub>CoCrCuFeNi HEA with a single FCC structure in range of 4.2-300 K. It was found that the yield strength of the HEA increased to 750 MPa from 450 MPa while the elongation stayed around 30%. The activation volume for dislocation moving was measured with strain  $\epsilon$  fixed at 2%. It decreased from  $122b^3$  to  $35b^3$  when the temperature decreased from 300 to 30 K. Here  $b$  means the Burgers vector of the dislocation. The FCC HEA didn't exhibit the ductile to brittle transformation temperature, the same with FCC traditional metals or alloys.

The fatigue behavior of HEAs also needs to be discussed. However, till now the literature reported is very limited. Hemphill et al.<sup>104</sup> investigated the fatigue behavior of Al<sub>0.5</sub>CoCrFeNi HEA. Results showed that HEA's fatigue behavior is more favorably than the traditional alloys for example, stainless steel, Ti alloys and bulk metallic glasses which have a fatigue endurance between 540 and 945 MPa, a ratio of

fatigue endurance to tensile strength between 0.402 and 0.703. Besides, the data showed a big variation during the tests. The data were separated into two groups, weak group and strong group with a Weibull mixture model. Inclusions like alumina and microcracks were observed in the weak group samples, which means the microdefects have significant effects on the fatigue behavior of HEAs.

The wear behavior of HEA is also needed to be studied. Some wear behavior under both of abrasive conditions and adhesive conditions have been carried out in order to evaluate its competitive and potential for using as tools, molds components material. Chuang et al.<sup>105</sup> fabricated a series of  $\text{Al}_x\text{Co}_{1.5}\text{CrFeNi}_{1.5}\text{Ti}_y$  HEAs and investigated the phase structure, microstructure and the wear behaviors. It was found the amount of Al significantly affect the wear behavior of the alloy, with the increase of the Al content, the volume fraction of  $\eta$  precipitation phase increased, thus increasing the hardness and wear resistance of the alloy. The HEA also showed excellent oxidation and softening resistance owing to the existence of the  $\eta$  precipitation phase. Comparing with the common wear resistance steel SUJ2 and SKH51, with similar hardness, the HEA was more than two times better. Wu et al.<sup>106</sup> found that the wear resistance of  $\text{Al}_x\text{CoCrCuFeNi}$  HEA increased with the increase of Al content. It was attributed the increase of hardness with the increase of Al content and a transition from FCC to BCC happened during the increase of Al content. It can be concluded that HEA has a larger range of hardness, from 300 MPa to about 3000 MPa. And the phases, microstructure is also affected by cooling during solidification.

The deformation mechanism of HEAs also needs to be studied. The plastic deformation mechanism of traditional alloys and quasi-crystals<sup>107</sup> is dislocation slipping while deformation mechanism of metallic glass is shear-transition-zone model<sup>108</sup> because dislocation or twinning is difficult to define in metallic glass.

Ma et al.<sup>109</sup> fabricated a HEA  $\text{AlCoCrFeNb}_x\text{Ni}$  ( $x=0-0.75$ ) which shows ferromagnetic properties and permeability varying within the range of  $2 \times 10^{-2}$ - $3 \times 10^{-3}$ . HEAs ( $\text{Ti}_{0.8}\text{CoCrCuFeNi}$  and  $\text{TiCoCrCuFeNi}$ ) with supermagnetic properties because of the formation of nanoparticles are also reported<sup>110</sup>. Chou et al.<sup>111</sup> fabricated a  $\text{CoCrFeNiCuAl}$  HEA and measured the magnetic hysteresis loops of the as-cast and as-annealed HEA at room temperature. The saturated magnetizations, remanence ratio and coercivity are 38.18 emu/g, 5.98%, 45 Oe, 16.08 emu/g, 3.01%, 15 Oe, showing excellent soft magnetic properties. Chen et al.<sup>112</sup> measured the electrical resistivity within the temperature range of 4.2-360 K. It was found that the resistivity showed a constant of 72 ppm/K with the increase of temperature, similar to the Manganin (an alloy of  $\text{Cu}_{86}\text{Mn}_{12}\text{Ni}_2$ ) developed by Weston in 1982. Kao et al.<sup>113</sup> studied the absorption and desorption hydrogen behavior of  $\text{CoFeMnTiVZr}$  HEA. The pressure-composition-isotherms showed  $0.5 < x < 2.5$ ,  $0.4 < y < 3.0$  and  $0.4 < z < 3.0$  respectively for  $\text{CoFeMnTi}_x\text{VZr}$ ,  $\text{CoFeMnTi}_y\text{V}_z\text{Zr}$  and  $\text{CoFeMnTiVZr}_z$ .

### 2.3 Fabrication, preparation and applications of HEAs

There are two typical methods to fabricate HEAs bulk materials, which are arc melting and powder metallurgy.<sup>114</sup> Arc melting is a method which first melts the pure elements consisting of HEA by arc at a vacuum or Ar atmosphere then the sample is cooled by the water under the supporting plate to hold the copper crucible after the arc is removed. Although some entropy alloys containing the element which is easy to vaporize can't be fabricated by arc melting method, it is the most common method used to fabricate HEAs. The schematic diagram of arc melting is shown in Figure 2.1. According to the literature<sup>115</sup>, more than 150 types of HEAs have been fabricated by arc melting. Singh et al.<sup>116</sup> carefully investigated the effect of cooling rate on the microstructure of the AlCoCrCuFeNi HEA. The melt had a tendency to form a single phase polycrystalline alloy at a level of  $10^6$ - $10^7$  K/s. However, it tended to form a dendrite plus interdendrite microstructure with different compositions at a level of 10-20 K/s.

Bridgman solidification, whose schematic diagram is shown in Figure 2.2, is a useful method to grow single crystal HEA from liquid state. The polycrystalline HEA is melted first and slowly cooled by a liquid metal (usually a eutectic Ga-In alloy, stays in liquid state at room temperature) from the end of the container with a seed located there. The single crystal having the same orientation with the seed forms and grows along the length of the container. It has been reported that Zhang et al.<sup>117</sup> successfully fabricated a CoCrFeNiAl<sub>0.3</sub> single crystal by Bridgman solidification method. In his study, along the growth direction from the end to the top of the container, the solidified alloy is composed of four different microstructures which are as-cast dendrite, equiaxed grains, columnar crystals and single crystal. The solidification was carried out with a pulling rate of 5 $\mu$ m/s and a temperature gradient of 45K/mm. It is interesting to note that the single crystal could not form if the composition of the HEA was changed to CoCrFeNiAl probably owing to the higher stacking fault energy caused by the high atomic percent of aluminum. Feuerbracher et al.<sup>118</sup> successfully fabricated a single crystal FeCoCrMnAl HEA cylinder by Bridgman method. It had a diameter of 1cm and a length of 6.6 cm. The X-ray Laue images were taken at different positions to confirm the single crystal nature. It is the first report of growth of HEA having a volume of the order of cubic centimeters.

Mechanical mixing is also a useful technique for preparing HEAs, especially if the alloys contain elements that easily vaporize. A solid-state preparation technique such as ball milling can be used to mix the pure metals uniformly by pressing, sintering and final heat-treatment. Pressing and sintering could be finished at the same time if hot isostatic pressing (HIP) is applied. The purpose of final heat treatment is to remove the internal stresses produced during pressing. Two equi-molar alloys entirely composed of HCP elements, BeCoMgTi and BeCoMgTiZn were fabricated by Chen et al.<sup>119</sup> The fabricated alloy showed an

entirely amorphous structure with no crystalline solid solution or compounds. Varalakhmi et al.<sup>120</sup> fabricated a nanocrystalline HEA, CuNiCoZnAlTi with a BCC structure by ball milling Cu-Ni alloy, Co, Zn, Al, Ti powders and HIP. It showed a Vickers hardness of 8.79 GPa and a compressive strength of 2.76 GPa, higher than those of current hard-facing alloys.

Sputtering technique is a method to fabricate HEA or HEA nitride coating layer. (AlCrTaTiZr) $N_x$  coatings were prepared by Chang et al.<sup>121</sup> using sputtering technique. The content of nitride was controlled by changing the  $N_2:(N_2+Ar)$  flow ratio during the deposition process. With the increase of the N content (flow ratio from 0% to 10%, finally 30%), (AlCrTaTiZr) $N_x$  first changed to a nano-composite from a noncrystalline structure and finally changed to a crystalline nitride structure. The hardness also increased to 30 GPa from 13 GPa while creep strain rate increased to  $7.3 \times 10^{-4}$  from  $1.3 \times 10^{-4}$ . (AlCrTaTiZr) $O_x$  amorphous HEA oxide was fabricated by Lin et al.<sup>122</sup> with magnetron sputtering. The oxygen content was controlled by changing the  $O_2:(O_2+Ar)$  flow ratio. The hardness of the film varied within the range of 8-13 GPa. The resistivity of film increased from  $10^2$  to  $10^{12}$   $\mu\Omega$  with the increase of the oxygen content. The film could maintain its amorphous structure below 900 °C. Crystal phases appeared after the film was annealed at 900 °C for 5 hours. A hardness of 20 GPa was achieved after annealing.

Laser cladding is also a method to deposit a HEA coating on the surface of a component to optimize the properties of component. 6FeNiCoSiCrAlTi, a BCC HEA coating with a thickness of 1.7-2.0 mm was deposited on the surface of a Q235 steel tube by laser cladding method using a laser-induction hybrid cladding head<sup>123</sup>. The surface microstructure hardness of Q235 steel tube increases from 250 HV to 800 HV. The surface hardness, surface strength, resistance to wear and corrosion were obviously improved.

HEA can also be prepared by electrochemical method. It is reported that Yao et al.<sup>124</sup> fabricated a BiFeCoNiMn HEA film using electrochemical method. However, till now, the electrochemical preparation of HEA is very limited.

Several potential applications of HEA have been proposed:<sup>125,126,127,128</sup>

1. There have already been some patents using HEA as solder or brazing filler metal. For example, HEA can be used as solder for welding pure Ti to Cr-Ni-Ti stainless steels; Filler metal for brazing cemented carbide to steel.
2. HEA has excellent ferromagnetic properties and soft magnetic properties. It shows the potential of magnetic materials.

3. As is mentioned above, HEA has high resistance to corrosion and radiation, which shows the potential to be the candidate as high pressure vessel materials or cladding materials of the nuclear fuels.
4. Low density HEAs can be used as hard surface materials in the transportation industry such as battery materials.
5. Some special HEA systems, such as Al<sub>2</sub>.08CoCrFeNi, have near constant resistivity within the temperature range of 4.2K-36K, showing the potential to be used in electronic applications.
6. Refractory HEAs can be used as superalloys or thermal barrier coatings in the future, such as tool materials for friction stir welding materials. The tool material for friction stir welding needs to satisfy following requirements:
  - a. High strength, fracture toughness, dimension stability, creep resistance, thermal fatigue strength, good resistance to wear
  - b. Higher compressive yielding strength at high temperature than expected forging force on the tool during processing
  - c. No harmful reactions between the tool material and the work pieces
  - d. Low coefficient difference between the shoulder material and the probe material to reduce the thermal stress
  - e. Good machinability to manufacture the shoulder or probe with complex features
  - f. Low production cost
  - g. Some types of tool materials being used now are tool steels, Ni or Co based superalloys, refractory metals, carbides, ceramic reinforced composite materials, polycrystalline boron nitride, which will be discussed below.

Tool steels such as AISI H13, AISI 4340 are the most common used tool materials for friction stir welding of Al, Mg, Cu alloys, Al or Mg based metal composite materials. However, the relatively low strength at high temperature limits its application. Ni or Co based superalloys, with high strength, good ductility, good creep, wear and corrosion resistance at high temperature, are also used as tool materials. However, Ni or Co based superalloys are usually difficult to machine. Refractory metals such as PM3030, Nimonic 90, Nimonic 105 with high temperature strength, could be used as tool materials during welding of high melting temperature metals such as Cu, Ti alloys and stainless steels. Most of them are single phase so that the mechanical properties could maintained at higher temperature than above tool materials. But the production cost of refractory metals is somewhat high because they are usually produced by powder metallurgy method. Also Ta and Nb have high oxygen solubility at high temperature so that the ductility will be degraded. Carbides with reasonable toughness at ambient temperature and superior resistance to

wear is also a common used tool material for friction stir welding. But it is not good for Cu alloys. Ceramic reinforced composite materials are also used as tool materials but because of its brittle nature, fracture always happens during tool plunging phase. Poly-crystalline boron nitride, with high strength at high temperature, good chemical stability, and excellent wear resistance is a novel type tool material for friction stir welding. However, the high production cost (a combination of high temperature and high pressure is required during sintering of boron nitride), size limitation, difficult to machine, low fracture toughness limit its wide applications.

Advantages of refractory HEAs are high strength at ambient temperature, dimension stability, good resistance to wear, usually showing a BCC single phase, high melting point, good creep resistance, high thermal strength. Disadvantages of refractory HEAs are relatively ductility than Ni or Co based superalloys at high temperature, low fracture toughness, difficult to machine because of the high hardness, high strength, and low ductility, high production cost (Powder metallurgy is often used to produce tools with the desired shape due to the poor machinability of cast refractory HEA). Table 2.1 shows the mechanical properties including strength, elongation, hardness and phase structure of the common refractory HEAs.

Continuing with the list of proposed applications of HEAs:<sup>129,130,131,132</sup>

7. As is mentioned above, some HEAs have high heat resistance and wear resistance. It shows the potential of surface coating materials for tubes or pipes.
8. The nuclear fission process is also an entropy increasing process because more elements are created during the nuclear fission process. Some models for simulation and calculation of HEA can be used for modeling the fission process.
9. HEA carbide, nitride and oxides is also an interesting topic because of their amorphous structure and high hardness, strength, modulus. They can be used as high speed steel coatings, tool steel coatings and thermal barrier coatings.

There are several types of mold materials for aluminum or aluminum alloy casting, which are ferrous alloys, Ni-base alloys, Titanium-base alloys, ceramics and graphite. Ferrous alloys are the most common aluminum casting mold materials. It has been reported that an intermediate zone, usually consisted of two layers,  $\theta$ -FeAl<sub>3</sub> phase adjacent aluminum melt and  $\eta$ -Fe<sub>2</sub>Al<sub>5</sub> adjacent ferrous alloy, has been observed between ferrous alloys and aluminum melt. For H13 and H12 tool steels,  $\zeta$ -FeAl<sub>2</sub> is also observed between ferrous alloy and  $\eta$ -Fe<sub>2</sub>Al<sub>5</sub>. Except these three phases, any other phase in the Al-Fe phase diagram has never been found. The thickness of the intermediate zone is up to hundreds of microns. Ni-base alloy is not an ideal candidate as aluminum alloy casting mold materials because Ni is active with both of molten aluminum and solid aluminum. Ni-base alloy is used in the production of aluminum reinforced composite

materials to solve the non-wetting problem between aluminum melt and reinforcements. Compared with ferrous alloys and Ni-base alloys, Titanium has better corrosion resistance. Mihelich et al. investigated the corrosion rate of Stellite 6B, Stellite 12, Alloy 718, Alloy 909, Tool steels, Ti-6Al-4V, Ti-6Al-2Sn-4Zr-2Mo, Ti-0.2Pd and Nb-30Ti-20W in A356/601 slurry at 600 and 625 °C. It was found that except Ni-30Ti-20W with a corrosion rate of 6µm/h, titanium alloys have the lowest corrosion rate in the range of 12-45 µm/h. The corrosion rate of Ni-base alloys and ferrous alloys are higher than 150 µm/h. Till now, several ceramics such as aluminum nitride, silicon nitride, alumina and sialons have been used as mold materials. Al<sub>4</sub>C<sub>3</sub> is the only intermediate compound found between graphite and aluminum melt. Simenmen et al. investigated the concentration of Al<sub>4</sub>C<sub>3</sub> formed between graphite and aluminum melt at different temperatures within the range of 950-1000 °C. Graphite is a well-known mold material because it's large thermal expansion coefficient and ease of fabrication. However, it is difficult to use graphite for mold materials due to its brittleness.

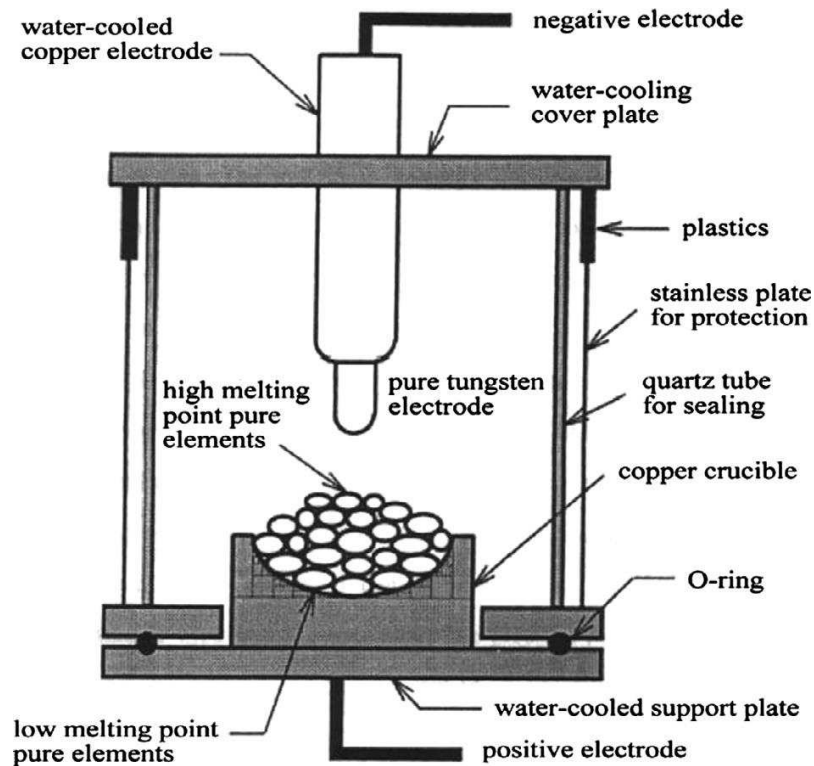


Figure 2.1 Schematic diagram of the arc melting set-up

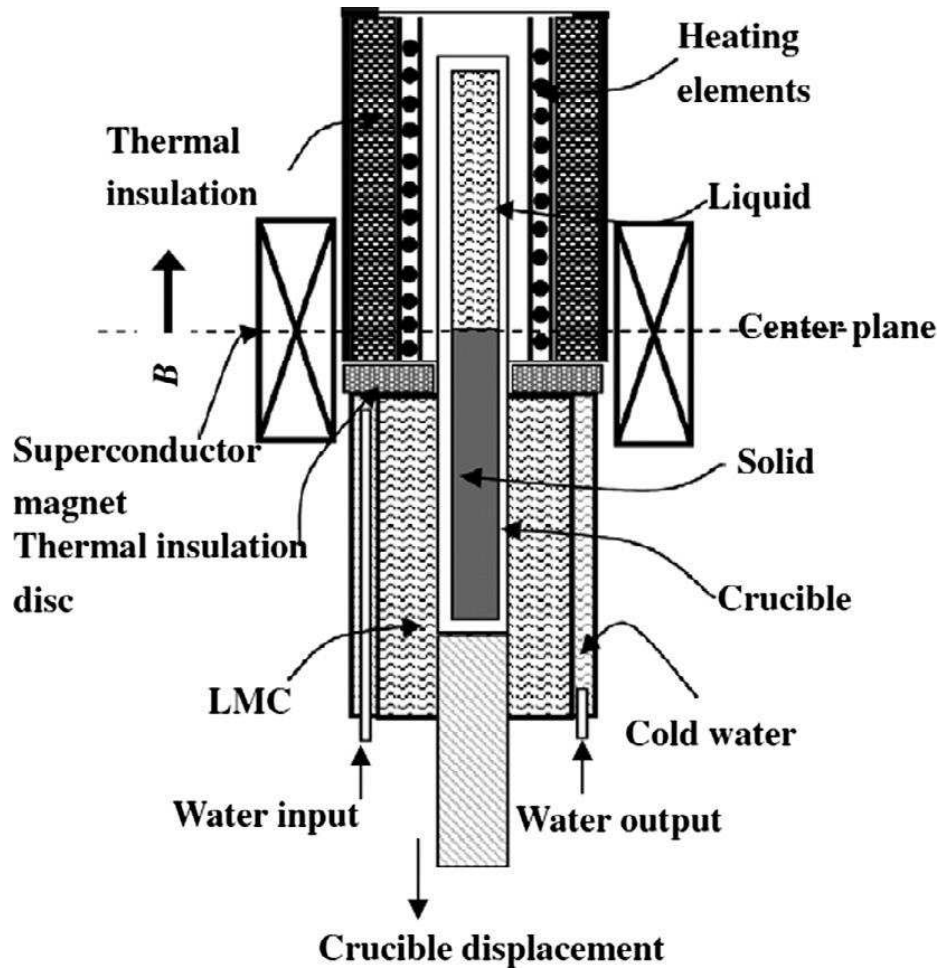


Figure 2.2 Schematic diagram of the Bridgman solidification set-up

Table 2.1 Mechanical properties and phases of refractory HEAs .YS means yield strength and PS means peak strength.

Composition	Strength	Fracture strain	Phase structure	Test method
HfNbTiZr	969 MPa(RT,UTS)	14.90%	Single BCC	tensile
HfNbTiVSi0.5	1400 MPa (RT, PS)	10.90%	BCC+(Hf,Nb,Ti) silicide	compression
	875 MPa (1073K,peak strain)	50%	BCC+(Hf,Nb,Ti) silicide	compression
	240 MPa (1273K, peak strain)	50%	BCC+(Hf,Nb,Ti) silicide	compression
NbMoTaW	1058 MPa (RT,YS),1211 MPa (PS)	1.50%	Single BCC	compression
	548 MPa (1273K,YS),1008 MPa (PS)	16%	Single BCC	compression
	506 MPa (1473K,YS),803 MPa (PS)	12%	Single BCC	compression
	421 MPa (1673K,YS),467 MPa (PS)	9%	Single BCC	compression
	405 MPa (1873K,YS),600 MPa (PS)	27%	Single BCC	compression
VNbMoTaW	1246MPa (RT,YS),1270 MPa (PS)	2%	Single BCC	compression
	862MPa (873K,YS),1597 MPa (PS)	13%	Single BCC	compression
	846 MPa (1073K,YS),1536 MPa (PS)	17%	Single BCC	compression
	842 MPa (1273K,YS),1454 MPa (PS)	19%	Single BCC	compression
	735MPa (1473K,YS),943 MPa (PS)	8%	Single BCC	compression
AlNbTiV	1000MPa (RT,YS),1280 MPa (PS)	5%	Single BCC	compression
	780MPa (873K,YS),1050 MPa (PS)	13%	Single BCC	compression
	560MPa (1073K,YS),700 MPa (PS)	>50%	Single BCC	compression
	110MPa (1273K,YS)	>50%	Single BCC	compression
AlCr0.5NbTiV	1300MPa (RT,YS),1430 MPa (PS)	1%	Single BCC	compression
	1005MPa (873K,YS),1045 MPa (PS)	3%	Single BCC	compression
	640MPa (1073K,YS),685 MPa (PS)	>50%	Single BCC	compression
	40MPa (1273K,YS),80 MPa (PS)	>50%	Single BCC	compression
AlCrNbTiV	1550MPa (RT,YS),1570 MPa (PS)	0%	BCC+Laves phase	compression
	1015MPa (873K,YS),1060 MPa (PS)	2%	BCC+Laves phase	compression
	860MPa (1073K,YS),895 MPa (PS)	>50%	BCC+Laves phase	compression
	65 MPa (1273K,YS),95 MPa (PS)	>50%	BCC+Laves phase	compression
AlCr1.5NbTiV	1700MPa (RT,YS),1700 MPa (PS)	0%	BCC+Laves phase	compression
	1370MPa (873K,YS),1480 MPa (PS)	1%	BCC+Laves phase	compression
	970MPa (1073K,YS),1045 MPa (PS)	>50%	BCC+Laves phase	compression
	75 MPa (1273K,YS),105 MPa (PS)	>50%	BCC+Laves phase	compression
NbNiTiCoZr	2331MPa (RT,YS),2500 MPa (PS)	0%	BCC1+BCC2	compression
	1385MPa (873K,YS),1566 MPa (PS)	7%	BCC1+BCC2	compression
	668MPa (973K,YS),1021 MPa (PS)	>50%	BCC1+BCC2	compression
	427 MPa (1073K,YS),567 MPa (PS)	>50%	BCC1+BCC2	compression
	213MPa (1173K,YS),324 MPa (PS)	>50%	BCC1+BCC2	compression
	60 MPa (1273K,YS),91 MPa (PS)	>50%	BCC1+BCC2	compression
NbNiTiCoZrHf	1469MPa (RT,YS),1800 MPa (PS)	1%	BCC+FCC+NbNi	compression
NbTaTiV	965MPa (RT,YS),1275 MPa (PS)	12%	Single BCC	compression
NbTaVW	1530MPa (RT,YS),1700 MPa (PS)	20%	Single BCC	compression

Table 2.1 Continued

NbTaTiVW	1420MPa (RT,YS),1800 MPa (PS)	48%	Single BCC	compression
NbTiVTa	1090MPa (RT,YS),3500 MPa (PS)	50%	Single BCC	compression
NbTiVTaAl0.25	1340MPa (RT,YS),3750 MPa (PS)	55%	Single BCC	compression
NbTiVTaAl0.5	1015MPa (RT,YS),3250 MPa (PS)	57%	Single BCC	compression
NbTiVTaAl	990MPa (RT,YS),3300 MPa (PS)	65%	Single BCC	compression
AlNbTiVZr0.5	1430MPa (RT,YS),2150 MPa (PS)	>50%	BCC+Laves phase+Zr2Al	compression
	1160MPa (873K,YS),1800 MPa (PS)	>50%	BCC+Laves phase+Zr2Al	compression
	680MPa (1073K,YS),800 MPa (PS)	>50%	BCC+Laves phase+Zr2Al	compression
	75MPa (1273K,YS),80 MPa (PS)	>50%	BCC+Laves phase+Zr2Al	compression
TaNbHfZrTi	929MPa (RT,YS),2300 MPa (PS)	>38%	Single BCC	compression
AlMo0.5NbTa0.5TiZr	2000MPa (RT,YS),2368 MPa (PS)	10%	BCC1+BCC2	compression
	1870MPa (873K,yield strength),2210 MPa (PS)	10%	BCC1+BCC2	compression
	1597 MPa (1073K,YS),1810 MPa (PS)	11%	BCC1+BCC2	compression
	745 MPa (1273K,YS),772 MPa (PS)	>50%	BCC1+BCC2	compression
	250 MPa (1473K,YS),275 MPa (PS)	>50%	BCC1+BCC2	tensile
TaNbHfZrTi	1155 MPa (RT,YS,tensile),1212 MPa (UTS)	12%	single BCC	compression
HfNbTaTiZr	1015MPa (RT,YS),1600MPa (PS)	>50%	Single BCC	compression
HfMo0.25NbTaTiZr	1112MPa (RT,YS),1750 MPa (PS)	>50%	Single BCC	compression
HfMo0.5NbTaTiZr	1317MPa (RT,YS),2250 MPa (PS)	>50%	Single BCC	compression
HfMo0.75NbTaTiZr	1373MPa (RT,YS),2500 MPa (PS)	>50%	Single BCC	compression
HfMoNbTaTiZr	1512MPa (RT,YS),1800 MPa (PS)	12%	Single BCC	compression
HfNbTaTiZr	1073±6MPa (RT,YS),1650 MPa (PS)	>50%	Single BCC	compression
Al0.3HfNbTaTiZr	1188±7MPa (RT,YS), 1850 MPa (PS)	>50%	Single BCC	compression
Al0.5HfNbTaTiZr	1302±6MPa (RT,YS), 2300 MPa (PS)	46%	Single BCC	compression
Al0.75HfNbTaTiZr	1415±4MPa (RT,YS),2100 MPa (PS)	30%	Single BCC	compression
AlHfNbTaTiZr	1489±7MPa (RT,YS),1900 MPa (PS)	21%	Single BCC	compression
AlMo0.5NbTa0.5TiZr	2000 MPa (RT,YS),2368 MPa (PS)	10%	BCC1+BCC2	compression
	1597 MPa (873K,YS),1810 MPa (PS)	11%	BCC1+BCC2	compression
	745 MPa (1073K,YS),772 MPa (PS)	>50%	BCC1+BCC2	compression
	250 MPa (1273K,YS),275 MPa (PS)	>50%	BCC1+BCC2	compression
Al0.4Hf0.6NbTaTiZr	1841 MPa (RT,YS),2269 MPa (PS)	10%	Single BCC	compression
	796 MPa (873K,YS),834 MPa (PS)	>50%	Single BCC	compression
	298 MPa (1073K,YS),455 MPa (PS)	>50%	Single BCC	compression
	89 MPa (1273K,YS),135 MPa (PS)	>50%	Single BCC	compression
TiZrHfNbV	1170 MPa (RT,YS),1463 MPa (PS)	30%	BCC+ compound	compression
TiZrHfNbCr	1375 MPa (RT,YS),2130 MPa (PS)	40%	BCC+Laves 1+Laves 2	compression
NbCrMo0.5Ta0.5TiZr	1595 MPa (RT,YS),2046 MPa (PS)	5%	BCC1+FCC(Laves)+BCC2	compression
	983 MPa (1073K,YS),1100 MPa (PS)	6%	BCC1+FCC(Laves)+BCC2	compression
	546 MPa (1273K,YS),630 MPa (PS)	No fracture	BCC1+FCC(Laves)+BCC2	compression
	170 MPa (1473K,YS),190 MPa (PS)	No fracture	BCC1+FCC(Laves)+BCC2	compression

Table 2.1 Continued

NbTiVZr	1105 MPa (RT, YS), 1732MPa(20%)	>50%	Single BCC	compression
	834MPa (873K, YS), 767MPa (20%)	>50%	Single BCC	compression
	187 MPa (1073K, YS), 174MPa(20%)	>50%	Single BCC	compression
	58 MPa (1273K, YS), 77 MPa(20%)	>50%	Single BCC	compression
NbTiV2Zr	918 MPa (RT, YS), 1635MPa(20%)	>50%	BCC1+BCC2+BCC3	compression
	571MPa (873K, YS), 716MPa (20%)	>50%	BCC1+BCC2+BCC3	compression
	240 MPa (1073K, YS), 185MPa(20%)	>50%	BCC1+BCC2+BCC3	compression
	72MPa (1273K, YS), 53MPa (20%)	>50%	BCC1+BCC2+BCC3	compression
CrNbTiZr	1260 MPa (RT, YS)	6%	BCC+Laves Phase	compression
	1035MPa (873K, YS), 1030MPa (20%)	>50%	BCC+Laves Phase	compression
	300 MPa (1073K, YS), 435MPa(20%)	>50%	BCC+Laves Phase	compression
	115 MPa (1273K, YS), 136MPa (20%)	>50%	BCC+Laves Phase	compression
CrNbTiVZr	1298 MPa (RT, YS)	3%	BCC+Laves Phase	compression
	1230MPa (873K, YS), 1360 MPa (10%)	>10%	BCC+Laves Phase	compression
	615 MPa (1073K, YS), 512MPa(20%)	>50%	BCC+Laves Phase	compression
	259 MPa (1273K, YS), 183MPa (20%)	>50%	BCC+Laves Phase	compression

## 2.4 Properties and welding of Ni-base superalloys

Ni-based super-alloys are complex materials with the ability to maintain their physical and mechanical properties at elevated temperatures.<sup>133</sup> The most common Ni-based super-alloys are mainly consisted of the matrix phase gamma ( $\gamma$ ), the  $Ni_3(Al, Ti)$  intermetallic precipitate gamma prime ( $\gamma'$ )  $Ni_3Nb$ , and MC or  $M_{23}C_6$  type intermetallic phases where M represents the alloying elements such as Co, Fe, Cr, Ti, Al, Nb, Mo, W and Ta.<sup>134</sup> There are also some minor phases such as sigma ( $\sigma$ ), mu ( $\mu$ ) and Laves phase in Ni-based super-alloys. Ni-based super-alloys have been widely used in many different fields such as aerospace, marine propulsion, submarines and nuclear reactors and powder generation industries, especially in the component of gas turbine engine which requires good ductility, high strength, high fatigue strength, high resistance to oxidation and corrosion at high temperature<sup>135</sup>. Among all the characteristics, high temperature creep resistance, high temperature corrosion and oxidation resistances are the most important ones. The precipitation phases enhanced the strength at high temperature and the resistance to oxidation and corrosion are improved by the formation of protective  $Cr_2O_3$  and  $Al_2O_3$  oxide films on the surface.<sup>136</sup> The average tolerance temperature of new generations of super alloys is 1050 °C and the highest tolerance temperature can be as high as 1200 °C, nearly 90% of the melting point of the nickel based super-alloys.<sup>137</sup> Typical nickel based super-alloys include CMSX2, CMSX4, CMSX6, CMSX10, Hastelloy X, Hastelloy S, Inconel 600, Inconel 718, Rene 108, Rene 41, Waspaloy, and many others. The Ni-based super-alloys are usually imposed at high temperature for prolonged periods, making them damaged by different types of

mechanisms such as hot gas erosion. Some types of methods to repair the parts or components made of Ni-based super-alloys have been proposed.

Welding is the most common repair method. However, the fusion welding of nickel based super-alloys has some issues, such as strain cracking, solidification cracking and liquation cracking. Especially the liquation cracking, which occurs in heat affected zone, can be a serious issue for the Ni-based super-alloy with Al+Ti>7% wt. Chen et al.<sup>138</sup> found that in the fusion zone of electron beam welded GH4169 alloy, the low melting point strengthening phase particles such as Ni<sub>3</sub>Nb distributed along the grain boundaries, which results in the liquid crack. The liquid crack can be reduced by introducing Mn into welding. Mn<sub>2</sub>Nb which has a higher melting point than f Ni<sub>3</sub>Nb formed so that the liquid crack was reduced and the overall properties were also optimized. Kim et al.<sup>139</sup> found that the cracking rate of the GTAW weldment of IN738 alloy decreases with the decrease of heat input. The morphology of the weldment changes from fine columnar to coarse cellular and the dendrite arm spacing decreases with the decrease of heat input. The cracking susceptibility is reduced because fine dendrite microstructure has less effective stress acting along the dendrite boundaries than coarse dendrite. The similar phenomenon is also found in the weldment of IN738 alloy welded by Laser Beam Welding. Ma et al.<sup>140</sup> analyzed the microstructure and mechanical properties of Hastelloy C-276 weld joint made by Laser Beam welding. The fusion zone is divided into three parts according to the grain structure, which are Center Fusion Zone (CFZ) mainly with fine sub-grain, Transition Fusion Zone (TFZ) with mixture of sub-grains and columnar dendrite, Edge Fusion Zone with the narrow area of Planar and Cellular. No obvious heat affected zone is observed. The trend to form brittle phases is weakened. The joint maintains a FCC phase structure, a yielding strength the same as base metal and tensile strength 90% of based metal. Montazeri et al.<sup>141</sup> investigated the liquation cracking of welded IN738LC in conduction and keyhole modes. Heat affected zone liquation cracking is observed associated with the constitutional liquation of  $\gamma$ - $\gamma'$  eutectic and carbides. It was found that the susceptibility to liquation cracking is decreased by increasing the heat input and peak power. While having the same heat input, conduction mode has more susceptibility to liquation cracking than keyhole modes. Suharno et al.<sup>142</sup> used a Super-alloy Welding at Elevated Temperature by pre-heating the Inconel 792 alloy at a temperature above the aging temperature prior to Gas Tungsten Arc Welding. It was found both the hot cracking and liquation cracking were reduced. It is difficult to weld Inconel 792 because the thermal gradient caused by welding will induce the formation of precipitation hardening and hardening will trap excess stress leading cracking. The thermal gradient is reduced by SWET technology so that the cracking was reduced. The weldability of Inconel 792 alloy is improved and the cost is also reduced by introducing the SWET technology. Wang et al.<sup>143</sup> selected Electron Beam Welding method to test the weldability of the second generation PWA1480 Ni-Based Super-alloy. It was found that the second generation PWA1480

alloy still has a poor weldability. Both the extensive cracking and liquation cracking were found in fusion zone and heat affected zone. It has a large solidification temperature range (1340 °C~1404°C), which places it in the “hard to weld alloy” category.

## **2.5 Brazing of Ni-base superalloy**

Brazing has been a versatile method to join two pieces of metal using a third, molten filler metal due to its advantages of high efficiency, low temperature compared with arc melting and low cost. The molten filler metal flows into the gap between two pieces to form a strong joint during the solidification. Because the base metals are usually not melted, they can maintain their original properties easily without being warped or distorted.<sup>144</sup> Due to the advantages mentioned above, especially the ability to avoid solidification cracking and liquation cracking, brazing has been used to join Ni-Based super-alloys.

### **2.5.1 Ag, Au-based filler metals for brazing of Ni-base superalloys**

Zaharinie et al.<sup>145</sup> successfully brazed two Inconel 600 alloy pieces using Cusil ABA filler metal and the effect of the brazing temperature on the shearing strength of the braze was investigated. Inconel 600 alloy was brazed at 830, 865, 930 °C separately and braze of 865 °C has a higher shearing strength than the braze of 830 °C or 930 °C. Diffusion is insufficient at 830 °C because 830 °C is only 15 °C above the melting point of Cusil ABA filler metal while 930 °C is too high, which will result in the formation of some detrimental phases due to the inter-diffusion of the elements in filler metal and base metal (Inconel 600). Zaharinie et al.<sup>146</sup> brazed Inconel 600 alloy to sapphire using Cusil ABA commercial filler metal in a high vacuum furnace. The experiments were carried out in the range of 830-900 °C and 15-30 min respectively. The maximum shearing strength of 58.5 MPa was reached at 900 °C for 30 min. Chen et al.<sup>147</sup> brazed Inconel 600 alloy to silicon nitride by using Cusil filler metal. The mechanism of bonding and the roles of different elements were investigated according to the SEM and EDS results. The bonding between Inconel 600 to filler metal was owned to the diffusion of silver and copper along the grain boundaries of Inconel 600. Ni promoted Ag or Cu rich phases to separate from the molten filler metal and decreased titanium's activity during reaction with silicon nitride ceramic.

### **2.5.2 Ni-based filler metals for brazing of Ni-base superalloys**

Miyazawa et al.<sup>148</sup> brazed 304 Stainless Steel to Inconel 600 alloy in an electrical resistant furnace in an argon gas atmosphere using three different types of filler metals, which are 4.5Si-7.0Cr-3.0B-3.0Fe-Nibal., 4.5Si-5.0Cr-3.0B-3.0Fe-Nibal and 4.5Si-10.0Cr-3.0B-3.0Fe-Ni bal. It was found except at 1050 °C, the shearing strength increases with the increase of the brazing time (10, 30, 60, and 120 min) at all the

other temperatures (1100, 1150, 1200, and 1250 °C). At 1050 °C, the shearing strength is not affected by brazing time. The maximum shearing strength of 450 MPa was achieved at 1250 °C. All the specimens showed a shearing strength increasing with the increase of the brazing temperature. Also the joint brazed using 4.5Si-7.0Cr-3.0B-3.0Fe-NiBal shows a higher shearing strength than the joints brazed by 4.5Si-5.0Cr-3.0B-3.0Fe-NiBal or 4.5Si-10.0Cr-3.0B-3.0Fe-NiBal. The brazing process using the filler metal foil could have a larger joining area than the brazing process using powder form filler metal. The brazing process using foils as filler metal is an effective method to prepare clad materials. Moore et al.<sup>149</sup> diffusion welded MA 6000 steel to Udimet 700 Ni-based Super-alloy at 1033K. It was found that the joint is relatively weak with a shearing strength lower than 100 MPa. Chaturvedi et al.<sup>150</sup> diffusion brazed the cast Inconel 738 super-alloy in the vacuum using Amdry DF3 (DF3) and Nicrobraz 150(NB150) as the filler metal. It was found that there were centerline eutectic constituents continuously distributed in the brazement, playing the role as a path for crack propagation with low resistance. Wu et al.<sup>151</sup> used Ni-7Cr-3Fe-3.2B-4.5Si (wt. pct.) filler metal to induction brazed Inconel 718 alloy to Inconel X-750 alloy. The brazing time was significantly reduced to 300 s when the brazing temperature was fixed at 1423K. The maximum shearing strength of the brazed joint (503 MPa) was achieved at only 240 s. It was found that the diffusion of silicon and boron from filler metal into base metal is the controlling factor during brazing. Silicon and chromium stayed in the center of the brazed region while boron showed a uniform distribution across the joint and diffused from filler metal into base metal. A superplastic Inconel 718 was brazed with Ni-P and Ni-Cr-P amorphous filler metal by Yeh et al.<sup>152</sup>. The effect of the applied pressure on the shearing strength and corrosion resistance of the brazed joint was investigated. It was found that Ni-Cr-P filler metal leads a better bonding than conventional Ni-P filler metal. And the shearing strength of the brazed joint increased after the pressure was applied because the fraction of the intermetallic phase decreased in the filler metal area. With two Ni or Fe based amorphous filler metal foils, MBF-51(73.6Ni-15Cr-7.3Si-1.4B in wt pct), VZ-2106(44Ni-35Fe-11Cr-1.5Mo-1.0Cu-6.4Si-1.5B) Chen et al.<sup>153</sup> successfully brazed two Inconel 625 pieces. A maximum shearing strength of 443 MPa was achieved in the sample brazed with MBF-51 and a maximum shearing strength of 300 MPa was achieved in the sample brazed with VZ-2106. The MBF-51 brazed joint includes the matrix enriched with Ni/Cr, borides distributing along the grain boundaries and coarse Nb<sub>6</sub>Ni<sub>16</sub>Si<sub>7</sub> while VZ-2106 brazed joint includes the matrix enriched with Ni/Cr, coarse Nb<sub>6</sub>Ni<sub>16</sub>Si<sub>7</sub> and Nb<sub>6</sub>Ni<sub>16</sub>Si<sub>7</sub> precipitates along the grain boundaries. Ojo et al.<sup>154</sup> diffusion brazed Inconel 738 alloy using two commercial filler metals, which were Amdry 'DF3' and Nicrobraz 150. Effect of the gap size and process parameters (brazing time, brazing temperature) were investigated carefully. Xiong et al.<sup>155</sup> brazed silicon carbide ceramic to GH3044 wrought Ni-base superalloy with a newly developed CoFeNi(Si,B)CrTi filler metal foil (40 μm). The filler metal is a CoFeNi-base alloy including 8%-15% Cr and 14-21% Ti (wt. pct.).

The DTA results shows this filler metal has a liquidus temperature of 1111 °C and the brazing temperature was fixed at 1150 °C. A maximum shearing strength of 62.5-64.6 MPa was achieved.

### **2.5.3 Cu-based filler metals for brazing of Ni-base superalloys**

Chen et al.<sup>156</sup> used the copper foil with a thickness of 50 µm to braze the Inconel 625 alloy. The Ni-based super-alloy was brazed at 1433K for 1800 s, showing a shearing strength of 470 MPa. Ductile dimple fracture with sliding marks was observed. Decreasing the brazing temperature reduced the shearing strength due to the formation of isolated solidification shrinkage voids. Increasing the temperature also reduced the shearing strength to 260 MPa because the isolated solidification shrinkage voids got coarser. Cu foil shows the potential of being filler metal for brazing of Inconel 625 alloy filler metal.

### **2.5.4 Advantages of HEA as filler metal for brazing of Ni-base superalloy**

HEA can be excellent potential filler metals for the brazing of Ni-based super-alloys due to the following reasons. (1) The good ductility of HEA filler metal will result in a weld having better ductility (2) The HEA filler metal contains fast diffusion elements such as Fe, Co and Ni in Ni-based super alloy at brazing temperature (around the solidus line of Ni-based super alloys). (3) Brazing could preclude liquation cracking of Ni-based super alloy, which is often observed during the fusion welding process of Ni-based super alloy. (4). Brazing requires a narrow solidus-liquidus range. And HEA has a single solid solution, which means a zero solidus-liquidus range. This zero solidus-liquidus range makes HEA an excellent candidate for the brazing filler metals. Table 2.2 shows the melting ranges of the common Ni-base superalloys.

Table 2.2 Melting ranges of typical HEAs

Ni-base superalloy	solidus T(°C)	liquids T(°C)
ATI 718Plus	1260	1343
Astrloy	1210	1340
CMSX2	1330	1390
CMSX4	1312	1382
CMSX6	1277	1337
CMSX10	1380	1419
Hastelloy X	1260	1355
Hasterlloy S	1335	1380
Inconel 600	1354	1413
Inconel 718	1260	1336
Inconel 625	1290	1350
MA758	1375	>=1375
MAR-M2000	1315	1392
Nimonic 80A	1320	1365
Nimonic 105	1290	1345
Nimonic 242	1225	1340
Nimonic 263	1300	1355
Nimonic 75	Liquids temperature=1410	
Nimonic 90	1310	1380
Nimonic 101	1260	1345
Nimonic 115	1260	1315
Nimonic 942	1240	1300
Nimonic PE11	1280	1350
Nimonic PE16	1310	1355
Nimonic PK33	1300	1345
Rene 108	1127	1496
Rene 41	1307	1343
Rene 80	1280	1320
PM1000	Melting point=1408	
Udimet 500	1285	1360
Udimet 700	1210	1375
Udimet 520	1260	1405
Udimet 41	1294	1345
Waspaloy	1330	1360

## CHAPTER 3

### EXPERIMENTS

#### 3.1 Brazing of Inconel 600 alloy by $\text{Fe}_5\text{Co}_{20}\text{Ni}_{20}\text{Mn}_{35}\text{Cu}_{20}$ HEA filler

##### 3.1.1 Design of HEA filler

Fe, Co, Ni, Mn and Cu are consistent in the 4<sup>th</sup> period of periodical table of elements. They have similar atomic radius, mechanical properties and chemical properties. HEAs consisted of these elements are predicted to form a simple phase structure. It is also reported that HEA systems including Fe, Co and Ni usually have a combination of high strength and good ductility.<sup>157,158</sup> So Fe, Co, Ni, Cu and Mn are chosen. A Thermo-Calc calculation using HEA1.0 database is made. According to the calculation result shown in Figure 3.1 and 3.2, the HEA with the composition of (Fe:5%, Co: 20%, Ni:20%, Cu:20%, Mn: 35%, atomic percent) is expected to have a simple FCC phase structure after fast cooling and a melting range of 1090-1142°C. As is shown in Table 3.1, the thermal expansion coefficient of the HEA ( $\text{Fe}_5\text{Co}_{20}\text{Ni}_{20}\text{Mn}_{35}\text{Cu}_{20}$ ) calculated by mixing rule is  $16.62 \times 10^{-6}/\text{K}$  at room temperature, similar to that of Inconel 600 alloy,  $13.3 \times 10^{-6}/\text{K}$ . The mixing entropy ( $\Delta S_{mix}$ ), mixing enthalpy ( $\Delta H_{mix}$ ) and atomic size difference parameter ( $\delta$ ) are  $12.33\text{J/mol} \times \text{K}$ ,  $-0.52\text{KJ/mol}$  and 1.16%. The results also show a good agreement with the reported HEA formation rule. Above all,  $\text{Fe}_5\text{Co}_{20}\text{Ni}_{20}\text{Mn}_{35}\text{Cu}_{20}$  HEA is chosen to be fabricated and used as the filler metal for brazing of Inconel 600 alloy.

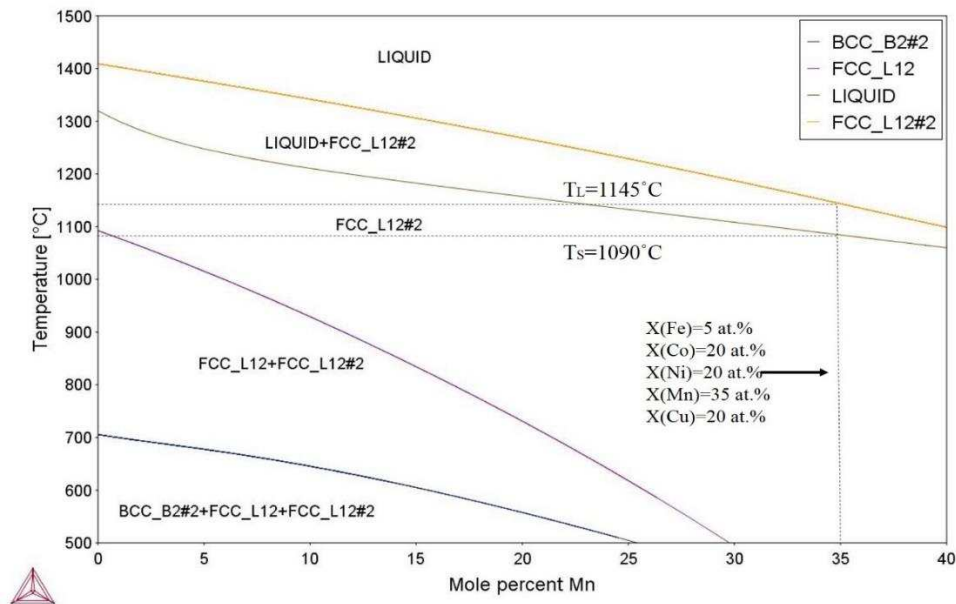


Figure 3.3 Phase diagram of  $\text{Fe}_x\text{Co}_{20}\text{Ni}_{20}\text{Mn}_y\text{Cu}_{20}$  system calculated by Thermo-Calc using HEA 1.0 database

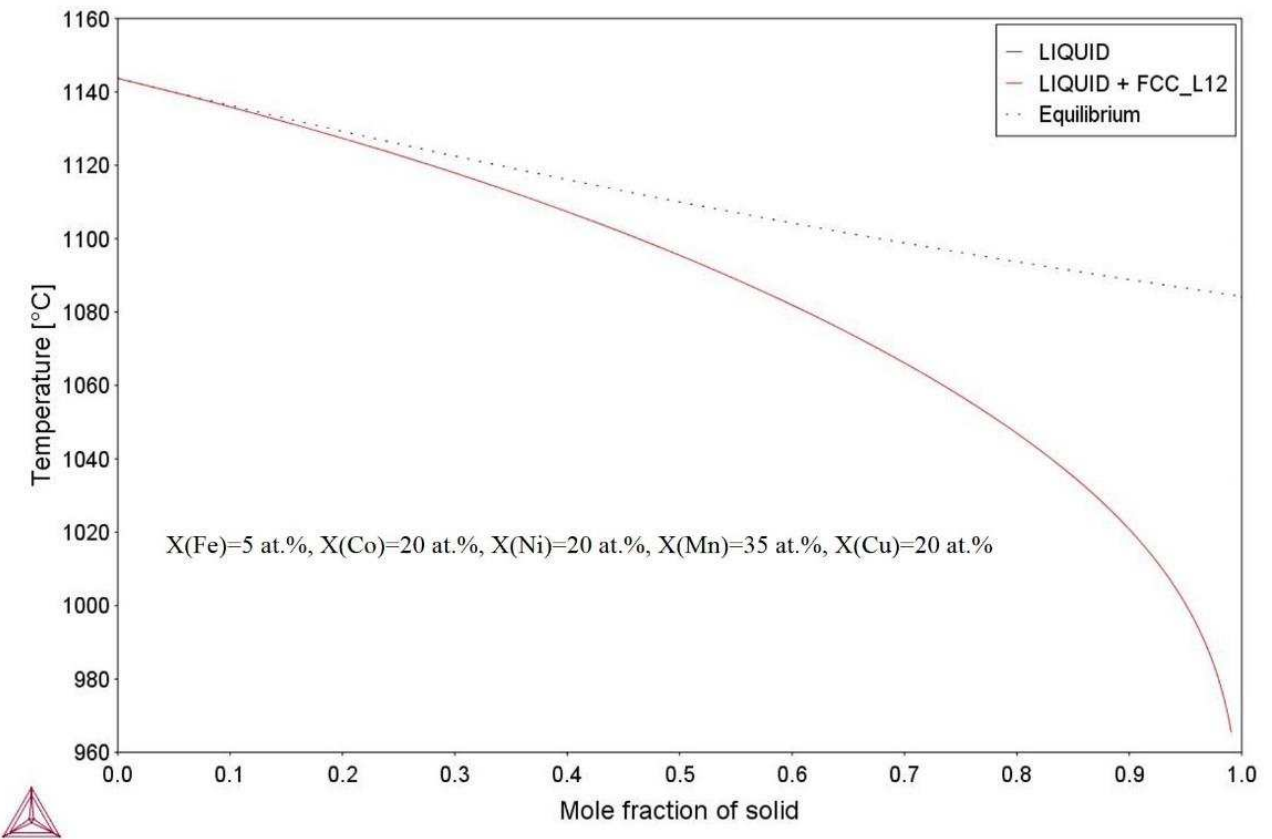


Figure 3.4 Scheil diagram of the  $\text{Fe}_5\text{Co}_{20}\text{Ni}_{20}\text{Mn}_{35}\text{Cu}_{20}$  system calculated by Thermo-Calc using HEA 1.0 database

Table 3.3 Mixing enthalpy, mixing entropy, atomic size difference, linear thermal expansion and valance electron concentration for Fe<sub>5</sub>Co<sub>20</sub>Ni<sub>20</sub>Mn<sub>35</sub>Cu<sub>20</sub> HEA system

Element couple	Fe-Co	Fe-Ni	Fe-Mn	Fe-Cu	Co-Ni	Co-Mn	Co-Cu	Ni-Mn	Ni-Cu	Mn-Cu	Total
$\Delta H_{mix}$ (KJ/mol)	-0.04	-0.08	0	0.52	0	-1.4	0.96	-2.24	0.64	1.12	-0.52
Element	Fe	Co	Ni	Mn	Cu	Total					
Mole fraction	0.05	0.2	0.2	0.35	0.2						
$\Delta S_{mix}$ (J/mol*K)	1.25	2.68	2.68	3.05	2.68	12.34					
Element	Fe	Co	Ni	Mn	Cu	$\delta$					
Mole fraction	0.05	0.2	0.2	0.35	0.2						
Atomic radius (pm)	126	125	124	127	128	126.15					
$C_i(1-r_i/r)*(1-r_i/r)$	7.07E-08	1.66E-05	5.81E-05	1.59E-05	4.30E-05	0.0115					
Element	Fe	Co	Ni	Mn	Cu	Total					
Mole fraction	0.05	0.2	0.2	0.35	0.2						
linear thermal expansion ( $\mu$ /K)	12	12	13	22	16.6	16.62					
Element	Fe	Co	Ni	Mn	Cu	Total					
Mole fraction	0.05	0.2	0.2	0.35	0.2						
Valance electron concentration	8	9	10	7	11	8.85					
C <sub>i</sub> : mole fraction of element i											
r <sub>i</sub> : atomic radius of element i											
r: average atomic radius of HEA											

$$\Delta S_{mix} = \sum_{i=1}^n -RC_i \ln C_i \quad \text{Equation 1}$$

$$\Delta H_{mix} = \sum_{i=1, i \neq j}^n -4C_i C_j \Delta H_{mix}^{AB} \quad \text{Equation 2}$$

$$\Omega = |TS_{mix}| / \Delta H_{mix} \quad \text{Equation 3}$$

$$r = \sum_{i=1}^n C_i r_i \quad \text{Equation 4}$$

$$\delta = \sqrt{\sum_{i=1}^n C_i \left(1 - \frac{r_i}{\sum_{i=1}^n C_i r_i}\right)^2} \quad \text{Equation 5}$$

$$VEC = \sum_{i=1}^n C_i (VEC)_i \quad \text{Equation 6}$$

$$\alpha = \sum_{i=1}^n C_i \alpha_i \quad \text{Equation 7}$$

Here  $\delta$  evaluates the atomic size difference;  $C_i$  is the molar fraction of element i;  $r$  is the atomic radius of the HEA system;  $r_i$  is the atomic radius of element i;  $\Delta H_{AB}^{mix}$  is the change of enthalpy before and after the mixing of A and B;  $T$  is the temperature;  $\Delta H_{mix}$  is the change of enthalpy before and after the mixing

of the multi-component alloy and  $\Delta S_{mix}$  is the change of entropy before and after the mixing of the multi-component alloy.  $\Omega$  evaluates the change of Gibbs free energy before and after the mixing.

### 3.1.2 Arc melting fabrication of HEA

HEA ingots were fabricated by arc melting the Fe, Co, Ni, Mn and Cu raw materials with the purity higher than 99.9% weight percent in an argon atmosphere. All the pure metals were purchased on Alfa Aesar website. As is shown in Figure 3.3 and 3.4, besides the pure metals in position 1 and 2, two titanium plates were also put into the furnace in position 3 and 4 in order to absorb the oxygen during arc melting. Once the metals were placed in the furnace, the vacuum pump was turned on for three minutes to remove the air inside the furnace. The vacuum level in the furnace can be as low as 1500-2000Pa. Argon gas with a purity of 99.9999% was then flowed into the furnace body for three minutes. The pressure of argon gas was set at 30 MPa. This recycle was repeated three times before arc melting. Titanium plates were melted two times before melting pure metals. The voltage and the current of the arc melting furnace were fixed at 220 V and 150 A. The pressure of argon gas was turned down to 10 MPa during melting. After melting, the solidified ingot was cooled on a water-cooled Cu hearth. In order to confirm the homogeneity of the HEA, the solidified button was flipped and re-melted for four times. After taken out of the arc melting furnace, the button was cut by alumina blade, ground by silicon carbide sand papers (80, 240, 320, 400, 600, 800, and 1200 mesh) and polished by diamond paste (6, 3, and 1  $\mu\text{m}$ ) for wetting angle test, Vickers hardness test, OM, SEM observation. The microstructure of the wetting angle test sample was observed on a 50X-1000X two light Zeiss optical microscope (OM) and a Philips XL-30 scanning electron microscope (SEM) equipped with an energy dispersive spectrometer (EDS). The dwell time, indents distance and force of the Vickers hardness were fixed at 10 s, 60  $\mu\text{m}$  and 50 g. A small piece with a weight of 40mg was cut to take the DSC test. The sample was heated to 1400  $^{\circ}\text{C}$  with a rate of 15  $^{\circ}\text{C}/\text{min}$  in the argon atmosphere then cooled with the furnace to room temperature. Two HEA cylinders with a diameter of 2mm and a height of 4mm were machined along the axial direction for compression test on CSM-Alliance mechanical test machine. Before the compression test, the top and bottom surface of the sample were polished from using 6, 3 and 1  $\mu\text{m}$  grit to reduce the friction between the fixture and the sample. The compression rate was set at  $1.6 \times 10^{-3}$  mm/sec. The CSM-Alliance machine, whose load frame is relatively low accurate to measure the load. It has an uncertainty of 89N.

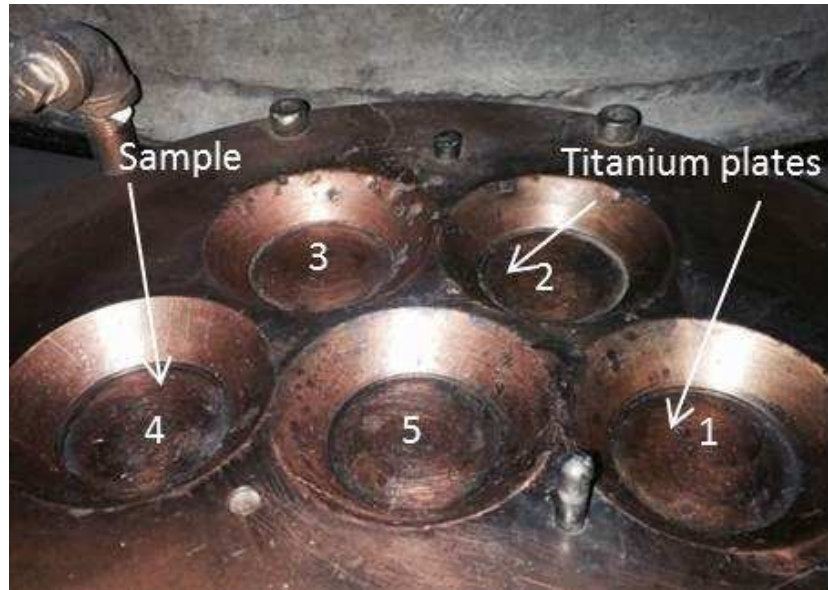


Figure 3.5 Photograph showing positions of the HEA samples and Ti buttons in the arc melting furnace

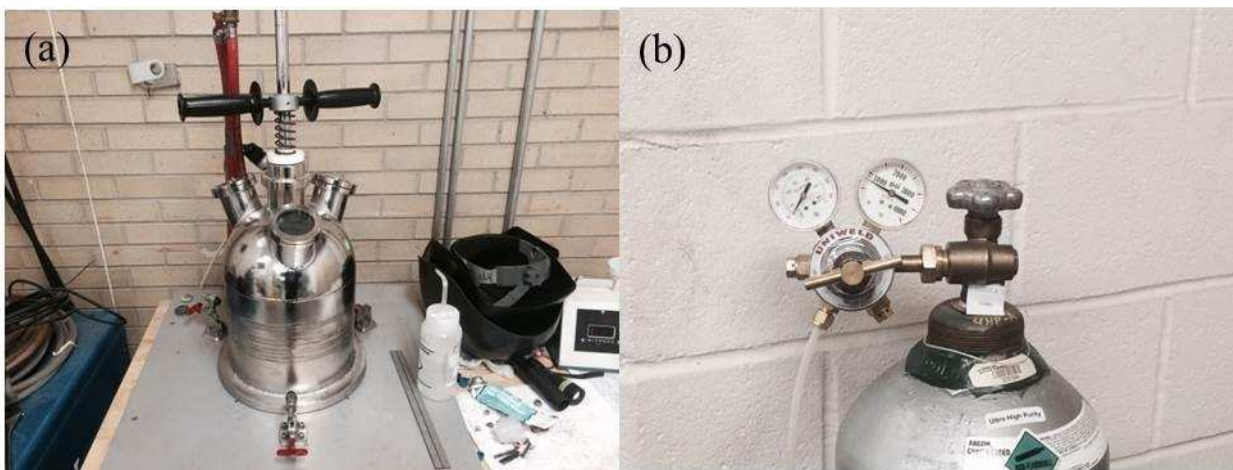


Figure 3.6 Photographs of (a) the arc melting furnace and (b) argon gas tank used in this study

### 3.1.3 HEA/Inconel 600 wetting angle test

An Inconel 600 alloy plate with a size of 20×10×6mm was grinded (80, 240, 320, 400, 600, 800, and 1200 mesh) with silicon carbide sand paper and polished with diamond paste (6, 3, and 1 μm). A small HEA cubic piece with a weight of 0.10 g was placed in the center on the surface of the polished Inconel 600 alloy plate. The plate with the HEA piece was then put into the vacuum furnace. The mechanical pump and diffusion pump attracted to the vacuum furnace were started. The heating power source was started after the vacuum level reached  $10^{-5}$  torr. As is shown in Figure 3.5, the furnace was first heated to the brazing temperature (1160, 1180, 1200, and 1250 °C) with a rate of 15 °C/min and kept at the brazing temperature for 30 min. After that the heating power source was shut down and the samples were cooled

with the furnace. The pumps were not stooped until the temperature measured by the K-type thermocouples dropped to 45 °C. The furnace was opened 10 min after both mechanical pump and diffusion pump was shut down. The cross sections of the samples were cut along the lines shown in Figure 3.6, grinded with silicon carbide sand papers (80, 240, 320, 400, 600, 800, and 1200 mesh) and polished with diamond paste (6, 3, and 1  $\mu\text{m}$ ) for OM, SEM, EDS, and hardness test. The microstructure of the wetting angle test sample was observed on a 50-1000X two light Zeiss optical microscope (OM) and a Philips XL-30 scanning electron microscope (SEM) equipped with an energy dispersive spectrometer (EDS). The dwell time, indents distance and force of the Vickers hardness were fixed at 10 s, 60  $\mu\text{m}$  and 50 g.

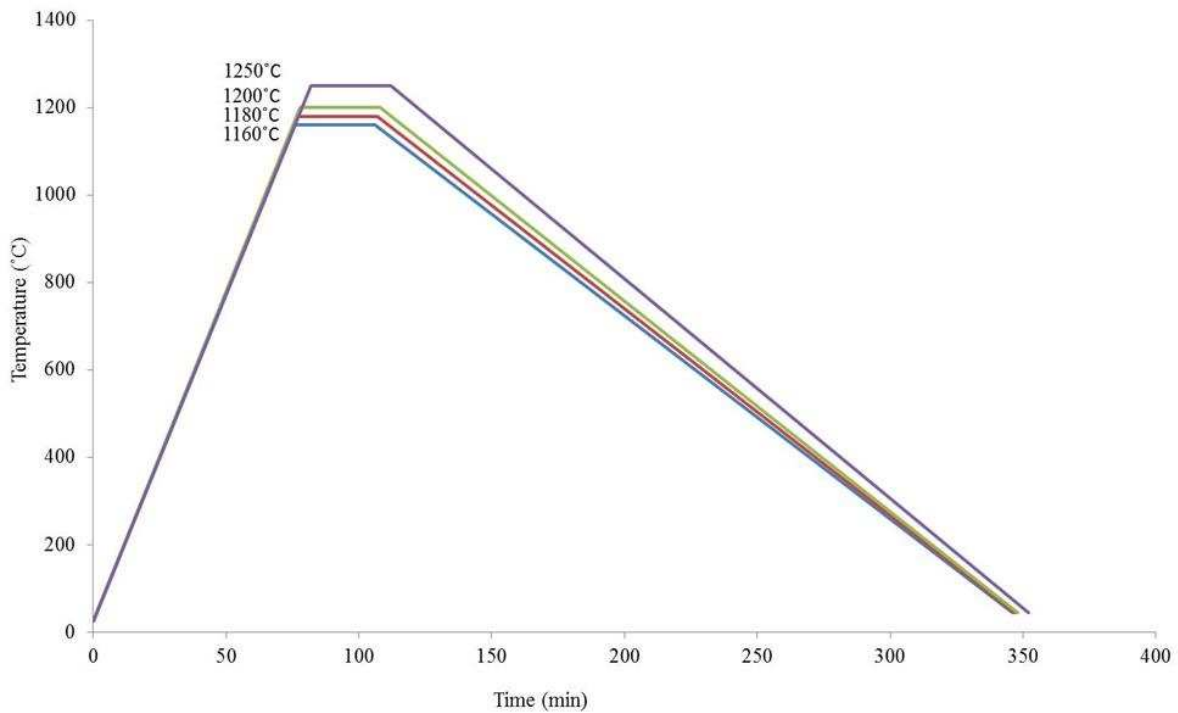


Figure 3.7 Temperature-time curves of wetting angle tests at 1160, 1180, 1200, and 1250 °C for 30 min

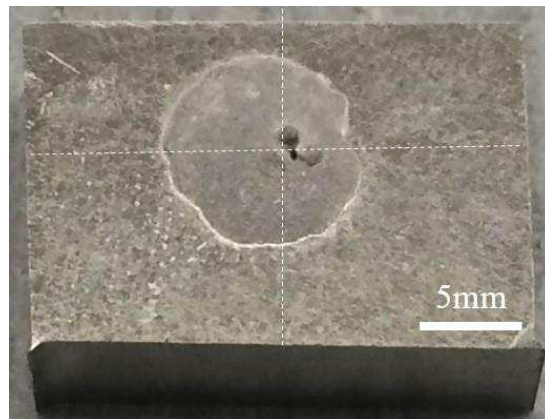


Figure 3.8 Top view of the wetting angle sample

### 3.1.4 Fabrication of HEA foils

The HEA buttons were cut into small pieces with a size of 5×5×2 mm for rolling. As is shown in Figure 3.7 is the roller in the physical metallurgy lab. The rollers were rotating in a speed of 0.2 m/s. There is a wheel on the top of the up-roller which could be used to adjust the distance between two rollers. The distance can be decreased by anti-clockwise rotating the wheel. The distance was decreased by 30 μm each time. The pieces were rolled into foils with different thicknesses (300, 200, 100, and 50 μm). The rollers were cleaned by ethanol and coated with lubricating oil before the rolling test in order to reduce the friction between HEA piece and the rollers.

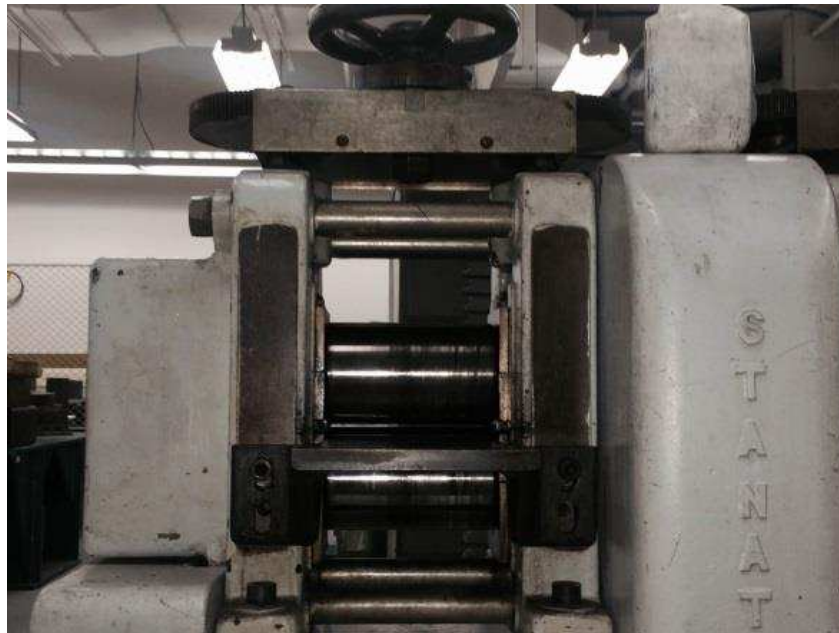


Figure 3.9 Rolling mill used to fabricate HEA foils in the physical metallurgy lab

### 3.1.5 Brazing of Inconel 600 alloy by HEA filler foils

The sample arrangement of the brazing test is shown in Figure 3.8. As rolled HEA filler foils were insert into the gap between two Inconel 600 alloy plates. The overlapping area is 5×5mm. Samples were placed into the vacuum furnace. The furnace was then heated to 1200 °C from room temperature in a speed of 15 °C/min and kept at 1200 °C for different time (15, 30, 45, 60, 90, and 120 min). After that the heating power source was shut down and the samples were cooled with the furnace. Figure 3.9 shows the temperature-time curves of the brazing test. The samples were not taken out of the furnace until the temperature dropped to 45 °C. Figure 3.10 shows the schematic diagram of the shear test. Shear tests were performed on an Instron universal testing machine with a constant tensile speed of 0.5 mm/min. Each shear test was repeated at least two times in order to confirm the shear strength. DIC equipment was used to

monitor the strain distribution among the shear test sample. Before the shear test, the sample was first painted by “boron nitride spray II” produced by Momentive and then painted by flat black cover produced Rust-Oleum. Photographs of samples were taken each second by the camera during the shear tests.

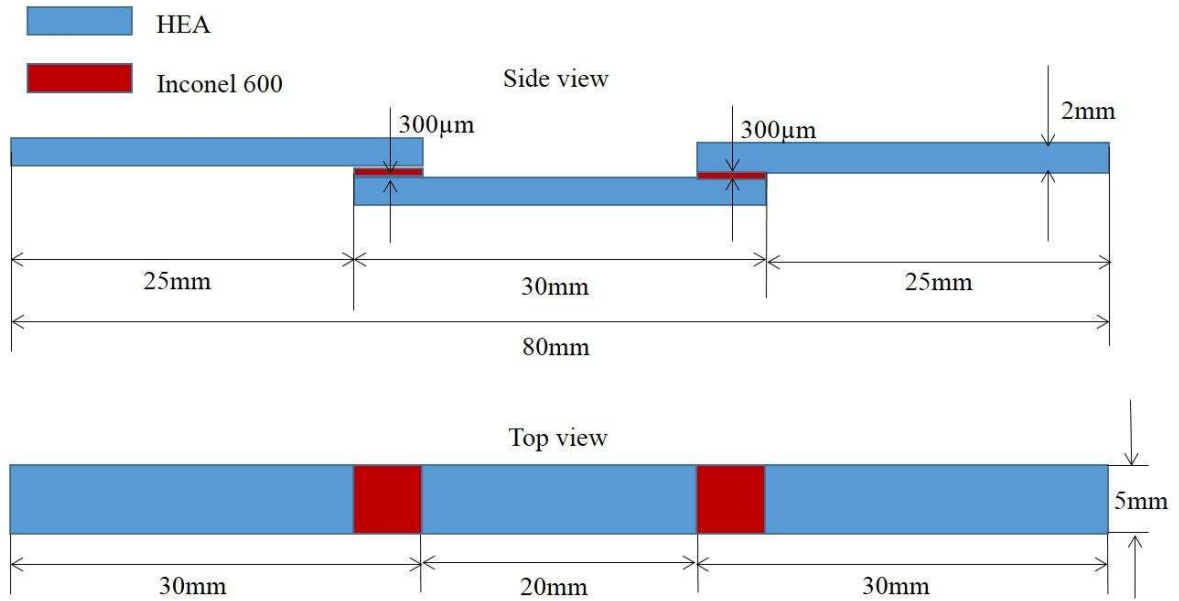


Figure 3.10 Sample arrangement of the brazing tests. HEA foil is used as filler metal and Inconel 600 alloy is used as the base metal

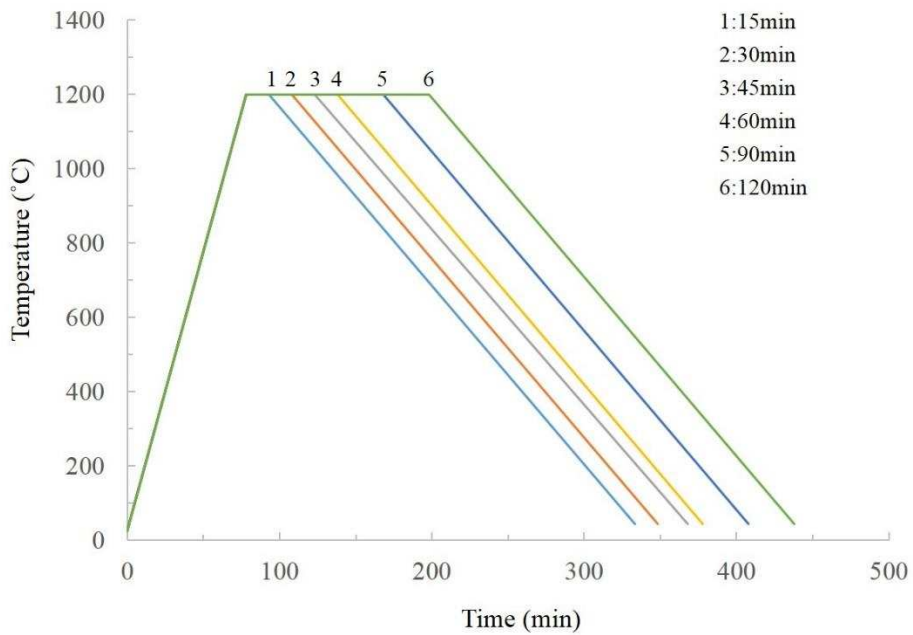


Figure 3.11 Temperature-time curves of brazing test at 1200 °C for 15, 30, 45, 60, 90, and 120 min

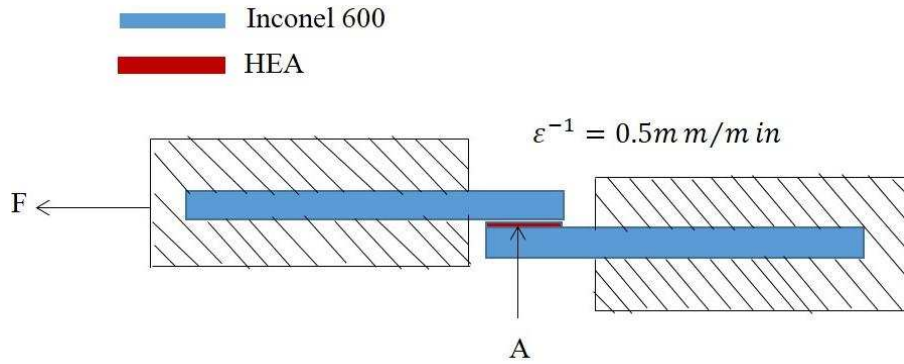


Figure 3.12 Schematic diagram of the brazed shear test specimen

### 3.2 Interface reaction between HEA and aluminum melt

#### 3.2.1 Arc melting fabrication of HEA

HEA ingots were fabricated by arc melting the Fe, Co, Ni, Al and Si raw materials with the purity higher than 99.9% weight percent in an argon atmosphere. All the pure metals were purchased on Alfa AeSar website. As is shown in Figure 3.3 and 3.4, besides the pure metals in position 1 and 2, two titanium plates were also put into the furnace in position 3 and 4 in order to absorb the oxygen during arc melting. Once the metals were placed in the furnace, the vacuum pump was turned on for three minutes to remove the air inside the furnace. The argon gas with a purity of 99.9999% was then flowed into the furnace body for three minutes. The pressure of argon gas was set at 30 MPa. This recycle was repeated three times before arc melting. Titanium plates were melted two times before melting pure metals. The voltage and the current of the arc melting furnace were fixed at 220 V and 150 A. The pressure of argon gas was turned down to 10 MPa during melting. After melting, the solidified ingot was cooled on a water-cooled Cu hearth. In order to confirm the homogeneity of the HEA, the solidified button was flipped and re-melted for four times. After taken out of the arc melting furnace, the button was cut by alumina blade, grinded by silicon carbide sand papers (80, 240, 320, 400, 600, 800, 1200 mesh) and polished by diamond paste (6, 3, 1 $\mu$ m) for wetting angle test, Vickers hardness test, OM, SEM observation. The microstructure of the wetting angle test sample was observed on a 50X-1000X two light Zeiss optical microscope (OM) and a Philips XL-30 scanning electron microscope (SEM) equipped with an energy dispersive spectrometer (EDS). The dwell time, indents distance and force of the Vickers hardness were fixed at 10 s, 60  $\mu$ m and 50 g. A small piece with a weight of 40mg was cut to take the DSC test. The sample was heated to 1500 °C with a rate of 15 °C/min in the argon atmosphere then cooled with the furnace to room temperature. Two HEA cylinders with a diameter of 3mm and a height of 6mm were machined along the axial direction for compression test on CSM-Alliance mechanical test machine. Before the compression test, the top and bottom surface of the

sample were polished from 6, 3  $\mu\text{m}$  to 1 $\mu\text{m}$  in order to reduce the friction between the fixture and the sample. The compression rate was set at  $2.4 \times 10^{-3} \text{mm/sec}$ . The CSM-Alliance machine, whose load frame is relatively low accurate to measure the load. It has an uncertainty of 20 lbs.

### 3.2.2 Oxidation of HEA

The as cast HEA button was cut into small cubes with a length of 5mm and placed in an alumina crucible with an inner diameter of 25mm, an outer diameter of 30 mm, a height of 25mm. The oxidation experiment was taken in a regular furnace in the physical metallurgy lab. After putting the sample into the furnace, the heating power source was started. Figure 3.11 shows the temperature-time curve of the interface reaction experiment. The temperature increased to the oxidation temperatures (800  $^{\circ}\text{C}$ , 1000  $^{\circ}\text{C}$ ) and kept at the oxidation temperature for 5 hours. The crucible with the oxidized alloy inside was taken out of the furnace immediately after 5 hours heating. The oxidized HEA was mounted, grinded with silicon carbide sand papers (80, 240, 320, 400, 600, 800, 1200 mesh), polished with diamond paste (6, 3, 1 $\mu\text{m}$ ) for microstructure observation by OM and SEM. The microstructure of the oxidized alloy was observed on a 50X-1000X two light Zeiss optical microscope (OM) and a Philips XL-30 scanning electron microscope (SEM) equipped with an energy dispersive spectrometer (EDS).

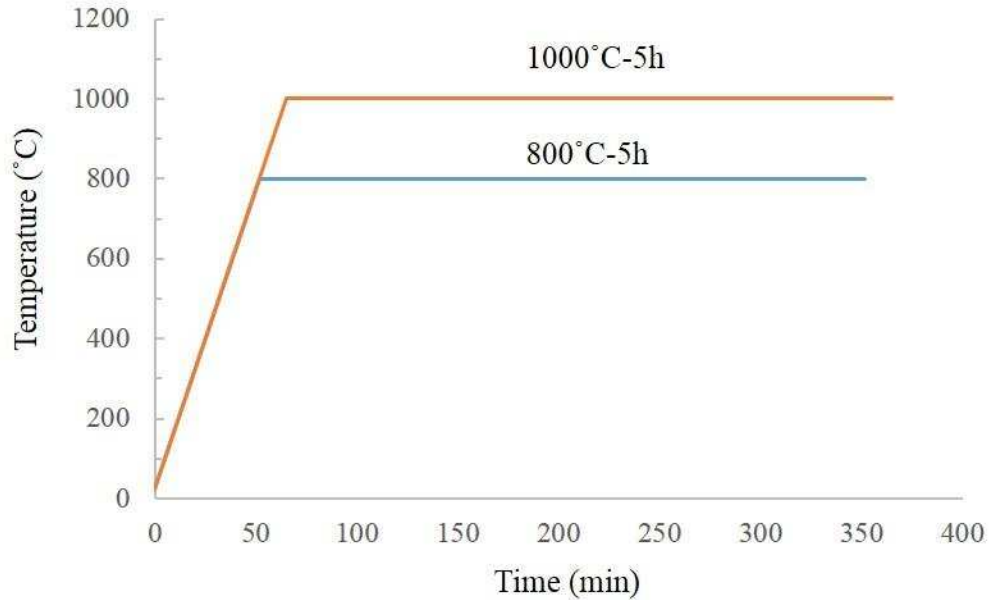


Figure 3.13 Temperature-time curves for oxidation of as-cast FeCoNi(AlSi)<sub>0.2</sub> HEA

### 3.2.3 HEA-aluminum melt interface reaction

An aluminum ingot with a purity of 99.9999% weighted 6g was placed into an alumina crucible with an inner diameter of 25mm, an outer diameter of 30 mm and a height of 25mm. The interface reaction experiment between as cast HEA, oxidized HEA and aluminum melt was taken in a regular furnace in the physical metallurgy lab. After putting the crucible with aluminum ingot into the furnace, the heating power source was started so that the temperature was increased to 730 °C in a speed of 10 °C/min. It can be observed that the aluminum ingot was completely melted after kept at 730 °C for half an hour. After that the slags and oxidation layers on the surface of aluminum melt was removed by a ceramic layer. The oxidized HEA cubes were then put into the aluminum melt and kept at 730 °C for another one hour in the regular furnace. Figure 3.12 shows the temperature-time curve of the interface reaction experiment. The crucible was taken out of the furnace after one hour and cooled in the air. After taken out, the crucible was broken by a hammer in order to take out the solidified aluminum ingot with HEA inside. The cross section of the solidified sample was cut with alumina blade, grinded with silicon carbide sand papers (80, 240, 320, 400, 600, 800, 1200 mesh) and polished with diamond paste (6, 3, 1 $\mu$ m) for microstructure observation by OM and SEM. The microstructure of the interface was observed on a 50X-1000X two light Zeiss optical microscope (OM) and a Philips XL-30 scanning electron microscope (SEM) equipped with an energy dispersive spectrometer (EDS).

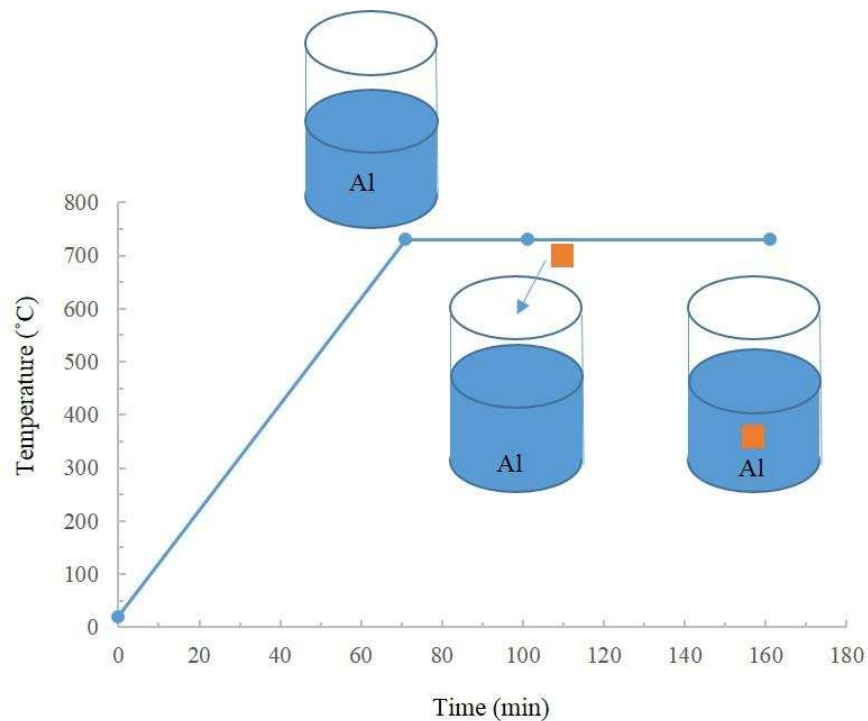


Figure 3.14 Temperature-time curves of the interface reactions between as-cast HEA, oxidized HEA, pure Fe and aluminum melt

## CHAPTER 4

### BRAZING OF INCONEL 600 BY HEA FILLER FOIL

#### 4.1 Design of the composition of HEA filler

In order to design the composition of HEA filler foil, both of the requirements to form HEA and filler metal for brazing of Inconel 600 alloy need to be satisfied. In order to form HEA, the elements should have similar atomic radius and chemical properties. According to the literature review, usually the consistent elements in the same period (3<sup>rd</sup>, 4<sup>th</sup> period) on the periodical elements are chosen. Several principles have also been proposed to predict the phase formation of HEA by Zhang et al<sup>69</sup>. In this study, three main parameters are taken in consideration. First,  $\delta$  evaluating the atomic radius difference of elements should be lower than 6%. The definition of  $\delta$  is listed in Equation 5 where  $C_i$  is the atomic fraction of the  $i^{\text{th}}$  element and  $r_i$  is the atomic radius of the  $i^{\text{th}}$  element.  $\Omega$ , evaluating the entropy change before and after mixing should be larger than 1.1. The definition of  $\Omega$  is listed in Equation 1, 2 and 3 where  $\Delta H_{mix}^{AB}$  is the mole mixing enthalpy of element A and element B. Third, VEC is defined in Equation 6 where  $(VEC)_i$  is the valance electron concentration of the  $i^{\text{th}}$  element. A FCC HEA will form if the average valance electron concentration is larger than 8 while a BCC HEA will form if the average valance electron is lower than 8. In this study, because we are designing a filler metal for brazing of Inconel 600 Ni-base superalloy and Inconel 600 alloy has a single FCC phase structure, in this study a FCC HEA is required. It means the valance electron concentration should be larger than 8.

There are also several requirements to be satisfied while designing a filler metal for brazing of Ni-base superalloys. First, several elements with similar high temperature chemical properties should be contained in the filler metal in order to form an excellent bonding between filler metal and Ni-base superalloys. Second, during the brazing of Ni-base superalloys, the filler metal is melted while the Ni-base superalloy keeps at solid state, at least 100 °C below its solidus line. So the liquidus line of the filler metal should be at least 100 °C lower than the solidus line of the Ni-base superalloy or the complex shapes of the Ni-base superalloy made components will be damaged due to the high temperature softening. Third, the filler metal should have similar hardness, strength with Ni-base superalloy. Fourth, the filler metal should have similar linear expansion coefficient with Ni-base superalloy in order to avoid the cracking after brazing. The definition of the linear expansion coefficient is listed in Equation 7 where  $\alpha_i$  is the linear thermal expansion of the  $i^{\text{th}}$  element.

According to requirements stated above, the composition of the HEA is determined in the following steps:

1. Ni should be included into the filler metal. Moreover, Fe, Co and Ni with similar atomic size and chemical properties, are consistent elements in the 3<sup>rd</sup> period on the periodical table of the elements. Fe and Co are chosen as components of the HEA filler metal because their similarity with Ni.
2. As stated in the previous paragraph, the liquidus temperature of the HEA filler metal should be at least 100 °C lower than the solid temperature of Inconel 600 alloy. The solidus temperature of Inconel 600 is 1354 °C so the liquidus temperature of HEA filler should be lower than 1250 °C. However, Fe, Co and Ni (Fe:1538 °C, Co:1495 °C, Ni:1455 °C) all have a melting point higher than 1400 °C. Lower melting point elements should be introduced into the braze alloy. In addition, these low melting point elements are supposed to have similar atomic size and chemical properties with Fe, Co and Ni in order to form a HEA. Mn and Cu (Mn:1246 °C, Cu:1080 °C) have relatively lower melting point than Fe, Co and Ni. They are also the nearest neighbors of Fe, Co and Ni in the periodical table of elements having similar atomic size and chemical properties with Fe, Co and Ni. So Mn and Cu were introduced into the system.
3. It is also proposed that the filler metal should have comparable mechanical properties with Ni-base superalloy base metal. Inconel 600 alloy is a single FCC solid solution so one target during designing the HEA filler metal is to achieve a FCC structure (single FCC or two FCC phases). It is already reported that FeCoNi ternary alloy has a single FCC phase structure and the addition of Mn into the FeCoNi is also good for maintaining of FCC phase structure because Mn is a FCC stabilizing element although it is a BCC element.

After the Fe-Co-Ni-Mn-Cu system was determined here, a  $Fe_xCo_{20}Ni_{20}Mn_yCu_{20}$  ( $x+y=40$ ) phase diagram is calculated by Thermo-Calc software using HEA 1.0 database, which is newly published by Thermo-Calc company. As is shown in Figure 4.1,  $Fe_5Co_{20}Ni_{20}Mn_{35}Cu_{20}$  is supposed to have a single FCC phase structure and a melting range of 1090-1148 °C, which satisfies the melting range requirement on filler metal for brazing of Ni-base superalloys. According to the principle proposed by Zhang et al<sup>69</sup>,  $\delta \leq 6\%$ ,  $\Omega \geq 1.1$  and  $VEC > 8$  should be achieved to form a FCC phase structure HEA. Here,  $\delta$ ,  $\Omega$ , and  $VEC$  were calculated as 1.16%, 7.09 and 8.85, satisfying the requirement to form a FCC HEA. The linear expansion coefficient of the composition at room temperature was calculated as 16.62 $\mu$ /K, similar to the linear expansion coefficient of Inconel 600 alloy (13.6  $\mu$ /K). It is good for bonding between filler metal and Inconel 600 alloy. These parameters are calculated according to equation 1-7 and listed in Table 4.1. Moreover, except the composition, properties and melting range of the base metal, some other factors including gap size, service requirements and cost also need to be considered. Compared with commercial braze alloy, for example, Cusil ABA, the alloy  $Fe_5Co_{20}Ni_{20}Mn_{35}Cu_{20}$  designed in this study excludes the high cost elements such as Ag, Au thus reduces the cost. A eutectic braze alloy (BNi-6, BNi-7, BNi-9) is

recommended for narrow gap brazing while a wide melting range (BNi-1, BNi-2, BNi-3, BNi-4, BNi-5) braze alloy is recommended for wide-gap brazing or braze repair of components. Fe<sub>5</sub>Co<sub>20</sub>Ni<sub>20</sub>Mn<sub>35</sub>Cu<sub>20</sub> has comparable melting range (70°C) with the commercial wide melting range braze alloys. So it is feasible to use Fe<sub>5</sub>Co<sub>20</sub>Ni<sub>20</sub>Mn<sub>35</sub>Cu<sub>20</sub> as a filler metal for wide gap brazing of Inconel 600 Ni-base superalloy. Considering the service environment, it has already been reported that the HEAs with similar composition to Fe<sub>5</sub>Co<sub>20</sub>Ni<sub>20</sub>Mn<sub>35</sub>Cu<sub>20</sub> have excellent oxidation and corrosion resistance. It can be predicted that Fe<sub>5</sub>Co<sub>20</sub>Ni<sub>20</sub>Mn<sub>35</sub>Cu<sub>20</sub> is also supposed to have excellent oxidation, corrosion resistance. Also, Fe<sub>5</sub>Co<sub>20</sub>Ni<sub>20</sub>Mn<sub>35</sub>Cu<sub>20</sub>, having a solidus temperature higher than the service temperature of Inconel 600 alloy, is able to keep stable in service. All the analysis above shows the HEA with a composition of Fe<sub>5</sub>Co<sub>20</sub>Ni<sub>20</sub>Mn<sub>35</sub>Cu<sub>20</sub> is a good potential candidate as a filler metal for brazing of Inconel 600 Ni-base superalloy.

$$\Delta S_{mix} = \sum_{i=1}^n -RC_i \ln C_i \quad \text{Equation 1}$$

$$\Delta H_{mix} = \sum_{i=1, i \neq j}^n -4C_i C_j \Delta H_{mix}^{AB} \quad \text{Equation 2}$$

$$\Omega = |TS_{mix}| / \Delta H_{mix} \quad \text{Equation 3}$$

$$r = \sum_{i=1}^n C_i r_i \quad \text{Equation 5}$$

$$\delta = \sqrt{\sum_{i=1}^n C_i \left(1 - \frac{r_i}{\sum_{i=1}^n C_i r_i}\right)^2} \quad \text{Equation 5}$$

$$VEC = \sum_{i=1}^n C_i (VEC)_i \quad \text{Equation 6}$$

$$\alpha = \sum_{i=1}^n C_i \alpha_i \quad \text{Equation 7}$$

Here  $\delta$  evaluates the atomic size difference;  $C_i$  is the molar fraction of element  $i$ ;  $r$  is the atomic radius of the HEA system;  $r_i$  is the atomic radius of element  $i$ ;  $\Delta H_{AB}^{mix}$  is the change of enthalpy before and after the mixing of A and B;  $T$  is the temperature;  $\Delta H_{mix}$  is the change of enthalpy before and after the mixing of the multi-component alloy and  $\Delta S_{mix}$  is the change of entropy before and after the mixing of the multi-component alloy.  $\Omega$  evaluates the change of Gibbs free energy before and after the mixing.

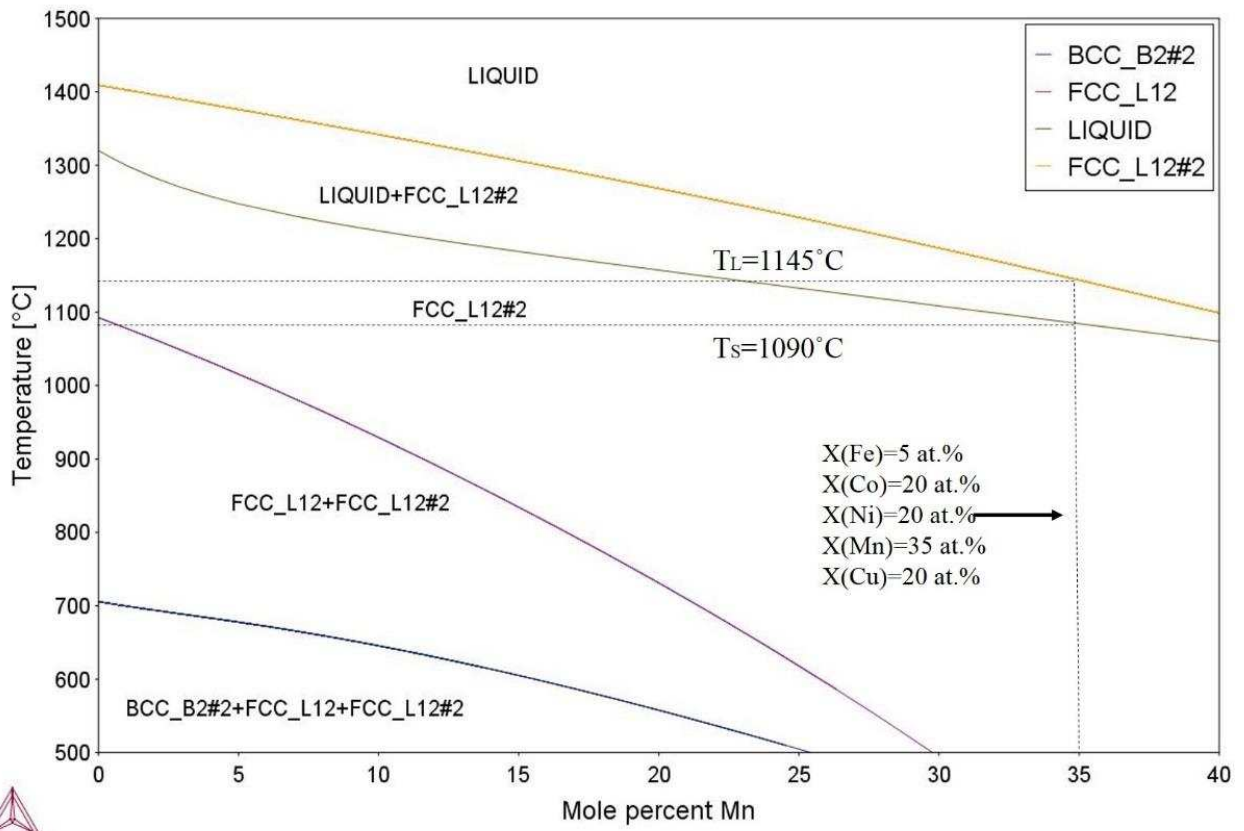


Figure 4.15 Phase diagram for  $\text{Fe}_x\text{Co}_{20}\text{Ni}_{20}\text{Mn}_y\text{Cu}_{20}$  system calculated by Thermo-Calc using HEA 1.0 database

Table 4.4 Mixing enthalpy ( $\Delta H_{mix}$ ), mixing entropy( $\Delta S_{mix}$ ), atomic size difference ( $\delta$ ), thermal expansion coefficient and valance electron concentration of  $Fe_5Co_{20}Ni_{20}Mn_{35}Cu_{20}$  system.

Element couple	Fe-Co	Fe-Ni	Fe-Mn	Fe-Cu	Co-Ni	Co-Mn	Co-Cu	Ni-Mn	Ni-Cu	Mn-Cu	Total
$\Delta H_{mix}$ (KJ/mol)	-0.04	-0.08	0	0.52	0	-1.4	0.96	-2.24	0.64	1.12	-0.52
Element	Fe	Co	Ni	Mn	Cu	Total					
Mole fraction	0.05	0.2	0.2	0.35	0.2						
$\Delta S_{mix}$ (J/mol*K)	1.25	2.68	2.68	3.05	2.68	12.34					
Element	Fe	Co	Ni	Mn	Cu	$\delta$					
Mole fraction	0.05	0.2	0.2	0.35	0.2						
Atomic radius (pm)	126	125	124	127	128	126.15					
$Ci(1-ri/r)*(1-ri/r)$	7.07E-08	1.66E-05	5.81E-05	1.59E-05	4.30E-05	0.0115					
Element	Fe	Co	Ni	Mn	Cu	Total					
Mole fraction	0.05	0.2	0.2	0.35	0.2						
linear thermal expansion ( $\mu/K$ )	12	12	13	22	16.6	16.62					
Element	Fe	Co	Ni	Mn	Cu	Total					
Mole fraction	0.05	0.2	0.2	0.35	0.2						
Valance electron concentration	8	9	10	7	11	8.85					
Ci: mole fraction of element i											
ri: atomic radius of element i											
r: average atomic radius of HEA											

#### 4.2 Fabrication and characterization of $Fe_5Co_{20}Ni_{20}Mn_{35}Cu_{20}$ HEA

Figure 4.2 shows the microstructure of the as-cast  $Fe_5Co_{20}Ni_{20}Mn_{35}Cu_{20}$  HEA. Typical dendrite and inter-dendrite structures are observed. The dendrite has a volume fraction of 90% while the inter-dendrite has a volume fraction of 10%. Figure 4.3 shows the XRD curves of as-cast HEA. The (111) (200) (220) (311) peaks appear on the curve, indicating a FCC phase structure. The alloy shows the exactly same peaks with “FeCoNi” ternary alloy. Although two phases (dendrite area and inter dendrite area) are observed in the microstructure, only the peaks of one FCC phase is detected by XRD test. The possible reason is that both of dendrite and inter dendrite have a FCC phase structure and their crystal parameters are very close. So their peaks are overlapped and can’t be separated from the XRD curve. Such phenomenon has also been found in the HEA system including Fe, Co and Ni with the same atomic fractions. Some papers owned it to the limit amount of the inter dendrite structure. However, it is incorrect in this study because the volume fraction of inter dendrite is 10%. It has already exceeded the minimum fraction which could be detected by XRD test. The structure type of “FeCoNi” ternary alloy is “cF4-Cu” and many types of HEAs including Fe, Co and Ni with equal atomic fraction have been reported to have a “cF4-Cu” crystal structure. In this

study, it is found that the HEA shows a “cF4-Cu” structure even Fe, Co and Ni have different atomic fraction. Mn and Cu has very similar atomic radius with Fe, Co and Ni. So the FCC solid solution structure is still well maintained after introducing Cu and Mn into Fe-Co-Ni system and the crystal parameter nearly keeps constant. The EDS mapping and spotting results are shown in Figure 4.4 to demonstrate the composition difference between dendrite and inter dendrite area. The composition of dendrite area is Fe:6.79 at%, Co:24.19 at%, Ni:20.82 at%, Mn:33.53 at%, Cu:24.19 at% and the composition of inter dendrite area is Fe:3.52 at%, Co:14.11 at%, Ni:19.76 at%, Mn:36.47 at%, Cu:26.14 at%. It can be seen that the dendrite area is rich in Fe, Co while the inter dendrite area is rich in Cu. However, Ni and Mn shows almost the same content in dendrite and inter dendrite area. The content of Ni in dendrite is slightly higher (1.5 at%) than the content of Ni in inter dendrite area while the content of Mn in dendrite is slightly lower (3 at%) than the content of Mn. The boundary segregation behavior of the elements can be explained by the difference of melting points. Among all the five elements included in the alloy, Fe and Co have the largest melting points (Fe:1538 °C, Co:1495 °C) and Cu has the lowest melting point (1080 °C), so during the solidification of the metallic liquid, Fe and Co are solidified first while Cu is ejected to the inter-dendrite area, solidified later. The melting points of Ni and Mn (Ni:1455 °C, Mn:1260 °C) are located between Fe, Co and Cu, so only slight segregation of Ni and Mn is observed. The segregation behavior of elements can be weakened by increasing the cooling rate of metallic liquid, such as increasing the flow of cooling water, decreasing the size of the HEA button and increasing the flow of argon gas. The segregation can also be promoted by decreasing the cooling rate of the metallic liquid. The as-cast HEA is supposed to have a single FCC phase structure, according to the phase diagram calculated by Thermo-Calc using HEA 1.0 database. The most possible reason for the difference between experimental and simulation results is the cooling rate after arc melting is not fast enough so that the composition segregation forms during solidification. Although the composition segregation was observed, the formation of FCC phases in the as-cast HEA is in agreement with the phase formation predicted by value of valance electron concentration. According to the phase formation principle proposed by Guo et al<sup>85</sup>., the HEA with a valance electron concentration lower than 8 is supposed to form a BCC phase structure while the HEA with a valance electron concentration higher than 8 is supposed to form a FCC phase structure. In this study, Fe<sub>5</sub>Co<sub>20</sub>Ni<sub>20</sub>Mn<sub>35</sub>Cu<sub>20</sub> has a valance electron concentration of 8.85 and forms a FCC phase structure.

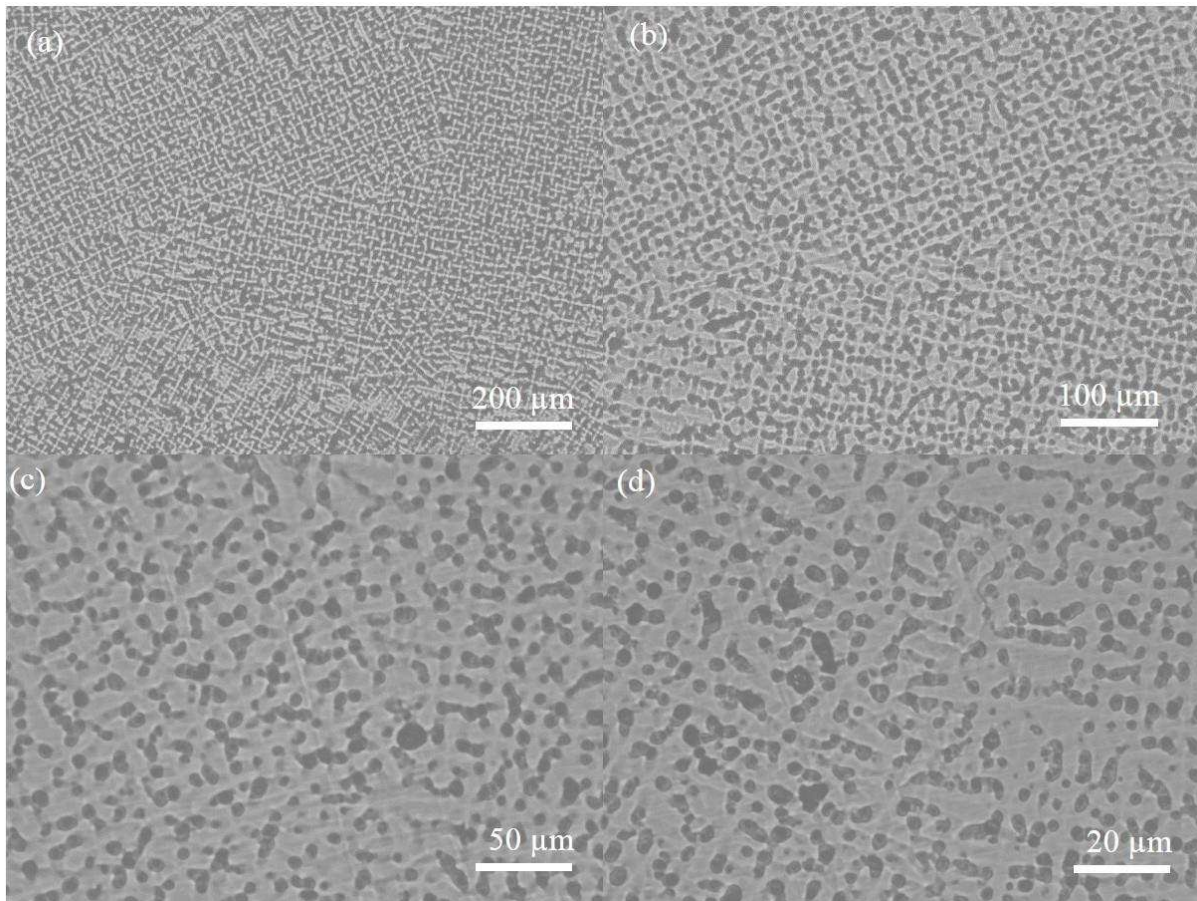


Figure 4.16 (a-d) Microstructure showing the microstructure of as-cast  $\text{Fe}_5\text{Co}_{20}\text{Ni}_{20}\text{Mn}_{35}\text{Cu}_{20}$  HEA

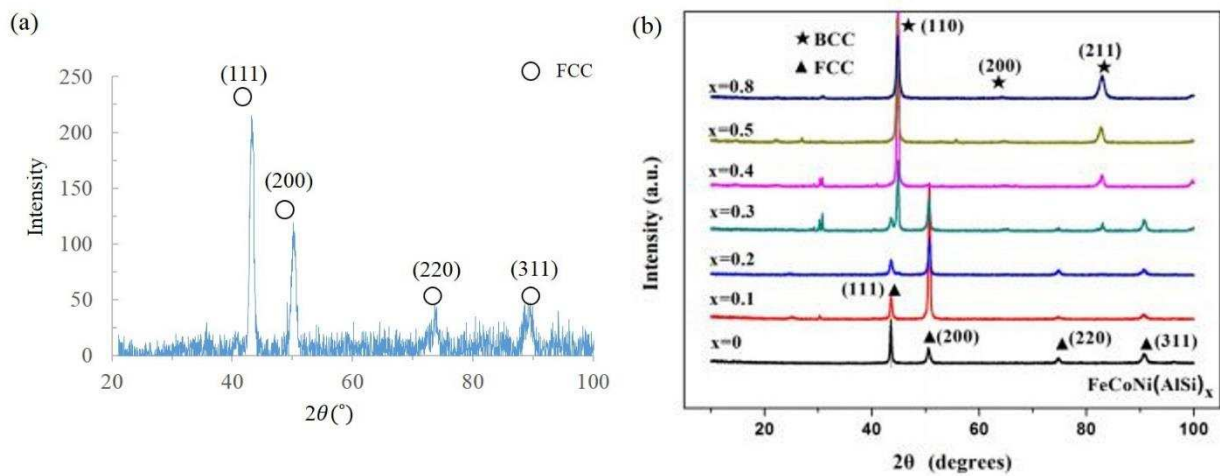


Figure 4.17 XRD curve of the (a) as-cast  $\text{Fe}_5\text{Co}_{20}\text{Ni}_{20}\text{Mn}_{35}\text{Cu}_{20}$  HEA and (b)  $\text{FeCoNi}(\text{AlSi})_x$  ( $x:0-0.8$ )<sup>157</sup>

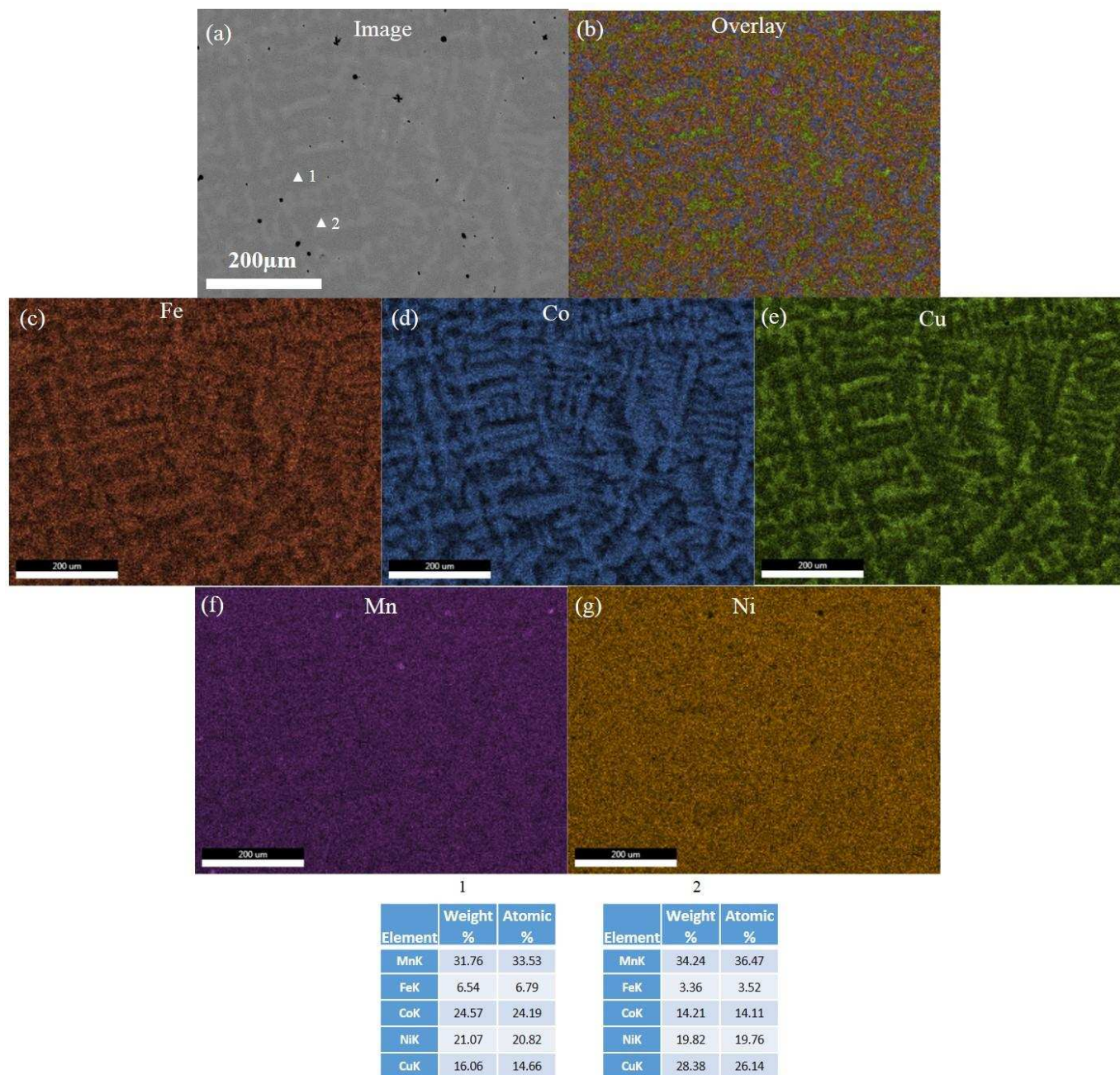


Figure 4.18 (a) BSE image and (b-g) EDS mapping of the five elements in as-cast  $\text{Fe}_5\text{Co}_{20}\text{Ni}_{20}\text{Mn}_{35}\text{Cu}_{20}$  HEA.

In order to measure the melting range of the as-cast HEA, a DTA test was carried out. Figure 4.5 shows the DTA curve of the HEA. It can be seen there are two peaks appearing on the curve, indicating the liquidus temperature at 1150 °C and solidus temperature at 1080 °C. Comparing the measured melting range (1080-1150 °C) with the melting range (1090-1148 °C) predicted by the  $\text{Fe}_x\text{Co}_{20}\text{Ni}_{20}\text{Mn}_y\text{Cu}_{20}$  ( $x+y=40$ ) phase diagram calculated in Thermo-Calc software using HEA 1.0 database, there is only a 10 °C difference for solidus temperature and 2 °C difference for liquidus temperature. It is found that the newly

proposed database, HEA 1.0 database for Thermo-Calc software, could provide a much accurate simulation result than other previous database such as Fe-base alloy (TCFE), Ni-base alloy (TCNI), Ti-base alloy (TCTI) and solid solution (SSOL) database. The HEA fabricated in this study shows a melting range lower than any literature reported HEA system. A compression test is also carried out in order to measure the mechanical properties of the as-cast HEA. A mini tensile test is first considered. However, it is difficult to machine a miniature sample. DIC was used instead of extensometer in the mini tensile test to monitor the samples strain. But the DIC has difficulty in measuring the strain once the strain becomes larger than 20%. Based on two reasons above, a compression test is hired instead of mini tensile test. Figure 4.6 and 4.7 show engineering stress-strain and true stress-strain curves of the compression test of  $\text{Fe}_5\text{Co}_{20}\text{Ni}_{120}\text{Mn}_{35}\text{Cu}_{20}$  HEA. The compression sample has a cylinder geometry with a diameter of 2mm and a height of 4mm. Compression tests are repeated two times. Reading from figure 4.6, the as-cast HEA has an average engineering yield strength of 300 MPa, engineering strength of 1210 MPa and engineering fracture strain of 52%. Reading from figure 4.7, the as-cast alloy has a true yield strength of 286MPa, true fracture strength of 591MPa and true fracture strain of 106%. Inconel 600 alloy has a true yield strength of 263MPa, true ultimate tensile strength of 952MPa and true elongation of 30%. Although the mechanical data of Inconel 600 and HEA are from different tests (Inconel 600's data is from tensile test and HEA's data is from compression test), the true stress-stain data in the elastic zone could still provide an accurate comparison. It is seen that the true yield strength of HEA (286MPa) from compression test is comparable with the true yield strength of Inconel 600 alloy (263MPa) from tensile test. According to the Vickers hardness test result, the average hardness of the as-cast HEA is 200 HV and the average hardness of as-received Inconel 600 alloy is 180 HV. The HEA shows a narrow melting range, a liquids temperature 204 °C lower than the solidus temperature of Inconel 600, a comparable hardness, strength with Inconel 600, a combination of high strength and good ductility. All of these properties make it a good candidate as the filler metal for brazing of Ni-base superalloys.

In a word, the above characterization results indicate that a FCC HEA filler metal having a liquidus temperature 200 °C than the solidus temperature Inconel 600 alloy and similar mechanical properties with Inconel 600 alloy is successfully fabricated. All the requirements proposed in section 5.1 have been satisfied. The fabricated  $\text{Fe}_5\text{Co}_{20}\text{Ni}_{120}\text{Mn}_{35}\text{Cu}_{20}$  can be used as filler foils for brazing of Ni-base superalloys.

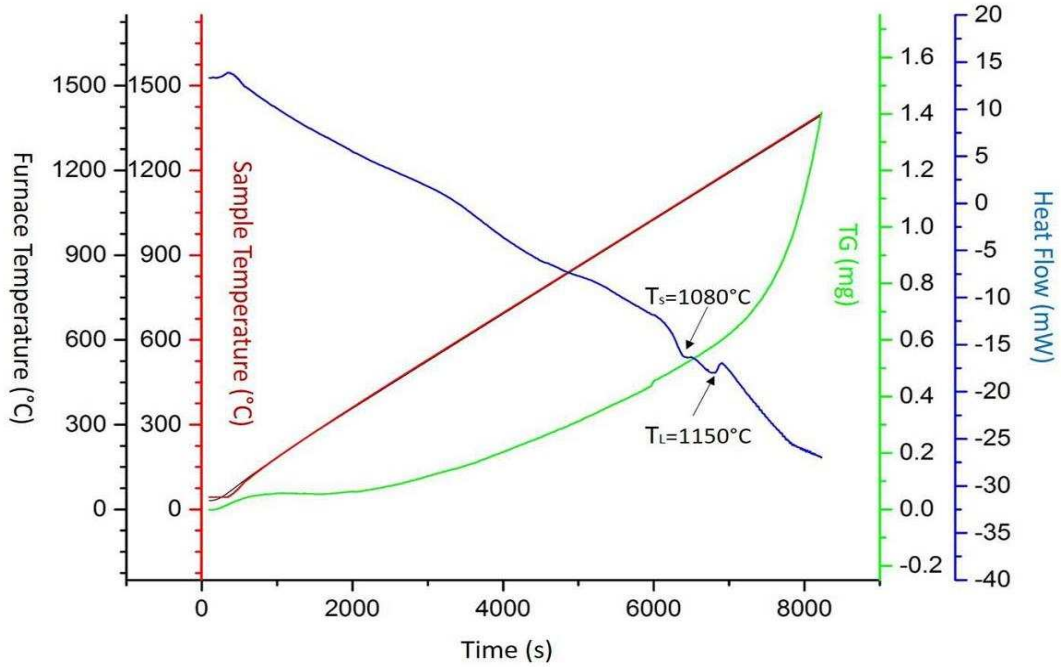


Figure 4.19 DTA curve of as-cast Fe<sub>5</sub>Co<sub>20</sub>Ni<sub>20</sub>Mn<sub>35</sub>Cu<sub>20</sub> HEA (the sample is heated in argon gas atmosphere at a rate of 15 °C/min)

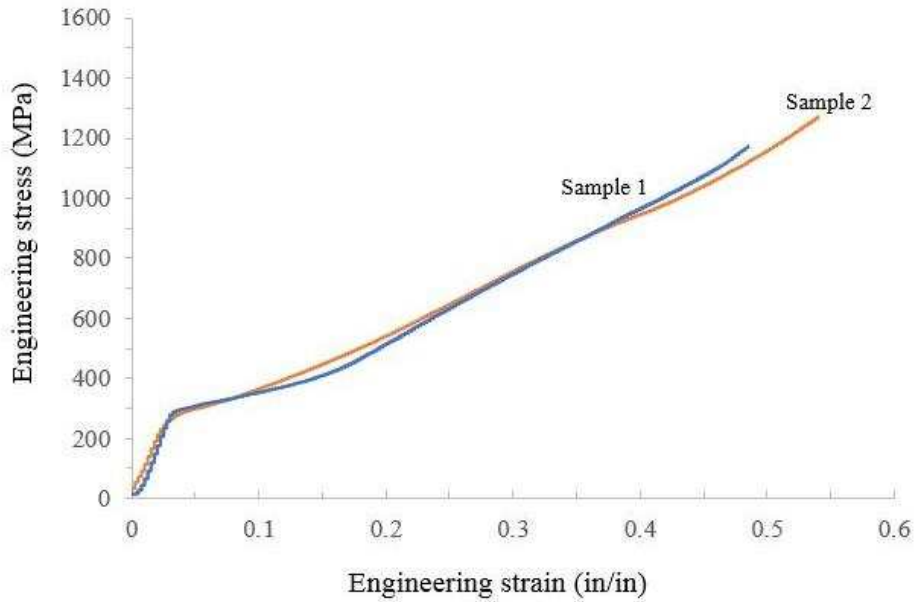


Figure 4.20 Engineering stress-strain curves during compression tests of as-cast Fe<sub>5</sub>Co<sub>20</sub>Ni<sub>20</sub>Mn<sub>35</sub>Cu<sub>20</sub> HEA (geometry:  $\phi 2 \times 4$  mm) in a strain rate of  $4 \times 10^{-4}$  /s on Alliance Machine

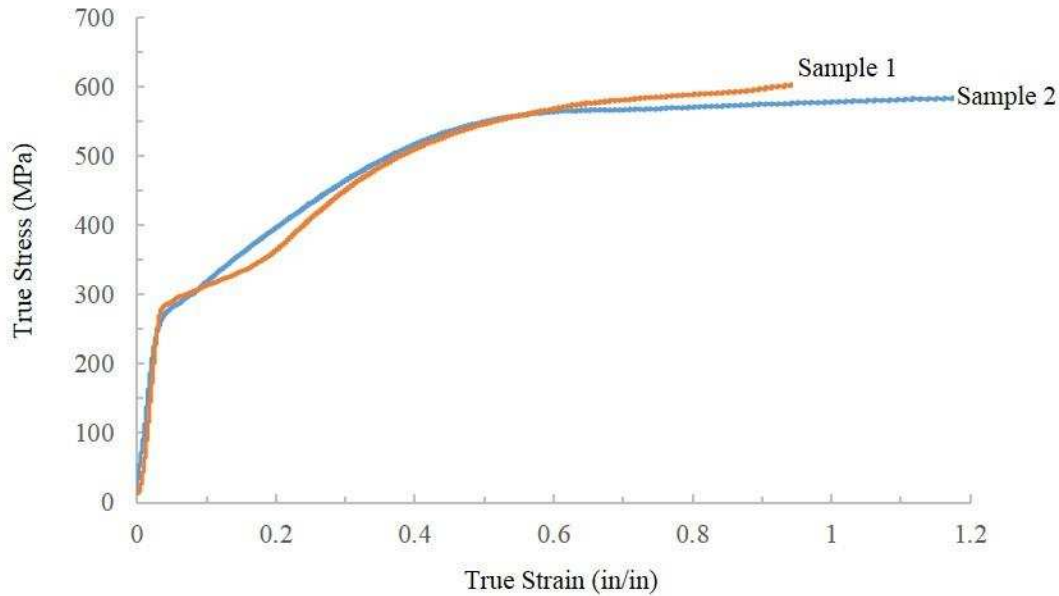


Figure 4.21 True stress-strain curves during compression tests of as-cast  $\text{Fe}_5\text{Co}_{20}\text{Ni}_{20}\text{Mn}_{35}\text{Cu}_{20}$  HEA (geometry:  $\phi 2 \times 4 \text{ mm}$ ) in a strain rate of  $4 \times 10^{-4} / \text{s}$  on Alliance Machine

### 4.3 Wetting angle test between Inconel 600 and HEA

In order to further evaluate the potential of HEA to be used as the filler metal for brazing of Inconel 600 Ni-base superalloy, several wetting angle tests are carried out at different temperatures (1160 °C, 1180 °C, 1200 °C and 1250 °C) in the vacuum furnace. The liquidus line of HEA is 1150°C and the solidus line of Inconel 600 is 1354°C. Considering the fact that the brazing temperature should be higher than liquidus line of filler metal and at least 100°C lower than the solidus line of Inconel 600, the wetting angle tests were carried out with in the range of 1160°C-1250°C in order to determine the brazing temperature. Effect of temperature on the wetting behavior of HEA on Inconel 600 substrate are investigated to choose the optimized temperature for brazing of Inconel 600 alloy. Figure 4.8 shows the spreading morphologies of the wetting angle testes at different temperatures. First, it is interesting to note that the grains of Inconel 600 alloy can be seen by eyes even without etching the sample. The grains have coarsened to several hundred micrometers while kept at high temperature. Even the lowest temperature for wetting angle tests, 1160 °C has way more exceeded the recrystallization temperature of Inconel 600 alloy. Secondly, by observing the pictures in Figure 4.8, it seems in the 1160 °C and 1180 °C samples, the HEA piece is only partly melted and not uniformly spreading on the surface of Inconel 600 substrate. The original outline of the HEA piece still can be tracked after wetting angle test. The incomplete melting or non-uniform spreading of filler metal on the substrate will cause problems. The diffusion of the elements into base metal and the fluidity of the melted filler metal will be reduced. Both of them are harmful to the bonding between

filler metal and base metal. As for 1250 °C sample, it can be seen that although the HEA has been completely melted, it has over spread on the Inconel 600 substrate. Over spreading is also harmful to brazing test because it will lead the melted filler metal flows out of the brazing area, weakening the contacting and bonding between filler metal and base metal. So 1160 °C, 1180 °C and 1200 °C are all not ideal temperature for brazing tests. Only the 1200 °C sample shows a good wetting between HEA and Inconel 600 alloy substrate. The HEA has been completely melted and it's uniformly spreading on the substrate. Over spreading is not observed in 1200 °C. A small hole is found on the top surface of solidified HEA. It is a defect formed due to the low cooling rate in the vacuum furnace during the test. In order to measure the wetting angle at 1200 °C, the 1200 °C sample was cut along the cross section and observed under SEM. In Figure 4.9, HEA and Inconel 600 alloy is distinguishable and the average wetting angle is measured as 13.9° (13.2° on the left side and 14.6° on the right side). According to the observed results above, it is seen that 1200 °C is the optimized temperature for vacuum brazing of Inconel 600 alloy. Considering the HEA is un-uniformly spreading at 1160°C and 1180°C, the product of cosine contacting angle and melted area is introduced in order to evaluate the spreading behavior of HEA on Inconel 600. It is defined as  $S.I.=A*\cos\theta$  where A is the melted area and  $\theta$  is the contacting angle. The contacting angle at 1160°C, 1180°C, 1200°C and 1250°C is 14°, 20°, 13.9° and 15°. The melted area at 1160°C, 1180°C, 1200°C and 1250°C is 48.7mm<sup>2</sup>, 42.5mm<sup>2</sup>, 59.5mm<sup>2</sup> and 164.7mm<sup>2</sup>. The value of S.I. is calculated as 47.3mm<sup>2</sup>, 39.9mm<sup>2</sup>, 57.7mm<sup>2</sup> and 158.7mm<sup>2</sup> at 1160°C, 1180°C, 1200°C and 1250°C. It can be seen that the increase of temperature promotes the spreading of HEA on Inconel 600 substrate. Moreover, the value of S.I. increases by two times when the temperature increases from 1200°C to 1250°C, which confirms the over spreading behavior of HEA on Inconel 600 substrate at 1250°C.

Besides the wetting angle, the hardness distribution in the wetting angle test sample also needs to be tested in order to check the hardness, ductility or strength difference between HEA and Inconel 600 alloy. So the cross section used for wetting angle measurement is also taken into the Vickers hardness test. Figure 4.10 shows the hardness distribution in the 1200 °C wetting angle sample. It can be seen that HEA has an average hardness of 180 HV. In the Inconel 600 area, the hardness decreases with the increase of the relative distance before the relative distance reaches 3.24mm. The minimum hardness is as low as 155 HV. The decrease of the hardness should be owed to the inter diffusion between HEA and Inconel 600 substrate. After the relative distance reaches 3.24mm, the hardness increases with the increase of the relative distance and is stabilized around 170 HV. The interface is located in the position where the relative distance is 0.84mm. The 0.84mm-3.24mm space is affected by the inter diffusion between HEA and Inconel 600 substrate, which is responsible for the lower hardness than other areas. The hardness of both HEA and Inconel 600 decreases after the wetting angle test because of the relatively lower cooling rate of brazing

process than casting process. However, they still maintain the comparable hardness. After determining 1200 °C as the brazing temperature, a series of brazing tests are carried out in the vacuum furnace using Inconel 600 as the base metal and HEA with different thickness as the filler metal.

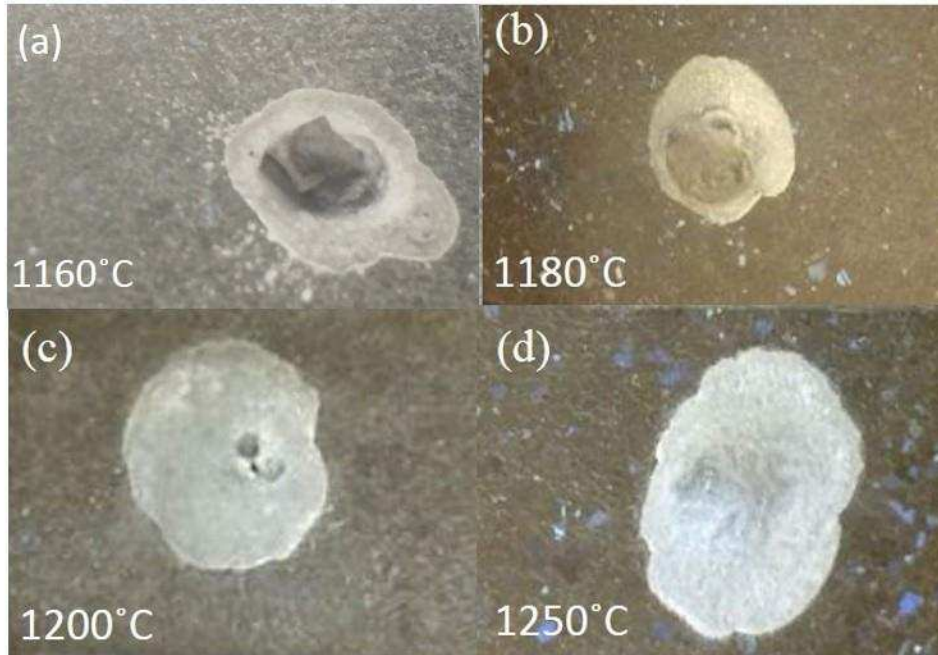


Figure 4.22 Spreading morphologies observed after wetting angle tests between  $\text{Fe}_5\text{Co}_{20}\text{Ni}_{20}\text{Mn}_{35}\text{Cu}_{20}$  HEA and Inconel 600 substrate at different temperature (a) 1160°C (b) 1180°C (c) 1200°C (d)1250°C

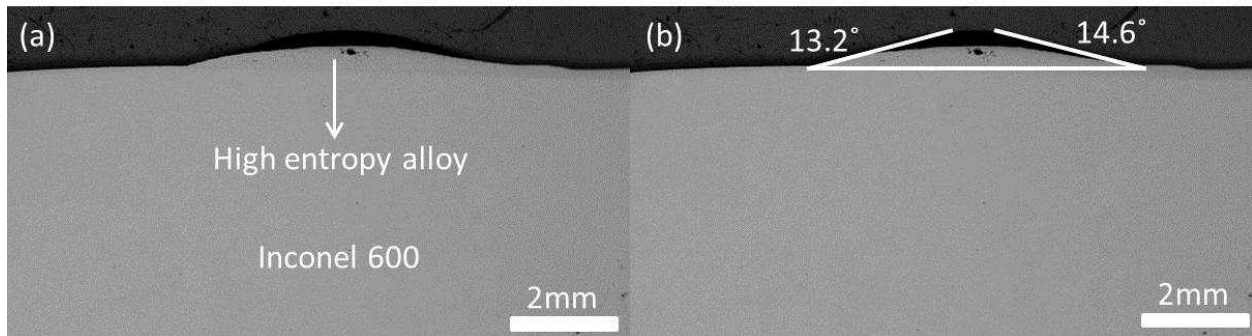


Figure 4.23 (a)Macrostructure and (b) measurement of wetting angle on both of left and right sides of 1200°C wetting angle test sample

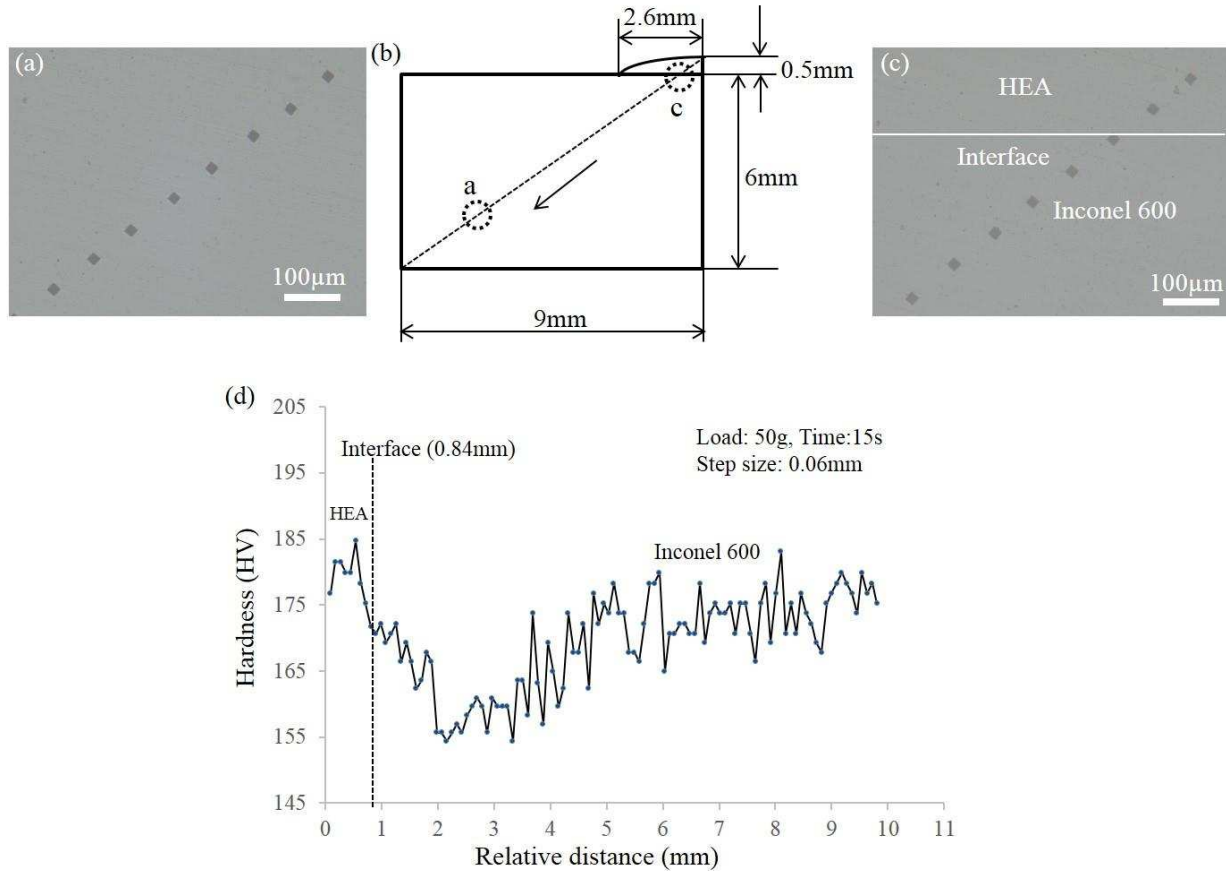


Figure 4.24 (a-c) Schematic diagram of the hardness (d) hardness distribution in different areas of the 1200°C wetting angle test sample between  $\text{Fe}_5\text{Co}_{20}\text{Ni}_{20}\text{Mn}_{35}\text{Cu}_{20}$  and Inconel 600 alloy substrate.

#### 4.4 Characterization of joints brazed by HEA filler foil

##### 4.4.1 Effect of brazing time on the shear strength of the brazed joint

Before the brazing tests, an as-cast HEA piece with a thickness of 3mm is successfully rolled into a foil with a thickness of 300  $\mu\text{m}$  for brazing tests without any cracking on the surface, confirming the good ductility of the HEA. Figure 4.11 shows the microstructure of the joints brazed at 1200 °C using HEA filler foils with a thickness of 300  $\mu\text{m}$  for different time (30, 60, 90, and 120 min). Nearly no cracking is found in the brazed joints. The width of the HEA area decreases by about 20% after brazing. Before the brazing test, the original thickness of the foils is 300  $\mu\text{m}$ . It reduces to 220  $\mu\text{m}$  after brazing, showing a reaction between HEA and Inconel 600 has happened. It is seen that the brazed joint is consisted of two areas, the coarse grain zone in the center and the diffusion affected zone with fine grains near the interface. Segregation zones are found along the grain boundaries in the coarse grain zone. The volume fraction of the segregation zone decreases with the increase of the brazing time and the composition of the brazed joint becomes more uniform. The base metal still maintains a single phase structure after brazing and the grain

size of the base metal increases with the increase of the brazing time. 1200 °C is higher than the recrystallization temperature of the base metal (Inconel 600) so grains of Inconel 600 coarsens with the increase of the holding time. Some annealing twins are also observed. It is because the Inconel 600 alloy used in this study was produced by cold rolling. Figure 4.12 shows the EDS mapping results of the joints brazed by HEA filler foil with a thickness of 300 μm for different time. Connecting the EDS mapping results to microstructure images, it is seen that the segregation zones along the coarse grain boundaries are Cu-Mn rich phases while the segregation zones inside the coarse grains are Cr-Mn rich phase. Cu-Mn rich phase is observed in every brazed joint while Cr-Mn rich phase is only found in the 120 min brazed joint. Both of the coarse grains and fine grains (in diffusion affected zone) are rich in Fe, Co and Ni, lacking Cu, Mn and Cr. The appearance of Cu-Mn rich phases along the grain boundaries can be explained by the difference of melting points of elements. Fe, Co and Ni have relatively melting points than Cu and Mn. So during the solidification of arc melting process, Fe, Co and Ni are solidified first while Cu and Mn are solidified at last. Cu and Mn are ejected to the boundary areas during the solidification of coarse grains, which are rich in Fe, Co and Ni. In as-cast HEA, segregation of Fe, Co and Cu is observed while Ni and Mn are nearly distributed uniformly in the grains and along the grain boundaries. Both of the segregation behaviors can be owned to the difference of the melting points of the elements Fe, Co, Ni, Cu, and Mn. However, the segregation behavior is more intense in the brazed joint than as-cast HEA. This is because of the arc melting process and vacuum brazing process have different cooling rate. After arc melting, the HEA button is solidified on a copper hearth cooled by anti-freezer. But the brazed sample is cooled with the furnace during the vacuum brazing process. Arc melting process has a faster cooling rate than vacuum brazing process. So only the elements having the highest melting points (Fe and Co) and lowest melting points (Cu) shows obvious segregation behavior in the as-cast HEA while all the elements show obvious segregation in the brazed joints. Figure 4.13 shows the line scanning results of the joints brazed by HEA filler foil with a thickness of 300 μm for different time. It is difficult to distinguish the brazed joint and base metal in the line scanning images even under BES mode on SEM, which confirms that a good bonding is achieved. It can be seen that Co, Cu and Mn have diffused into base metal from the filler metal while Ni and Cr have diffused into filler metal from the base metal during brazing. Fe shows no obvious diffusion behavior because of its similar concentration in as-cast HEA and as-received base metal, Inconel 600 alloy. Among Co, Cu and Mn, it can be measured from the line scanning results that Mn has the farthest diffusion distance while Co has the shortest diffusion distance. This is in agreement with the order of diffusion coefficient of Co, Cu and Mn in Ni-base superalloys reported by the literature. Fu et al. investigated the diffusion behavior of the typical alloying elements in Ni-base superalloy using the first principle calculation method. Co, Mn and Mn are assumed to have the same  $D_0$  and the calculation result shows that Mn has the lowest diffusion activation energy while Co has the highest activation energy. The inter diffusion behavior

between base metal and filler metal is promoted by the prolongation of holding time during brazing, making the composition of brazed joint more uniform and the volume fraction of Cu-Mn rich phase smaller. More Cu and Mn diffused into base metal from HEA filler metal so less Cu-Mn rich phase forms in the brazed joint. On the other hand, more Cr diffused into the filler metal from base metal with the prolongation of the brazing time. So the Cr-Mn rich phase is only found in the long holding time (120 min) brazed joint. The diffusion distances of Mn for different brazing time are measured as 13.8 $\mu\text{m}$ , 38 $\mu\text{m}$  and 52.9 $\mu\text{m}$ . The diffusion distance of Co and Cu are difficult to be measured from the line scanning results because of the low value. It also can be compared that the diffusion distance of Cr and Ni is much longer than the diffusion distance of Co, Cu and Mn in the Inconel 600 Ni-base superalloy. The diffusion of Cr and Ni in filler metal is the diffusion in melt while the diffusion of Co, Cu and Mn in base metal is the diffusion in solid. So the diffusion of Cr and Ni in filler metal is much faster than the diffusion of Co, Cu and Mn in the base metal.

The mechanism of formation of fine grains in the diffusion affected zone needs to be explored further. One possible reason is the fine grain is from epitaxial growth of filler metal near the interface. Just like the epitaxial growth in the fusion welding case, the barrier energy  $\Delta G$  for the crystal to nucleate on the substrate is

$$\Delta G = \frac{4\pi T_m^2 \gamma_{LC}^3}{3(\Delta H_m \Delta T)^2} (2 - 3\cos\theta + \cos\theta^3) \quad \text{Equation 8}$$

Here  $T_m$  is the equilibrium melting temperature,  $\Delta H_m$  is the latent heat of melting,  $\Delta T$  is the undercooling below  $T_m$ ,  $\gamma_{LC}$  is the liquid-crystal interface surface energy and  $\theta$  is the contacting angle between the liquid and substrate. If the welding is carried out without any filler metal, the contacting angle is zero and the barrier energy is zero. The liquid nucleates by arranging atoms on the substrate grains without changing the crystallographic orientations which have already existed. All the nucleated grains grow along the same direction. This epitaxial growth behavior could also appear when the liquid has a good wetting on the base metal substrate and the weld metal has the same structure with the base metal. In our study, it has been measured that the HEA has a good wetting on Inconel 600 substrate. The contacting angle is around 13.9°. Also both of Inconel 600 and HEA have a FCC structure. So epitaxial growth of HEA grains on Inconel 600 substrate is also likely to happen, resulting in the formation of fine grains in the diffusion affected zone. The growth direction is parallel to the brazed joint. However, in the center area, the grains are nucleated and grow along the direction perpendicular to the brazed joint. The coarse grain zone and diffusion affected zone form under different grain growth direction. This needs to be confirmed by the EBSD test under FSEM in the future. Another possibility is the fine grain is from the recrystallization of deformed grains on the surface of Inconel 600 alloy. Because Inconel 600 piece is cut by silicon carbide blade before brazing test,

cold deformation is accumulated in the grains on the surface. During the brazing test, the deformed grains were then annealed and recrystallized, lead to the formation of fine grains in the diffusion affected zone.

As is discussed, Cr and Ni diffuse into filler metal from base metal while Cu, Co and Mn diffuse into base metal from filler metal. Cr-Mn has a melting point higher than 1200°C so it has already precipitated in the liquid before cooling. As is shown in figure 4.1 and 4.14-16 calculated by Thermo-Calc, the decrease of the concentration of Cu, Co, Mn in the filler metal could increase the melting point of filler metal and the increase of the concentration of Ni in the filler metal could slightly decrease the melting point of filler metal. It suggests that with the inter diffusion between base metal and filler metal, the melting point of the filler metal should increase. By doing the spotting test on the joint brazed by 300µm foil for 90min, the coarse region has a composition of Cr:4.25 at%, Mn:19.40 at%, Fe:8.73 at%, Co:21.83 at%, Ni:34.40 at%, Cu: 11.39 at% while the diffusion affected zone has a composition of Cr:10.95 at%, Mn:14.62 at%, Fe:8.48 at%, Co:6.41 at%, Ni:54.89 at%, Cu: 4.65 at%. The coarse region has a melting range of 1247°C-1307°C predicted by Thermo-Calc using HEA 1.0 database while the melting point of Cu-Mn segregation region is only 873°C. As the filler metal solidifies gradually, the low melting point elements, Cu and Mn, tends to remain in the liquid and eventually segregate into the coarse grain boundaries, as indicated in Figures 4.12 and 4.13.

Figure 4.17 shows the shear strengths of the joints brazed at 1200 °C by the HEA filler foil with a thickness of 300 µm for different time (15, 30, 45, 60, 90 and 120 min). The shear strength of the brazed joint increases with the increase of brazing time before the brazing time reaches 90 min. It can be explained the relationship between the bonding force and brazing time. With the increase of the brazing time, further diffusion distance is achieved, leading to a better bonding between the base metal and filler metal. So the shear strength increases with the increase of brazing time. It is also in agreement with the relationship between shear strength and brazing time in the literature. The maximum shear strength, 530 MPa is achieved at 90 min. After that, the shear strength drops to 384 MPa when the brazing time increases from 90 min to 120 min. So when the foil thickness is fixed at 300 µm, 90 min is chosen as the optimized brazing time because a maximum shear strength of 530 MPa is achieved at 90 min. However, more efforts are still needed in order to explain the reason why the shear strength drops from 530 MPa to 384 MPa when the brazing time increases from 90 min to 120 min. It is likely because of the appearance of Cr-Mn rich phases in the brazed joint, which is not observed in other brazed joints. Cr-Mn rich phase is a brittle inter-metallic compound which is detrimental to the mechanical properties of the brazed joints. This can be confirmed on the Cr-Mn and Cu-Mn phase diagrams. Seen from the phase diagrams, Cr and Mn tend to form an intermetallic compound while Cu and Mn tend to form a FCC solid solution. So Cu-Mn rich phases is not harmful to the mechanical properties of the brazed joints because of its similarity with FCC HEA while Cr-

Mn intermetallic compound is detrimental to the mechanical properties of brazed joints because of its low ductility. Till now, only very limited literature on brazing of Inconel 600 alloy has been published. The shear strength of the brazed joint can only be found in one paper, which uses 50  $\mu\text{m}$  Cusil ABA filler foils to braze Inconel 600 alloy. The maximum reported shear strength is 325 MPa. The optimized shear strength achieved in this study is 68% higher than the literature reported shear strength. The filler metal designed in this study successfully avoids the formation of detrimental brittle phase in the brazed joint while achieving an optimized shear strength 68% higher than literature results.

Figure 4.18-4.20 show the hardness distribution of joints brazed at 1200  $^{\circ}\text{C}$  by HEA filler foil with a thickness of 300  $\mu\text{m}$  for different time (30, 90, and 120 min). The brazed joints have an average hardness of 200 HV while the base metal Inconel 600 alloy shows an average hardness of 165 MPa. Although the brazed joints show a higher hardness than base metal, they're still comparable, which is good for the mechanical properties of the brazing repaired Ni-base superalloy made components. The detail hardness distribution of different areas, phases (coarse grain zone, diffusion affected zone, segregation zone) in the brazed joints are also marked in Figure 4.18-4.20. The fine grains in diffusion affected zone have the highest average hardness of 215 HV while the coarse grains have the lowest average hardness of 185 HV. The average hardness of Cu-Mn segregation zone is around 200 HV. In addition, in the 120 min brazed joint, the hardness of Cr-Mn rich phase is also measured. The Cr-Mn rich phase has an average of 240 HV, showing the highest hardness among all the phases. The difference of the hardness of Cu-Mn rich phase and Cr-Mn rich phase can be explained by Cu-Mn and Cr-Mn phase diagrams shown in Figure 4.22 and 4.23. The compositions of Cu-Mn and Cr-Mn rich phases are also marked on the phase diagrams. It can be seen from Cu-Mn phase diagram that a single phase infinite solid solution could form above 600  $^{\circ}\text{C}$ . Because of the fast cooling rate after brazing, the solid solution phase structure may still be maintained at room temperature. Considering it is an infinite solid solution and both Cu has a FCC phase structure, Cu-Mn solid solution should have a FCC phase structure, the same with HEA. So it shows a comparable hardness with HEA and it is not harmful to the mechanical properties of the brazed joint. However, in the Cr-Mn phase diagram, at high temperature, Cr-Mn would form an intermetallic compound instead of forming a solid solution like Cu-Mn system. So Cr-Mn compound is more brittle than HEA and its appearance is detrimental to the mechanical properties of the brazed joints. It is interesting to note that the Cr and Mn are closet neighbors on the periodical table of the elements while Cu and Mn are not. The atomic radius of Cr and Cu are the same, 128pm, very close to the atomic radius of Mn, 127pm. Both of Cr and Mn have a BCC phase structure while Cu has a FCC phase structure. The electronegativity of Cr is 1.7, closer to the electronegativity of Mn (1.5) than Cu (1.9). Considering the factors including atomic size, electronegativity and crystal structure, according to the Hume-Rothery principle, Cr should have more

advantages than Cu to form an infinite solid solution with Cu. However, the phase diagram shows at high temperature, Cu could form an infinite solid solution with Mn while Cr could not, which is opposite to the prediction by Hume-Rothery. Equation 9 shows the how to calculate the ionic bond percent in an A-B system where  $\chi_A$  and  $\chi_B$  represent the electronegativity of element A and B. According to Equation 9, the ionic bond percent is only 1% for Cr-Mn phase and 4% for Cu-Mn phase, which means the covalent bond for Cr-Mn phase and Cu-Mn phase are 99% and 96%. Judging from the covalent bond percent, Cr-Mn and Cu-Mn phases should have high hardness and high strength because the covalent bond usually has high covalent bonding energy. However, the hardness result shows a totally opposite tendency. Both Cr-Mn and Cu-Mn phases have a low hardness, comparable with typical FCC metals, which also needs to be investigated more deeply.

$$Ionic\ Character\% = (1 - e^{-0.25(\chi_A - \chi_B)^2}) * 100\% \quad \text{Equation 9}$$

It is also worth to note that in Figure 4.21, by connecting the hardness profile with EDS line scanning results, actually the diffusion affected zone with the highest hardness is located in the transition area between base metal and filler metal area with the most complex element distribution. It neither belongs to base metal nor filler metal.

While the optimized brazing time has been determined at 90 min for the filler foil with a thickness of 300  $\mu\text{m}$ , a series of brazing tests are also carried to join Inconel 600 alloys by HEA filler foils with a thickness of 50  $\mu\text{m}$  at 1200  $^{\circ}\text{C}$  for different time (15, 30, 45, 60, and 90 min). The shear strength of different brazed joints is also tested. The shear strength increase from 220 MPa to 310 MPa with the increase of brazing time from 15-60 min. A maximum shear strength of 310 MPa is achieved at 60 min. The shear strength nearly keeps constant when the brazing time is further increased to 90 min. With the increase of the brazing time, further diffusion distance is achieved, leading to a better bonding between the base metal and filler metal. So the shear strength increases with the increase of brazing time. On the other hand, the driving force of diffusion comes from the concentration gradient. The concentration gradient decreases with the time so the driving force decreases with time. The driving force at 90 min is already low. The diffusion behavior is nearly not promoted by prolonging the brazing time from 90 to 120 min so the shear strength also keeps constant. It is also worth to note that no Cr-Mn segregation zone is observed in all the 50  $\mu\text{m}$  brazed joints so an obvious drop of shear strength doesn't appear. 60 min is determined as the optimized brazing time when the foil thickness is fixed at 50  $\mu\text{m}$ . As is shown in Section 5.4.2, a thinner foil has a higher diffusion efficiency than a thicker foil. So 50  $\mu\text{m}$  needs shorter time than 300  $\mu\text{m}$  to reach the maximum shear strength. However, it is also necessary to note that although the reduction of the foil thickness promotes the inter diffusion between HEA and Inconel 600, Cr-Mn rich phase is not found in any 50  $\mu\text{m}$  brazed joint or there will be a reduction of shear strength when the brazing time is increased from

60 to 90 min. With the prolongation of brazing, the diffusion of Cr and Mn is promoted. More Cr diffuses into the filler metal which is good for the formation of Cr-Mn rich phase. But more Mn also diffuses into the base metal which prevents forming the Cr-Mn rich phase. They have two opposite effects on Cr-Mn rich phase formation. The mechanism needs to be studied more deeply in the future work, especially the relationship between the formation of Cr-Mn rich phase and the reduction of shear strength. Video 1 and Video 2 show the strain distribution in the 15 and 60 min brazed samples during the shear tests. The strain distributions in the joint and base metal of 60 min brazing sample are shown in Figure 4.24. Pictures were taken every second during the shear test. The shear test was done at 797s. The software has difficulty to measure the strain due to large deformation. It can be seen at the beginning of the shear tests, the strain distribution is uniform in both base metal and brazed joint. No obvious strain difference can be observed in the DIC image. However, after more loads are applied on the sample, it is seen that the brazed joint undertakes more strain and stress than Inconel 600 base metal due to HEA's higher strength and hardness than Inconel 600 alloy. At the later stages of the shear tests, the peak strain is shown at the interface between the brazed joint and base metal, which means the fracture is initiated at the interface. The reduction of the foil thickness reduces the HEA's ability to undertake plastic deformation so the shear strength of the brazed joints decreases with the decrease of the foil thickness. By comparing video 1 and video 2, in the 15 min brazed sample, the brazed joint doesn't demonstrate a uniform deformation and the crack is initiated in the base metal, Inconel 600 alloy. In the 60 min brazed sample, the brazed joint shows a uniform deformation distribution in the later period during the shear test and the crack is initiated from the interface between the brazed joint and the Inconel 600 alloy base metal. The 60 min brazed sample fails earlier than the 15 min brazed sample. The 60 min brazed joint also undertakes at least three times deformation than base metal. In the DIC tests, the software has the difficulty in measuring the strain when the strain is larger than 20%. However, the measured results have already provided enough information to distinguish the deformation of different brazed joints.

In a word, Inconel 600 alloy was successfully brazed by  $\text{Fe}_5\text{Co}_{20}\text{Ni}_{20}\text{Mn}_{35}\text{Cu}_{20}$  filler foils at 1200 °C. A maximum shear strength of 530 MPa was achieved at 90 min (brazing time) while using 300  $\mu\text{m}$  foil and a maximum shear strength of 310 MPa was achieved at 60 min (brazing time) while using 50  $\mu\text{m}$  foil. In the brazed joint, only Cu-Mn rich and Cr-Mn rich ductile phase was found. Brittle borides or silicides which are always found in the joint brazed by commercial fillers, have successfully be avoided in this study by replacing commercial fillers with HEA fillers. The mechanism of bonding is owed to the diffusion of Mn, Co, and Cu into the base metal and diffusion of Cr, Ni into the filler metal. The strain distribution among the brazed samples indicates that the brazed joint with a good ductility could deform with base metal together during the shear test. So the sample could undertake more strain, leading to a higher shear strength.

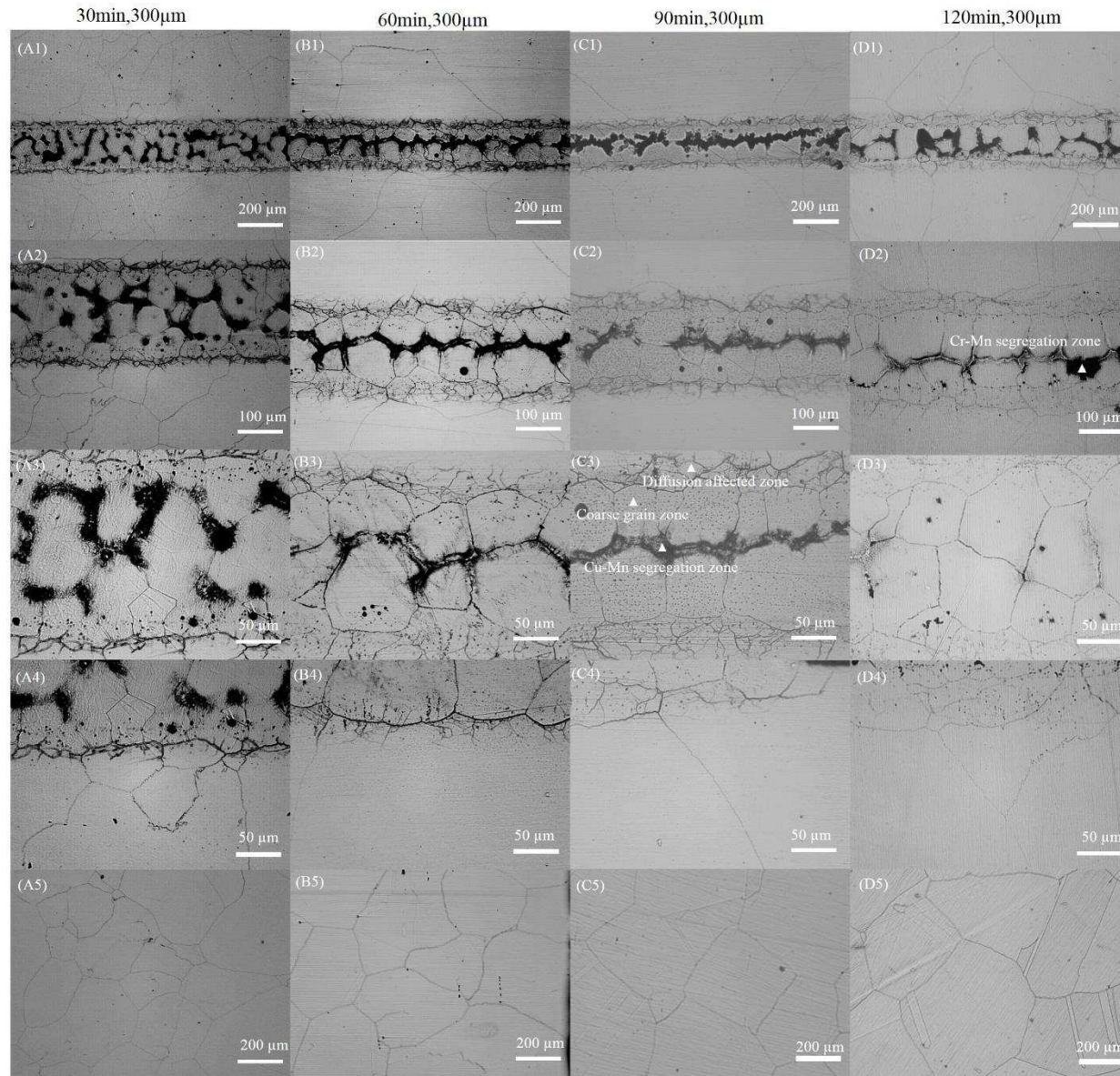


Figure 4.25 Microstructure of the joint brazed at 1200 °C for by a filler foil with a thickness of 300μm for different brazing time (A1-A5)30min, (B1-B5)60min, (C1-C5)90min, and (D1-D5)120min

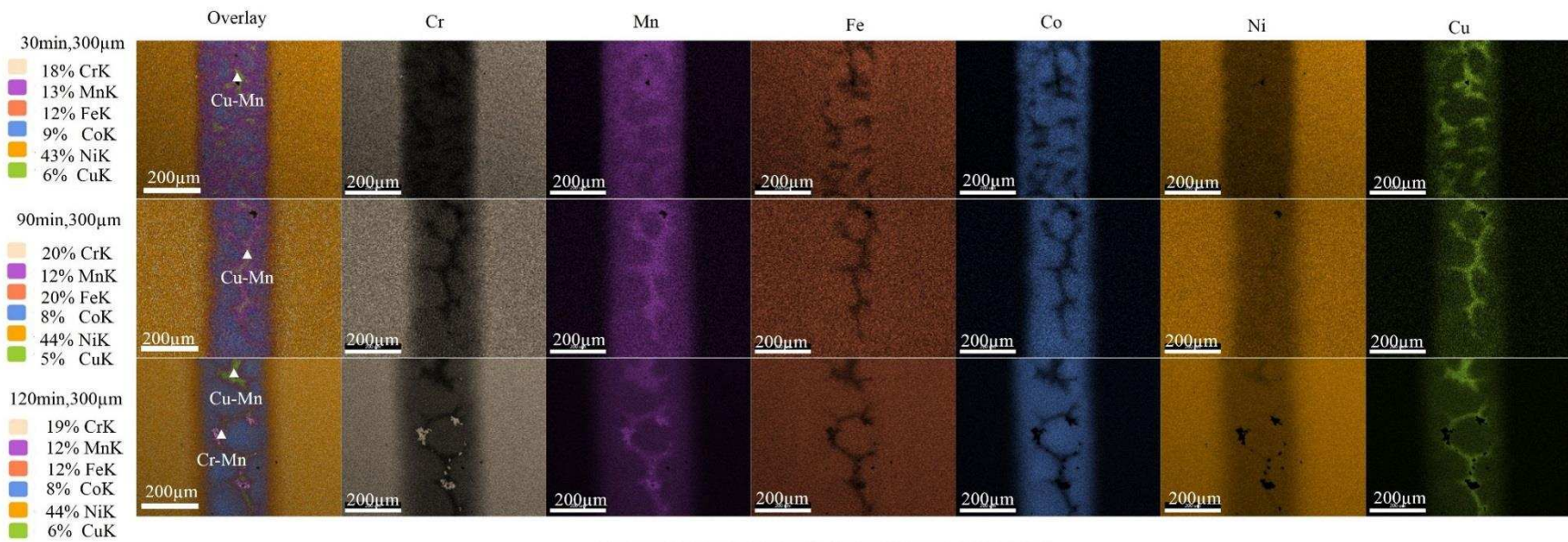


Figure 4.26 EDS Mapping of elements in joints brazed at 1200 °C for 90 min using HEA filler foil with different thicknesses (300, 200, 100, and 50 μm)

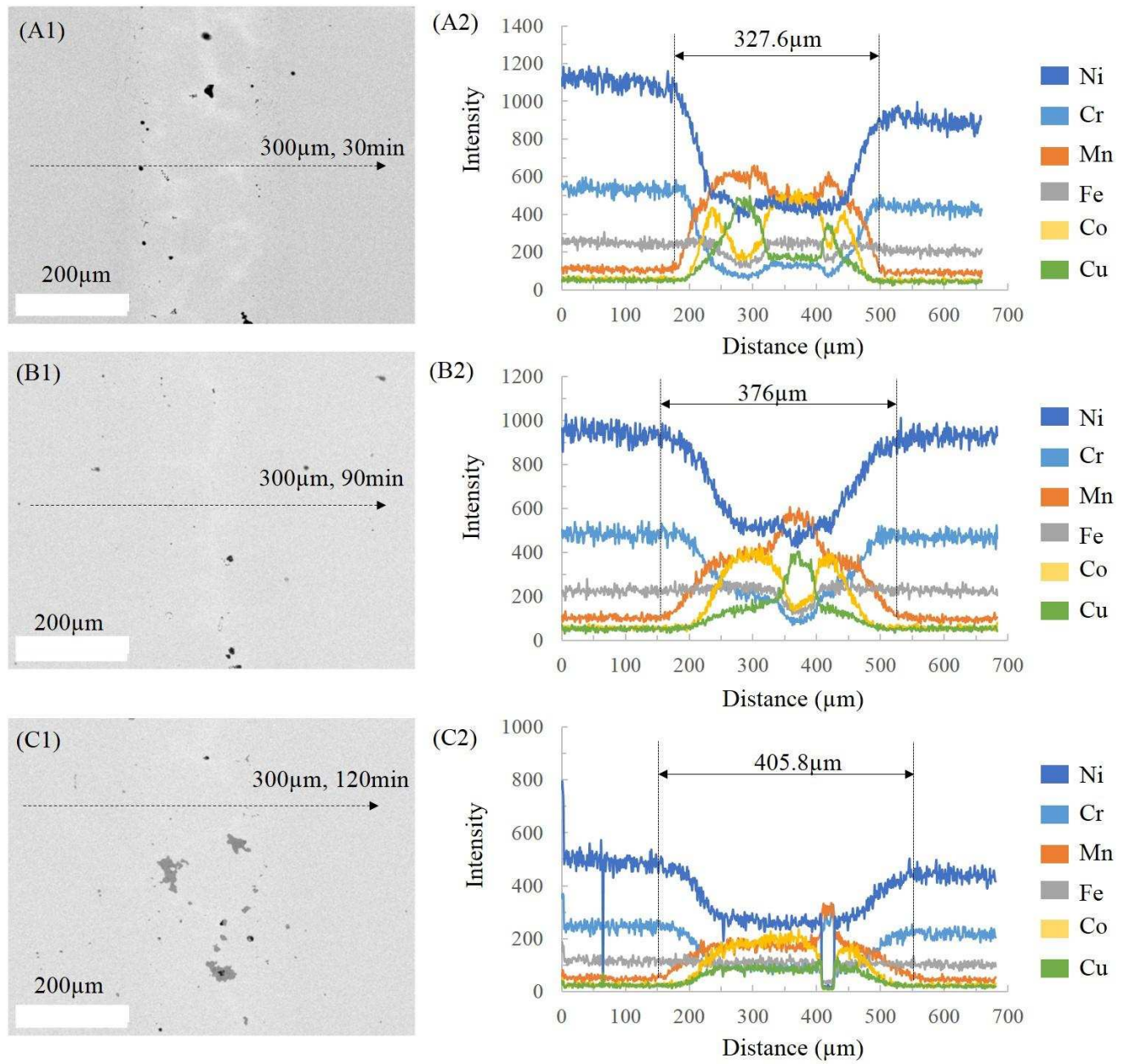


Figure 4.27 EDS line scanning of joint brazed at 1200 °C for different time (30, 90, and 120 min) using 300 μm HEA filler foils. (A1-A2) 30min (A2-B2) 90min (A3-B3) 120min

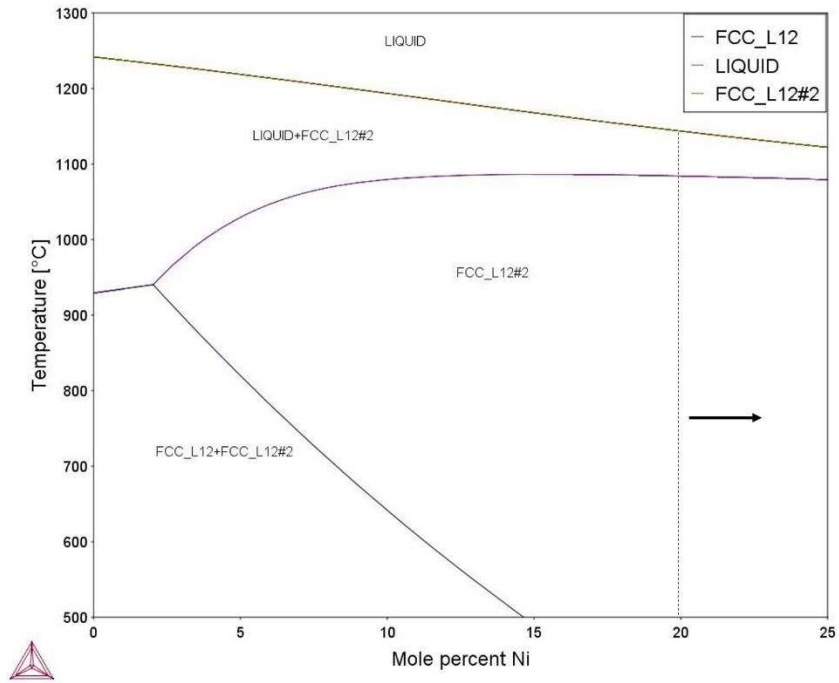


Figure 4.28 Phase diagram for  $\text{Fe}_x\text{Co}_{20}\text{Ni}_y\text{Mn}_{35}\text{Cu}_{20}$  system ( $x+y=25$ ) calculated by Thermo-Calc using HEA 1.0 database

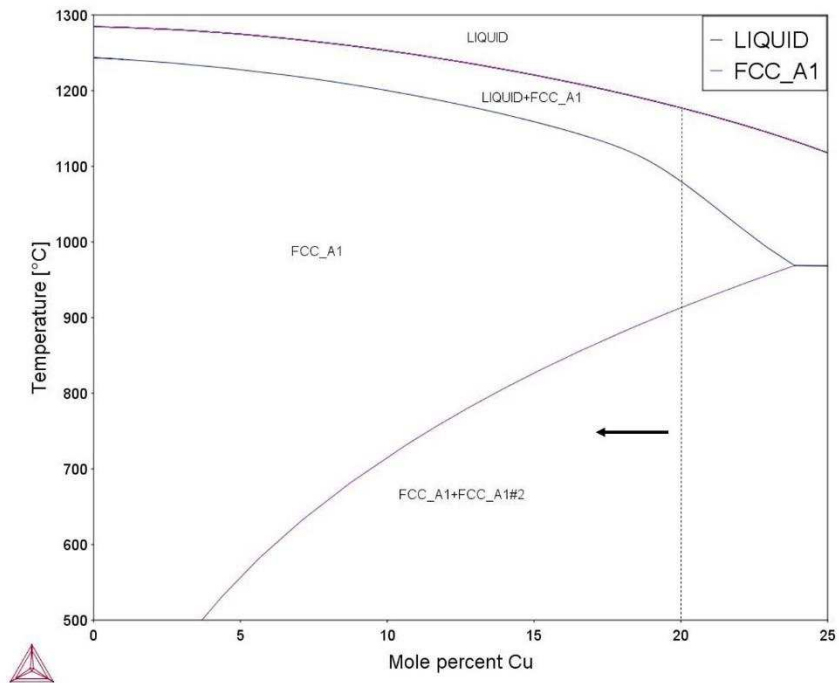


Figure 4.29 Phase diagram for  $\text{Fe}_x\text{Co}_{20}\text{Ni}_{20}\text{Mn}_{35}\text{Cu}_y$  system ( $x+y=25$ ) calculated by Thermo-Calc using HEA 1.0 database

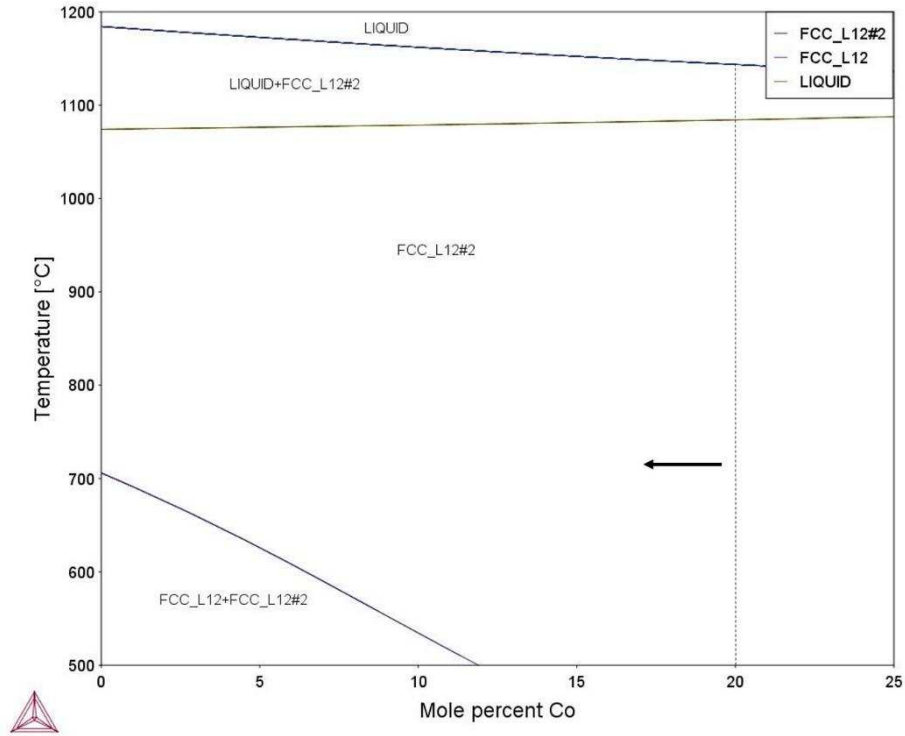


Figure 4.30 Phase diagram for  $Fe_xCo_yNi_{20}Mn_{35}Cu_{20}$  system ( $x+y=25$ ) calculated by Thermo-Calc using HEA 1.0 database

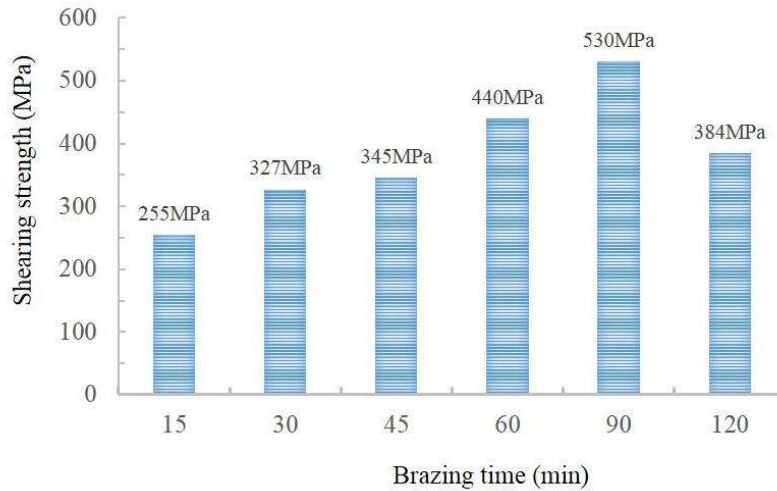


Figure 4.31 Shear strength of the Inconel 600/ $Fe_5Co_{20}Ni_{20}Mn_{35}Cu_{20}$  HEA/Inconel 600 braze joint of different brazing time (15, 30, 45, 60, 90, and 120 min, filler metal foil thickness and brazing temperature were fixed at 300  $\mu$ m and 1200  $^{\circ}$ C).

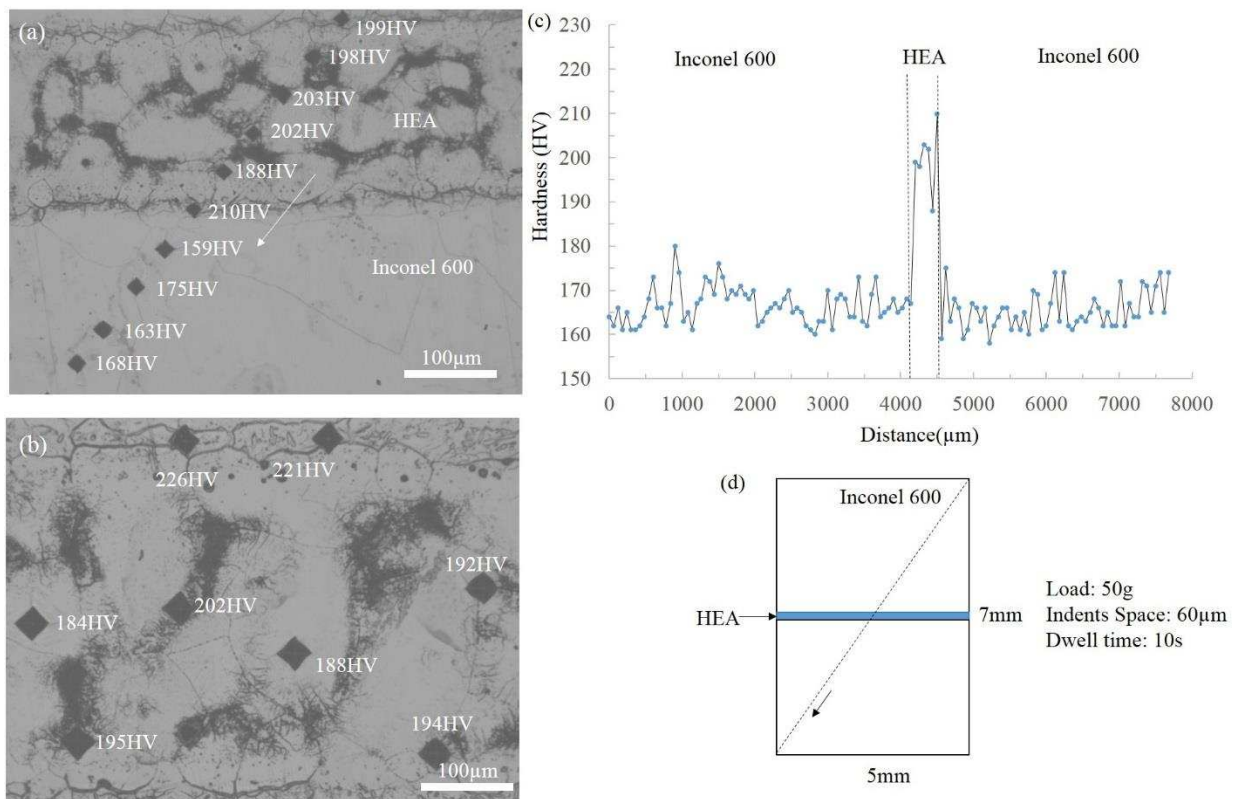


Figure 4.32 (a, b) Hardness distribution in joint brazed at 1200 °C for 30 min by  $\text{Fe}_5\text{Co}_{20}\text{Ni}_{20}\text{Mn}_{35}\text{Cu}_{20}$  filler with a thickness of 300  $\mu\text{m}$ . (c) Hardness distribution in different areas of the brazed sample (d) Schematic diagram of the hardness test

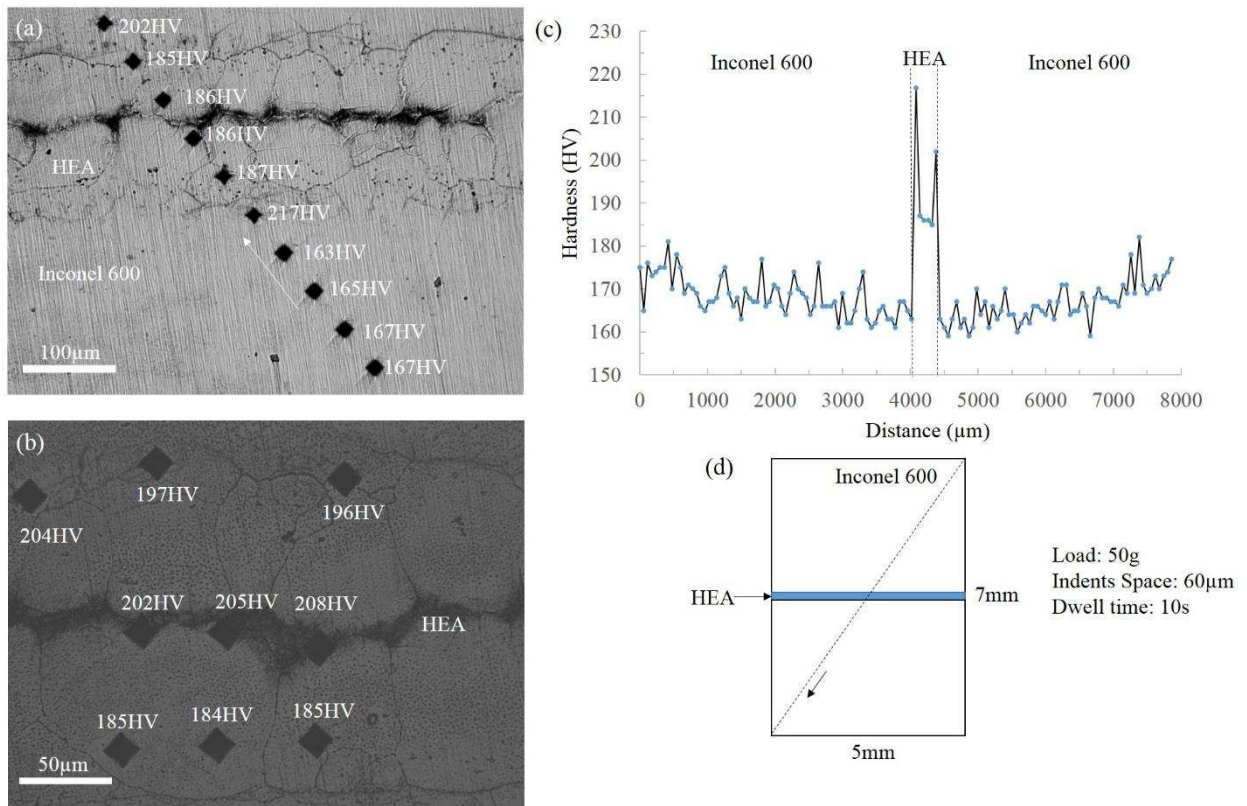


Figure 4.33 (a, b) Hardness distribution in joint brazed at 1200 °C for 90 min by  $\text{Fe}_5\text{Co}_{20}\text{Ni}_{20}\text{Mn}_{35}\text{Cu}_{20}$  filler with a thickness of 300 μm. (c) Hardness distribution in different areas of the brazed sample (d) Schematic diagram of the hardness test

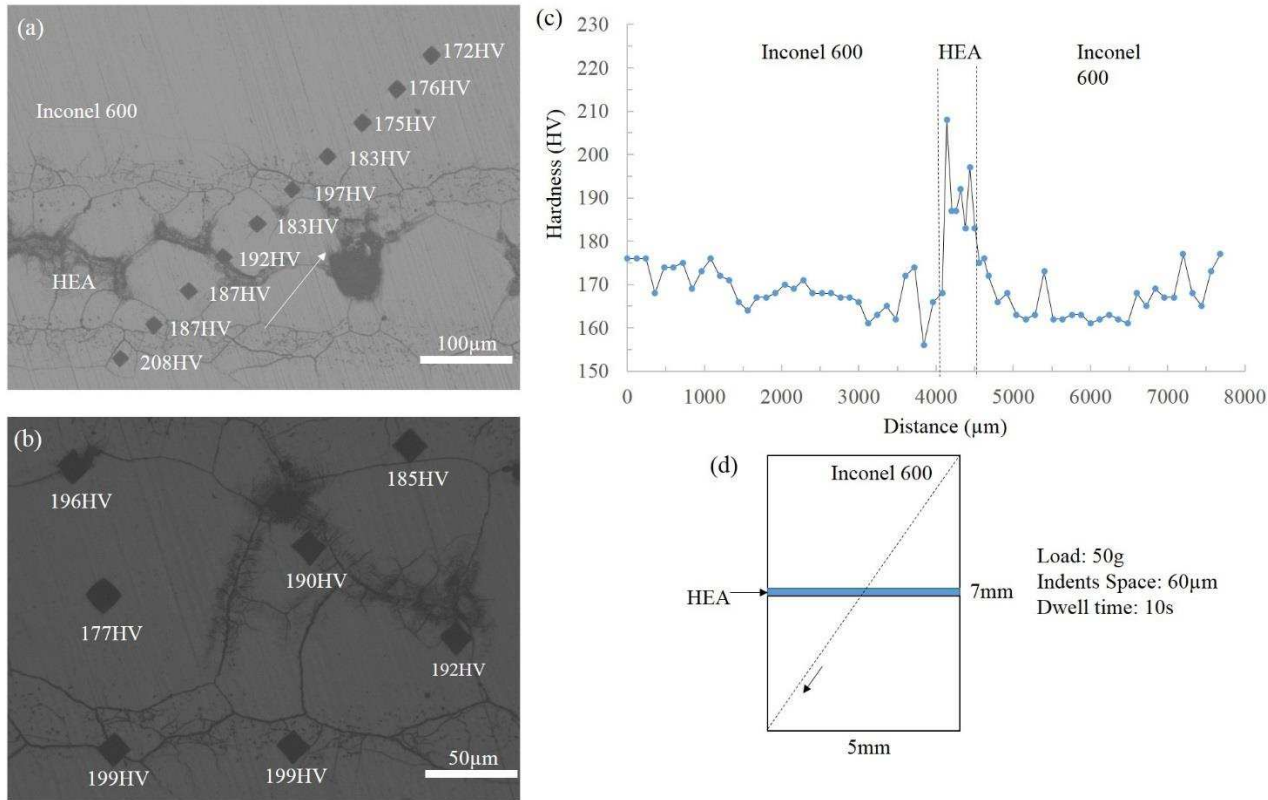


Figure 4.34 (a, b) Hardness distribution in joint brazed at 1200 °C for 120 min by  $\text{Fe}_5\text{Co}_{20}\text{Ni}_{20}\text{Mn}_{35}\text{Cu}_{20}$  filler with a thickness of 300 µm. (c) Hardness distribution in different areas of the brazed sample (d) Schematic diagram of the hardness test

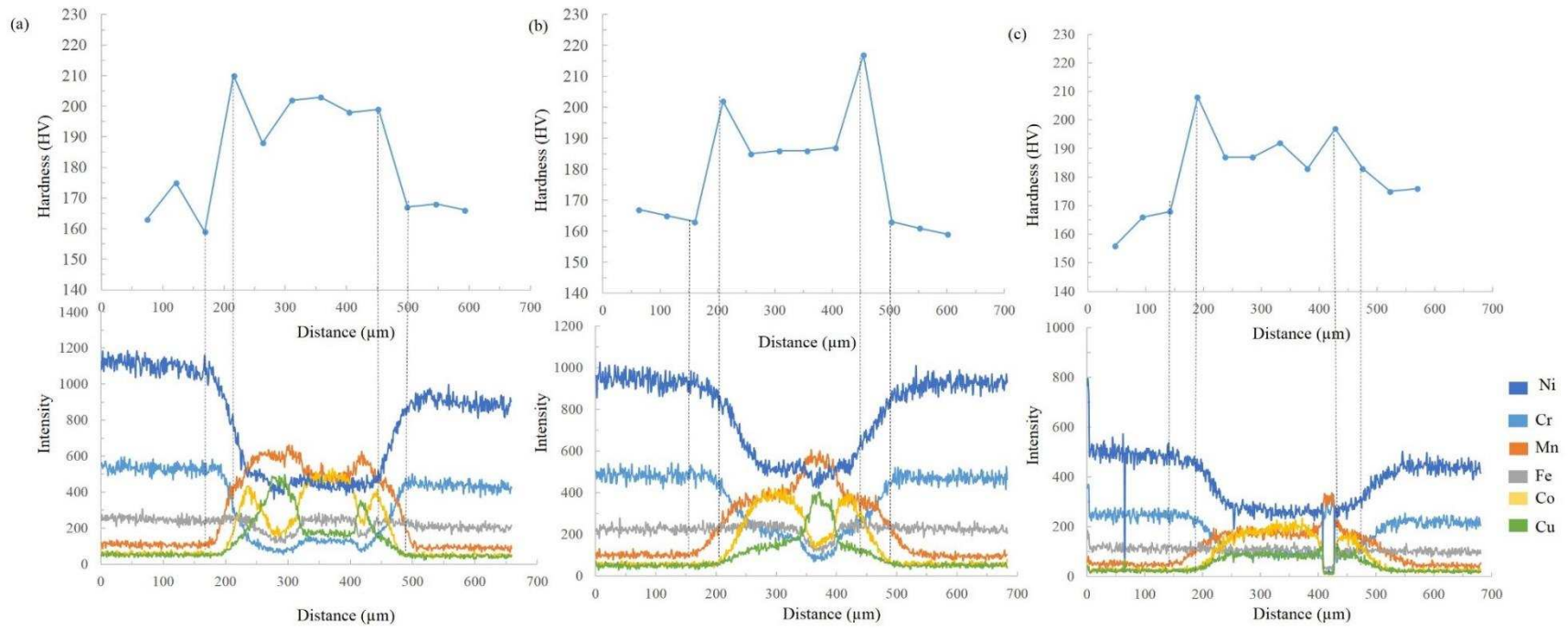


Figure 4.35 Hardness variation of the joints brazed by HEA filler foil with a thickness of 300µm for different time. (a) 30min (b)90min (c)120min

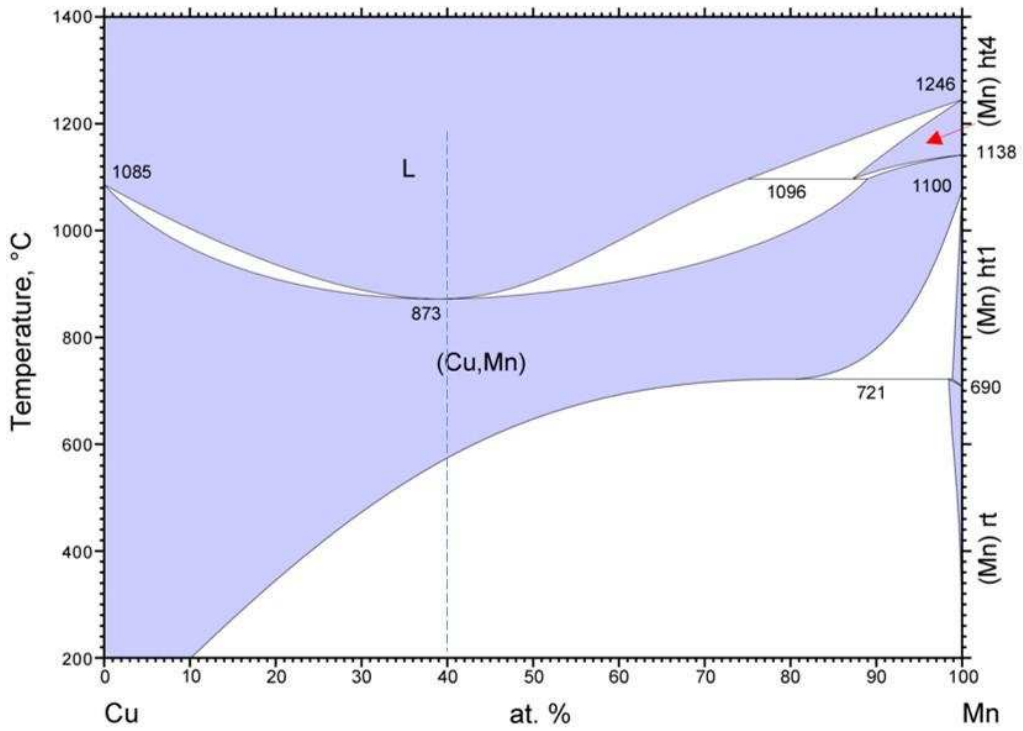


Figure 4.36 Cu-Mn phase diagram with the composition of Cr-Mn rich phase observed

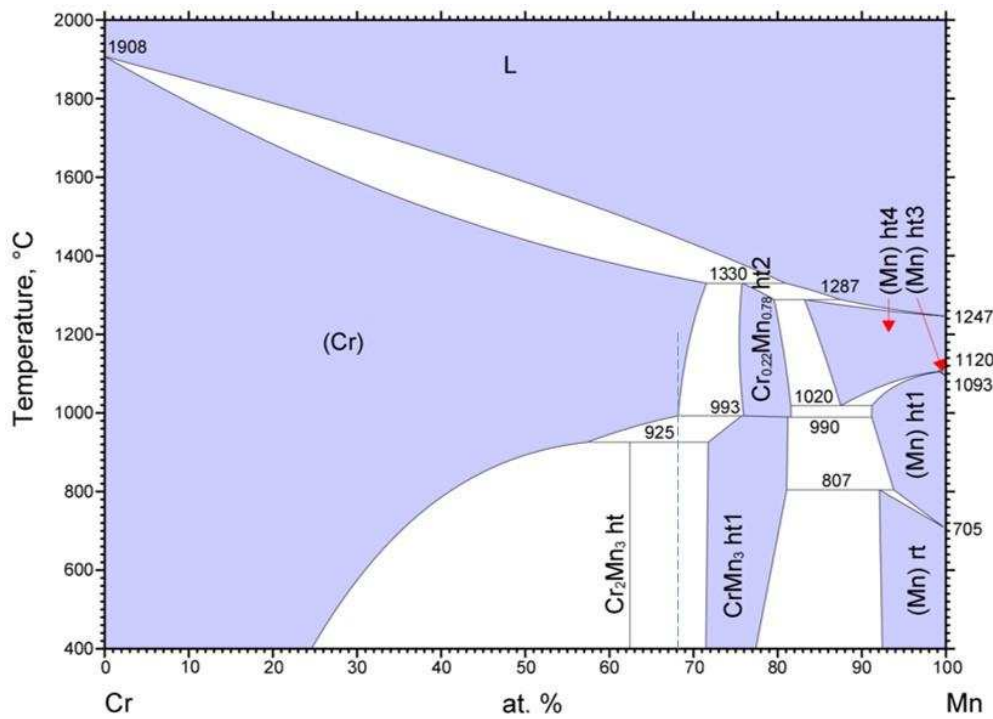


Figure 4.37 Cr-Mn phase diagram with the composition of Cr-Mn rich phase observed

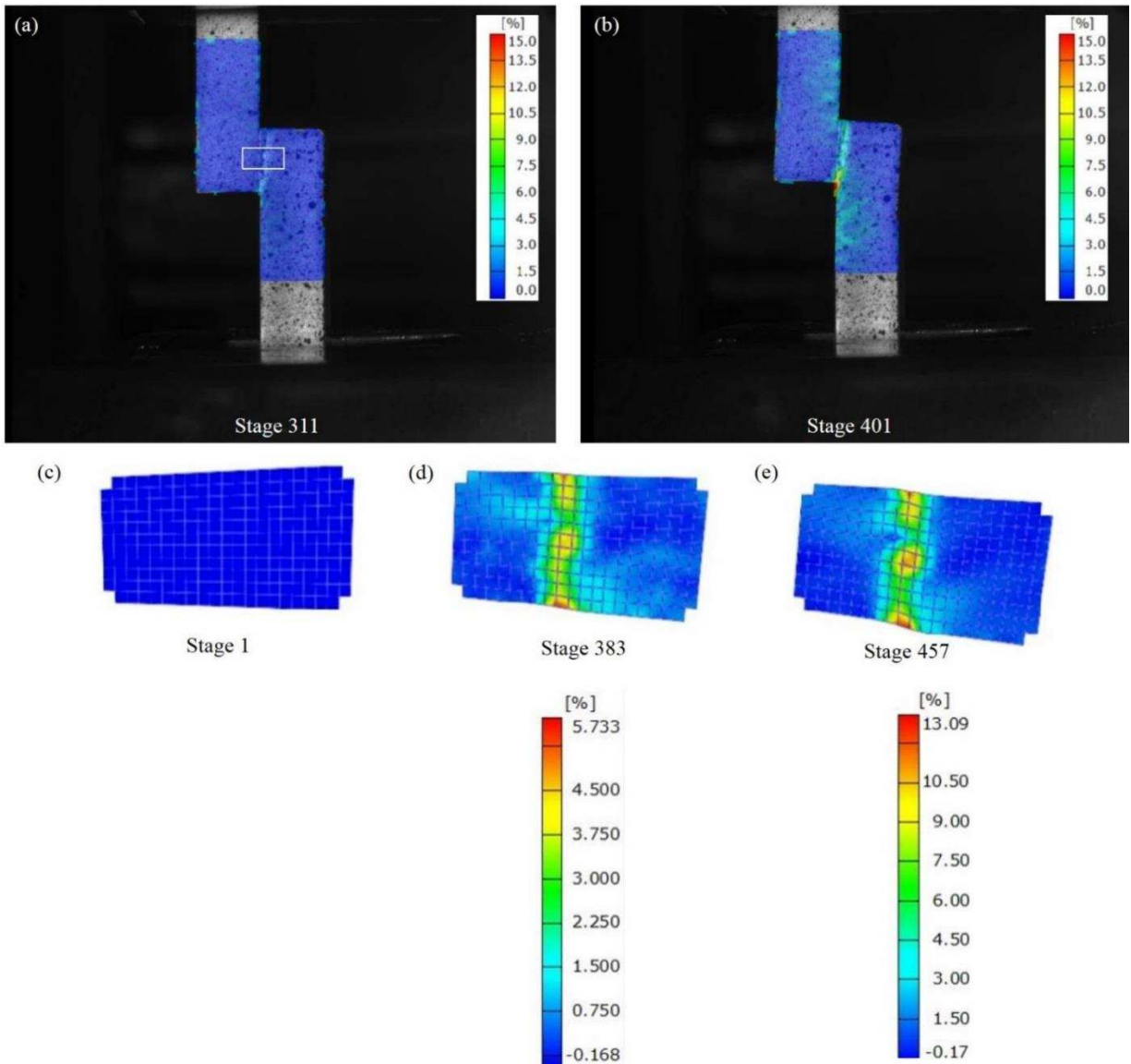


Figure 4.38 Strain distribution during shear test of the sample brazed at 1200 °C for 60 min by the HEA filler foil with a thickness of 50  $\mu\text{m}$ . (a, b) strain distribution in the whole brazed sample (c, d, e) strain distribution in the local area marked in (a).

#### 4.4.2 Effect of filler foil thickness on the shear strength of the brazed joint

In order to investigate the effect of foil thickness on the shear strength of the brazed joints, Inconel 600 alloy plates were brazed by HEA filler foil with different thickness (300, 200, 100, and 50  $\mu\text{m}$ ) at 1200  $^{\circ}\text{C}$  for 90 min. Nearly no cracking is found in the brazed joints. Figure 4.25 shows the microstructure of the joints brazed by filler foils with different thickness. The width of the brazed joint is also reduced by 20%-25%. Like the joints brazed by 300  $\mu\text{m}$  filler foil for different time in section 4.4.1, the brazed joint is consisted of three areas, coarse grain zone, segregation zone along the coarse grain boundaries, diffusion affected zone with fine grains near the interface. However, no segregation zone is found inside the coarse grains. The coarse grain shows an average size of 60  $\mu\text{m}$  while the fine grain in the diffusion affected zone shows an average size of 10  $\mu\text{m}$ . The volume fraction of the segregation zone along the boundaries decreases with the decrease of the foil thickness. The segregation zone is almost not seen in the 50  $\mu\text{m}$  brazed joint and the 50  $\mu\text{m}$  joints shows a uniform composition. This is because with the decrease of the filler foil thickness, the area of the grain boundaries is also decreased, resulting in lower volume fraction of segregation zone along the coarse grain boundaries in the brazed joints. As for the base metal, it still maintains a single phase structure. All the four samples show similar grain size because they were heated at the same temperature (1200  $^{\circ}\text{C}$ ) for the same time (90 min). All the samples show similar base metal grain size because they are heated at 1200  $^{\circ}\text{C}$  for the same time. Figure 4.26 shows the EDS mapping results of the joint brazed at 1200  $^{\circ}\text{C}$  for 90 min by HEA filler foils with different thickness (300, 200, 100 and 50  $\mu\text{m}$ ). By combining Figure 4.25 and Figure 4.26, it can be seen that the segregation zone along coarse grain boundaries are Cu-Mn rich phases. No Cr-Mn rich phase is detected in any brazed joint. Like the joints brazed by 300  $\mu\text{m}$  filler foil for different time in section 5.4.1, it also can be seen that Co, Cu and Mn diffuse into base metal from base metal and Ni, Cr diffuse into filler metal from base metal. Fe has no obvious diffusion behavior because of its similar initial concentration in both of HEA and Inconel 600 alloy. The driving force of the diffusion of elements comes from the concentration gradient on both sides. Because both sides (HEA and Inconel 600 alloy) has similar concentration of Fe, Fe is difficult to diffuse. Among Cu, Co and Mn, Mn shows the best ability to diffuse in the base metal because of its lowest diffusion activation energy. Figure 4.27 shows the line scanning results of the joints brazed at 1200  $^{\circ}\text{C}$  for 90 min by HEA filler foils with different thickness (300, 200, 100, and 50  $\mu\text{m}$ ). It is difficult to distinguish the brazed joint and base metal in the line scanning images even under BES mode on SEM, which confirms that a good bonding is achieved. The diffusion distance of each element under different conditions can be measured from the line scanning curve of different elements. However, it is difficult to get an accurate value for Co and Cu because of their low value and resolution. Only the diffusion distance of Mn can be measured accurately. The diffusion distance of Mn are measured as 38, 67.5, 93 and 109  $\mu\text{m}$  for the joints brazed by filler foil with a thickness of 300, 200, 100, and 50  $\mu\text{m}$ . A parameter, diffusion efficient is defined

in order to evaluate the diffusion behavior of Mn in base metal. The diffusion efficiency of Mn is calculated as 25.3%, 67.5%, 186% and 436% for for the joints brazed by filler foil with a thickness of 300, 200, 100, and 50  $\mu\text{m}$ . Comparing the diffusion efficiency for different foil thickness, the reduction of the foil thickness promotes the diffusion of elements during brazing. The microstructure of the brazed joints thus becomes more uniform and less composition segregation can be detected in the brazed joints. This also reduces the volume fraction of the segregation zone along the grain boundaries in the 50  $\mu\text{m}$  brazed joint except the reduction of the grain boundary area. The shear strength of the joints brazed at 1200 °C for 90 min by filler foils with different thickness are listed in Figure 4.28. The shear strength of the brazed joint decreases with the decrease of the foil thickness. Shear strength drops from 530 to 302 MPa when the foil thickness decreases from 300 to 50  $\mu\text{m}$ .

In a word, in this section, effect of the filler foil thickness on the shear strength of the brazed joints is investigated. Shear strength decreases with the decrease of the filler foil thickness because the ability of the brazed joint to undertake deformation decreases. It is also found that the inter diffusion between HEA and Inconel 600 is promoted by the reduction of filler foil thickness.

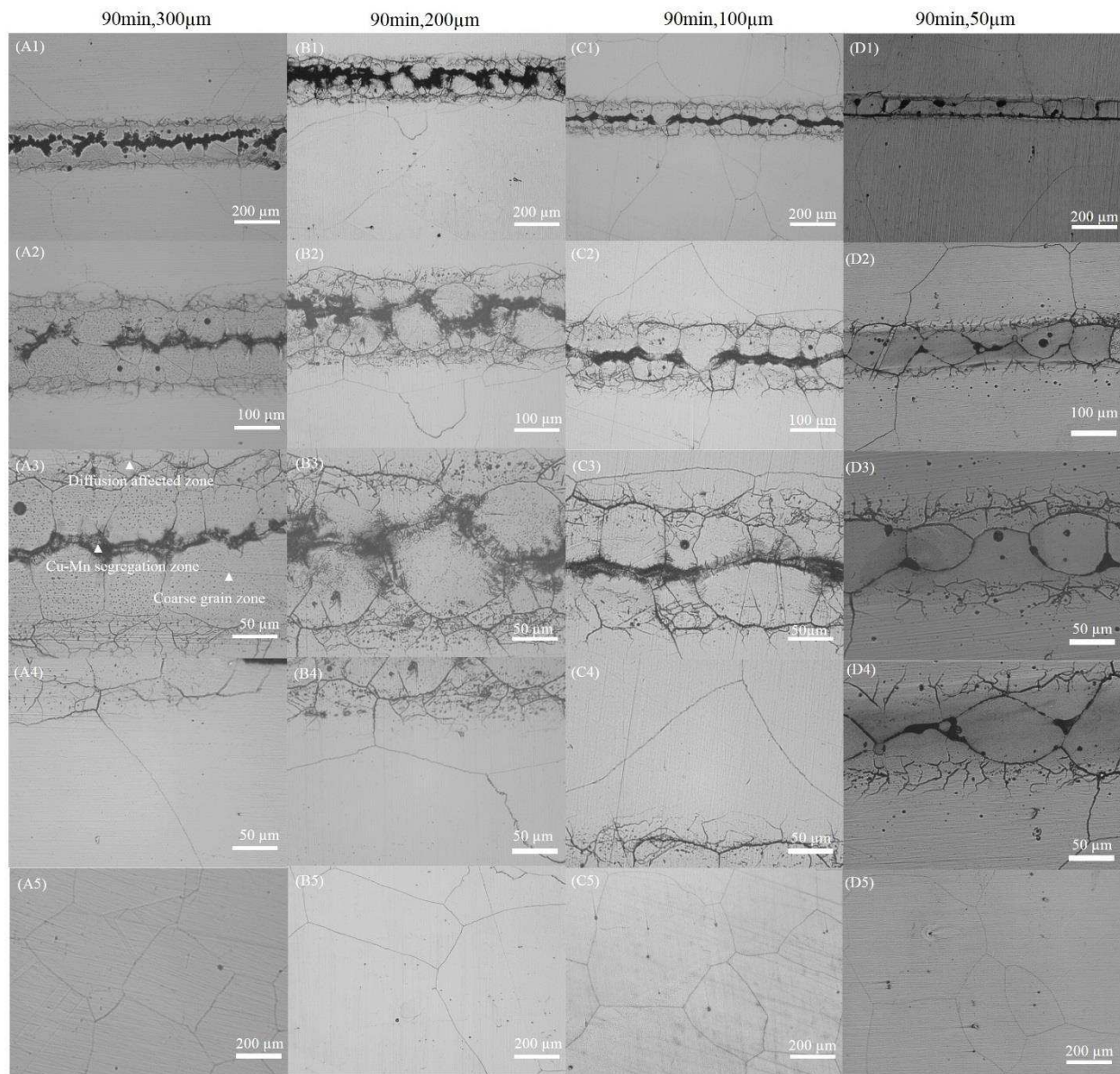


Figure 4.39 Microstructure of the joint brazed at 1200 °C for 90 min by a filler foil with a thickness of (A1-A5)300 μm, (B1-B5)200 μm, (C1-C5)100 μm, and (D1-D5)50 μm

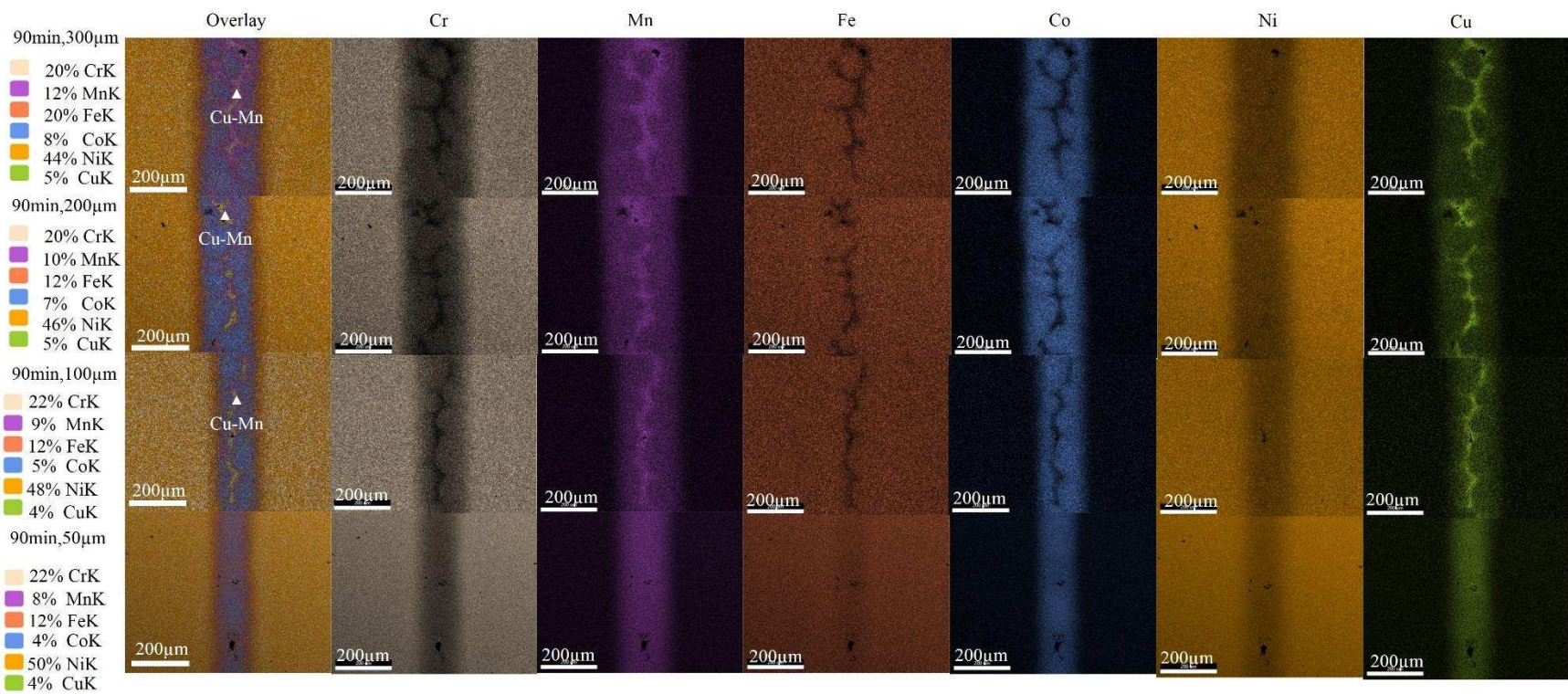


Figure 4.40 EDS element maps in joints brazed at 1200 °C for 90 min using HEA filler foil with 300, 200, 100, and 50 μm thicknesses

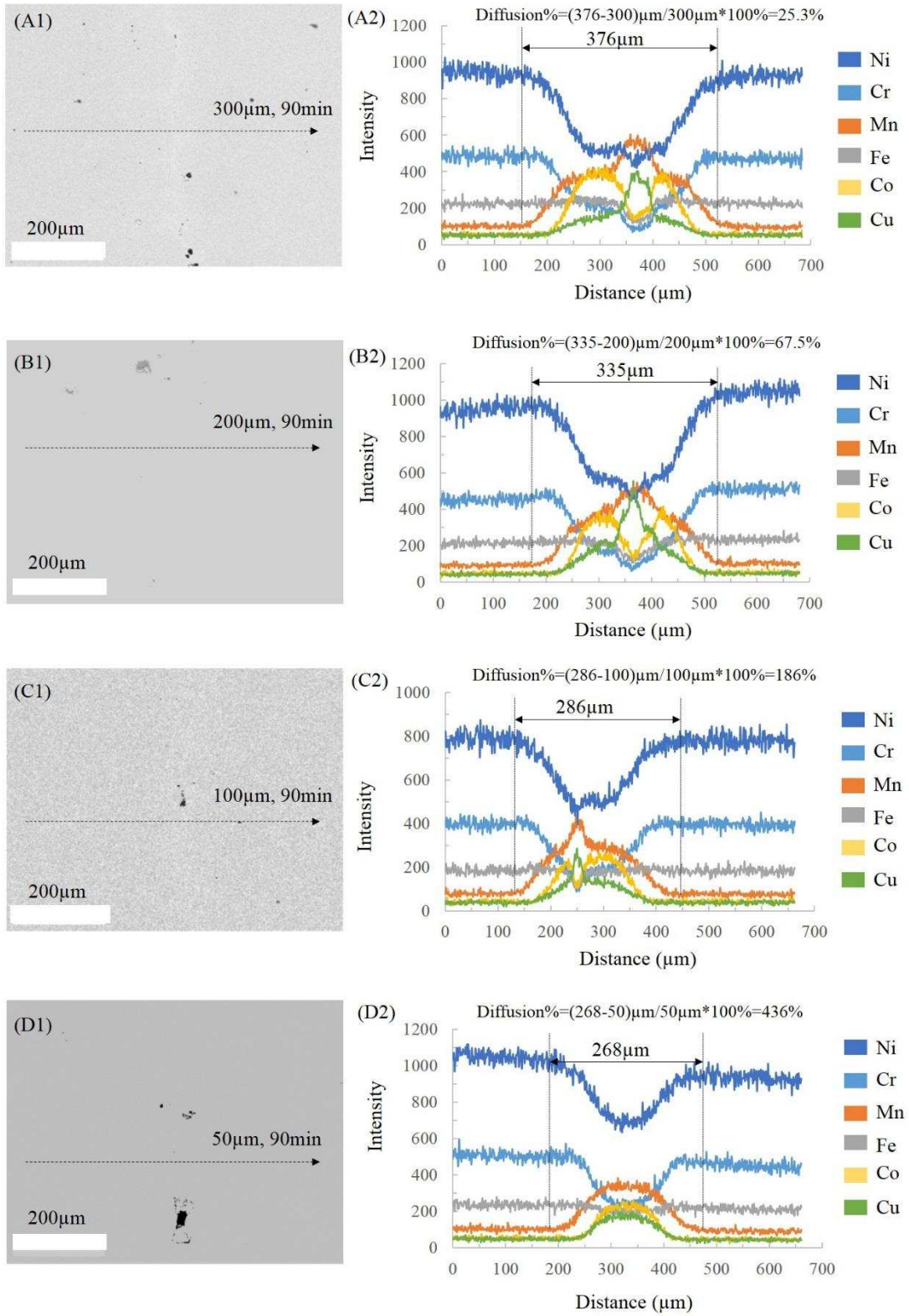


Figure 4.1 EDS line scanning of joint brazed using HEA filler foil with different thicknesses when brazing temperature and brazing time are fixed at 1200 °C and 90 min. (A1-A2)300 $\mu\text{m}$  (B1-B2)200 $\mu\text{m}$  (C1-C2)100 $\mu\text{m}$  (D1-D2)50 $\mu\text{m}$

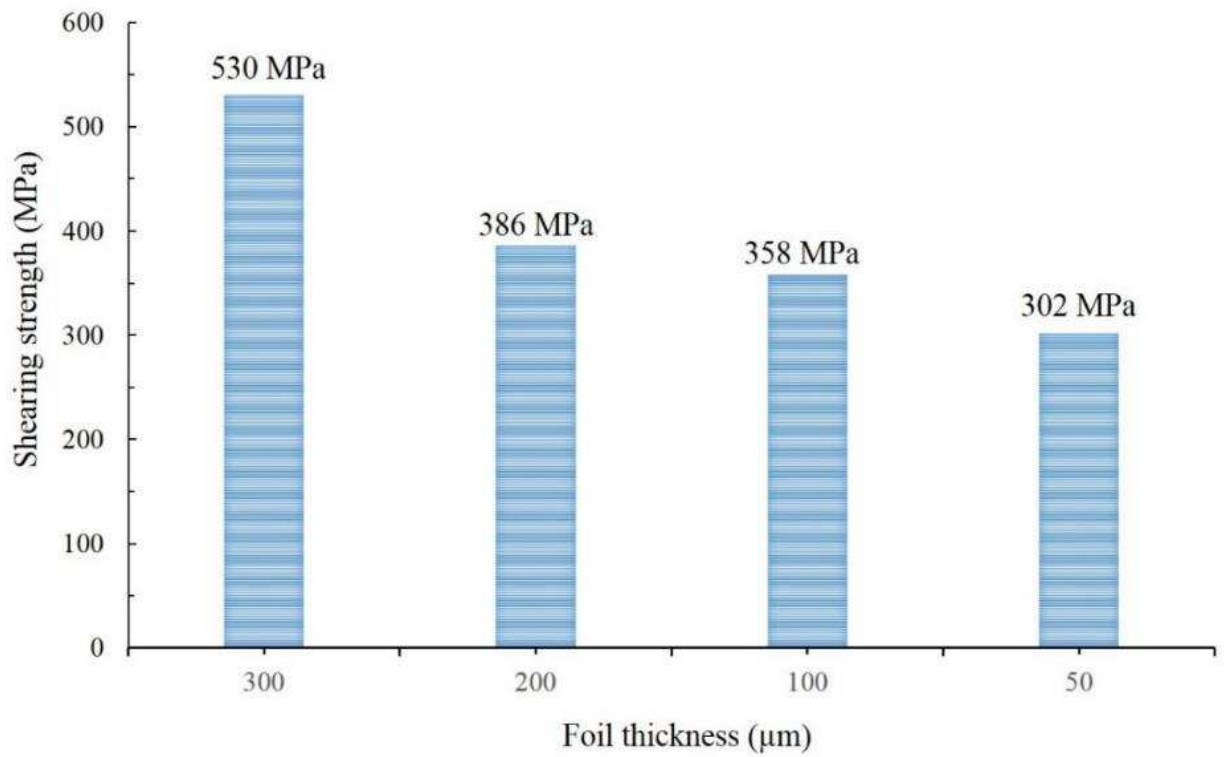


Figure 4.42 Shear strength of the Inconel 600/ $\text{Fe}_5\text{Co}_{20}\text{Ni}_{20}\text{Mn}_{35}\text{Cu}_{20}$  HEA/Inconel 600 joint brazed by 50, 100, 200, and 300  $\mu\text{m}$  thick foils with brazing time and brazing temperature fixed at 90min and 1200 °C.

## CHAPTER 5

### HEA/AL MELT INTERFACE REACTION

#### 5.1 Selection of the HEA composition

There are several requirements on the mold materials for aluminum alloys casting.

1. Much higher melting temperature than aluminum to ensure that the mold will not soften after contacting the aluminum melt. Mold should have good thermal stability.
2. Combination of good ductility and high strength
3. Large difference between thermal expansion coefficients of mold materials and aluminum alloy
4. Poor wetting and very little interface reaction with aluminum melt

A newly reported HEA with a composition of FeCoNi(AlSi)<sub>0.2</sub> satisfies these requirements quite well. The change of mole mixing entropy ( $\Delta S_{mix}$ ) and mixing enthalpy ( $\Delta H_{mix}$ ), atomic size difference ( $\delta$ ) and valance electrons concentration (VEC) are all calculated according to Equation 1-7 in table 4.1.  $\delta=4.44\%<6\%$ ,  $\Delta H_{mix}=-12.28$  KJ/mol,  $\Delta S_{mix}=1.42$  J/(mol\*K),  $\Delta G_{mix}=\Delta H_{mix}-T\Delta S_{mix}<0$ . It satisfies all the requirements to form a HEA proposed by Zhang et.al<sup>69</sup>. Also VEC equals to 8.23, larger than 8, which means a FCC HEA could be formed according to the VEC principle proposed by Guo et.al<sup>85</sup>. In addition, below are the reasons to confirm FeCoNi(AlSi)<sub>0.2</sub> HEA satisfies the requirements on mold materials for aluminum alloy casting.

1. The melting point of FeCoNi(AlSi)<sub>0.2</sub> HEA can be predicted by Equation 10 shown below. It is calculated as 1454 °C, similar to the melting point of current mold materials, mold steels.

$$T_m = \sum_{i=1}^n C_i T_i \quad \text{Equation 10}$$

2. HEA has good thermal stability.
3. FeCoNi(AlSi)<sub>0.2</sub> has a compression yield strength of 500 MPa, an ultimate compression strength of 200 MPa and a fracture strain of 50%, showing a combination of high strength and good ductility.
4. The linear thermal expansion coefficient FeCoNi(AlSi)<sub>0.2</sub> HEA has been predicted according to the Equation 7. It is calculated as  $12.32 \times 10^{-6}/K$ , showing obvious difference with the linear thermal expansion coefficient of pure aluminum, which is  $23 \times 10^{-6}/K$ .
5. Except Al, the other four elements contained in FeCoNi(AlSi)<sub>0.2</sub> HEA are Fe, Co, Ni, and Si, all having low activity than Al. So the interface reaction should be limited. Moreover, it has been reported that the surface oxidation of the mold materials is good for improving its resistance to corrosion of aluminum melt.

Table 5.5 Mixing enthalpy ( $\Delta H_{\text{mix}}$ ), mixing entropy ( $\Delta S_{\text{mix}}$ ), atomic size difference ( $\delta$ ), linear thermal expansion and valence electron concentration of FeCoNi(AlSi)<sub>0.2</sub> system

Element couple	Fe-Co	Fe-Ni	Fe-Al	Fe-Si	Co-Ni	Co-Al	Co-Si	Ni-Al	Ni-Si	Si-Al	Total
$\Delta H_{\text{mix}}$ (KJ/mol)	-0.15	-0.42	-0.76	-2.43	0	-1.32	-2.64	-1.53	-2.78	-0.26	-12.29
Element	Fe	Co	Ni	Al	Si	Total					
Mole fraction	0.294	0.294	0.294	0.059	0.059						
$\Delta S_{\text{mix}}$ (J/mol*K)	0.36	0.36	0.36	0.17	0.17	1.42					
Element	Fe	Co	Ni	Al	Si	Total					
Mole fraction	0.294	0.294	0.294	0.059	0.059						
Atomic radius (pm)	126	125	124	143	111	125.24					
$C_i*(1-r_i/r)*(1-r_i/r)$	1.08E-05	1.08E-06	2.88E-05	1.19E-03	7.63E-04	0.045					
Element	Fe	Co	Ni	Al	Si	Total					
Mole fraction	0.294	0.294	0.294	0.059	0.059						
linear thermal expansion ( $\mu$ /K)	12	12	13	23	2.6	12.39					
Element	Fe	Co	Ni	Al	Si	Total					
Mole fraction	0.294	0.294	0.294	0.059	0.059						
Valence electron concentration	8	9	10	3	4	8.351					
Ci: mole fraction of element i											
ri: atomic radius of element i											
r: average atomic radius of HEA											

## 5.2 Fabrication and characterization of FeCoNi(AlSi)<sub>0.2</sub> HEA

Figure 5.1 shows the microstructure and the composition of the as-cast FeCoNi(AlSi)<sub>0.2</sub> HEA. A typical as-cast microstructure is observed. The alloy is consisted of dendrite and inter dendrite structure with different compositions. Grain boundary segregation is found in the EDS spotting test result shown. The composition of the inter dendrite is Al: 9.07 at%, Si: 11.41 at%, Fe: 21.62%, Co: 23.34%, Ni: 34.76% and the composition of the dendrite area is Al: 5.73 at%, Si: 4.65 at%, Fe: 30.9 at%, Co: 29.84%, Ni: 28.78 at%. The dendrite is rich in Fe and Co while the inter dendrite area is rich in Al, Si and Ni. Compared with the composition segregation in Fe<sub>5</sub>Co<sub>20</sub>Ni<sub>20</sub>Mn<sub>35</sub>Cu<sub>20</sub>, the segregation tendency of Fe, Co, Al and Si is the same while Ni shows the opposite tendency in FeCoNi(AlSi)<sub>0.2</sub>. The segregation of Fe, Co, Al and Si can be explained by the difference of melting points among the elements. Fe and Co has relatively higher melting points while Al and Si have relatively lower melting points. During the solidification of metallic

liquid, Fe and Co were solidified first while Al and Si were ejected to the inter dendrite or grain boundary areas, solidified later. So the dendrite area is rich in Fe and Co while the inter dendrite area is rich in Al and Si. However, according to the melting difference, the dendrite area instead of the inter dendrite area, should be rich in Ni. The possible reason is, as shown in Table 5.1 among all the binary element couples Ni-Si has the most negative enthalpy. So Ni tends to stay together with Si. While the inter dendrite area is rich in Si, it is also rich in Ni. Figure 5.2 shows the XRD curve of the as-cast FeCoNi(AlSi)<sub>0.2</sub> HEA. Only the peaks of one FCC phase is observed on the curve. The positions of the peaks are exactly the same with the peaks of “FeCoNi” ternary alloy. There are two possible reasons to explain this. First, both the dendrite and the inter dendrite have a FCC phase structure. Their Crystal parameters are very close. So their diffraction peaks are overlapping and it is difficult to separate their peaks on the XRD curve. Second, the volume fraction of the inter dendrite is lower than 5%, which is too low to be detected by XRD technique. The valance electron concentration of the alloy, 8.3, is calculated in section 4.1, which predicts the alloy is supposed to have a FCC phase structure. The XRD result confirms this prediction. Figure 5.3 shows the DTA curve of the as-cast HEA. Two endothermic peaks are observed on the curve. The first peak appears around 160 °C, which is corresponded to the vaporization of the impurity absorbed on the sample surface. The second peak appears at 1340 °C, indicating the melting of HEA. So the melting point of HEA is measured as 1340 °C here. Figure 5.4 and Figure 5.5 show the engineering stress-strain and true stress-strain curves of FeCoNi(AlSi)<sub>0.2</sub> for compression test. The compression tests are repeated three times. Sample 1 was tested on the CSM Alliance RT-1000 machine while sample 2 and 3 were compressed on the Instron machine. The CSM Alliance RT-1000 machine has a higher load measurement uncertainty (20lbs) than Instron (1lb). A stage is found in the elastic deformation zone of sample 1’s compression curve but this stage disappears from the compression curves of sample 2 and 3. Averaging the data from three tests, the as-cast FeCoNi(AlSi)<sub>0.2</sub> has an engineering yield strength of 443 MPa, an ultimate compression strength of 1323 MPa and an engineering fracture strain of 56%. Also, reading from the true stress-strain curves, the true yield strength, true ultimate compression strength and true fracture strain are 460 MPa, 647 MPa and 128%, respectively. Compared with the literature reported mechanical properties of FeCoNi(AlSi)<sub>0.2</sub>, the alloy fabricated in this study has a lower strength but a similar ductility. One possible reason to explain the difference is that there are some defects in the HEA button after arc melting. The defects decreased the strength of the alloy.

In a word, an FCC HEA having a high strength, good ductility, and good thermal stability has been successfully fabricated in this study. It is a good candidate as mold materials for casting of aluminum alloys.

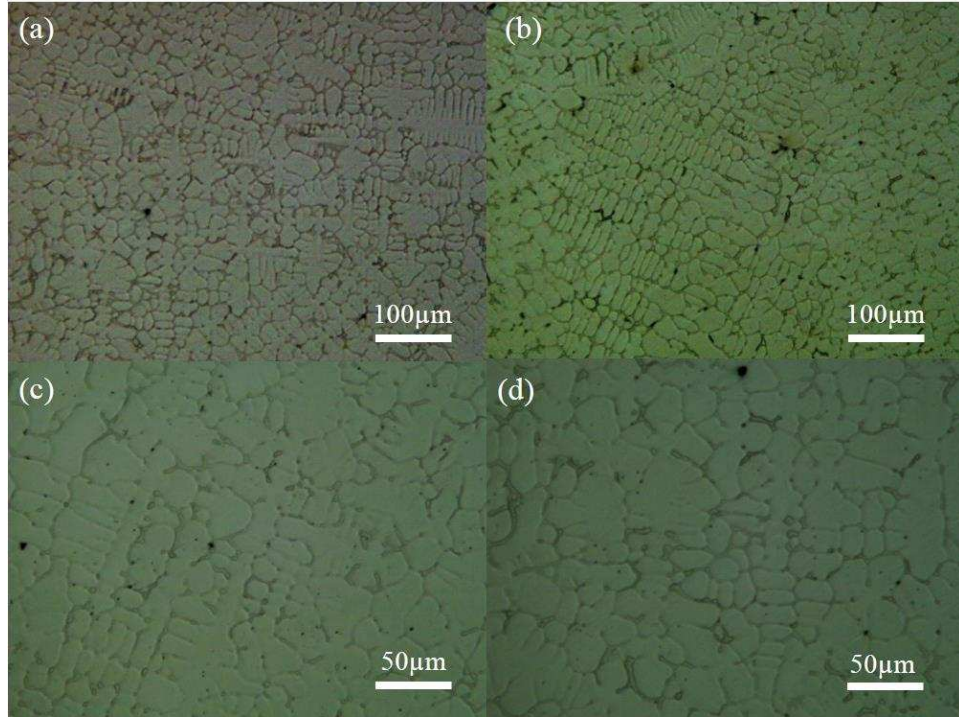


Figure 5.43 OM images showing the microstructure of the as-cast FeCoNi(AlSi)<sub>0.2</sub> HEA

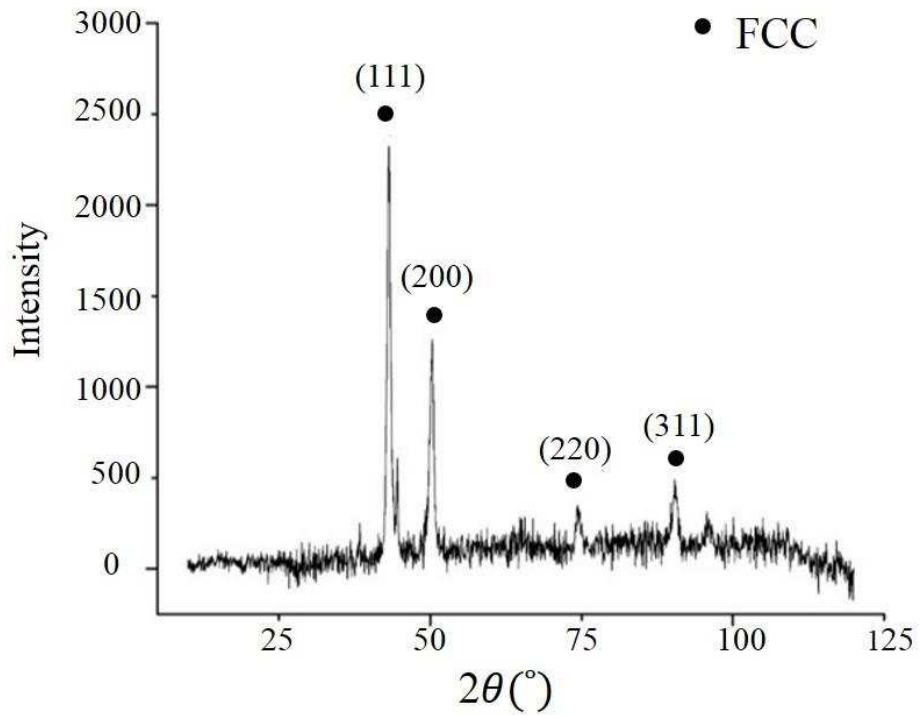


Figure 5.44 XRD curve of the as-cast FeCoNi(AlSi)<sub>0.2</sub> HEA

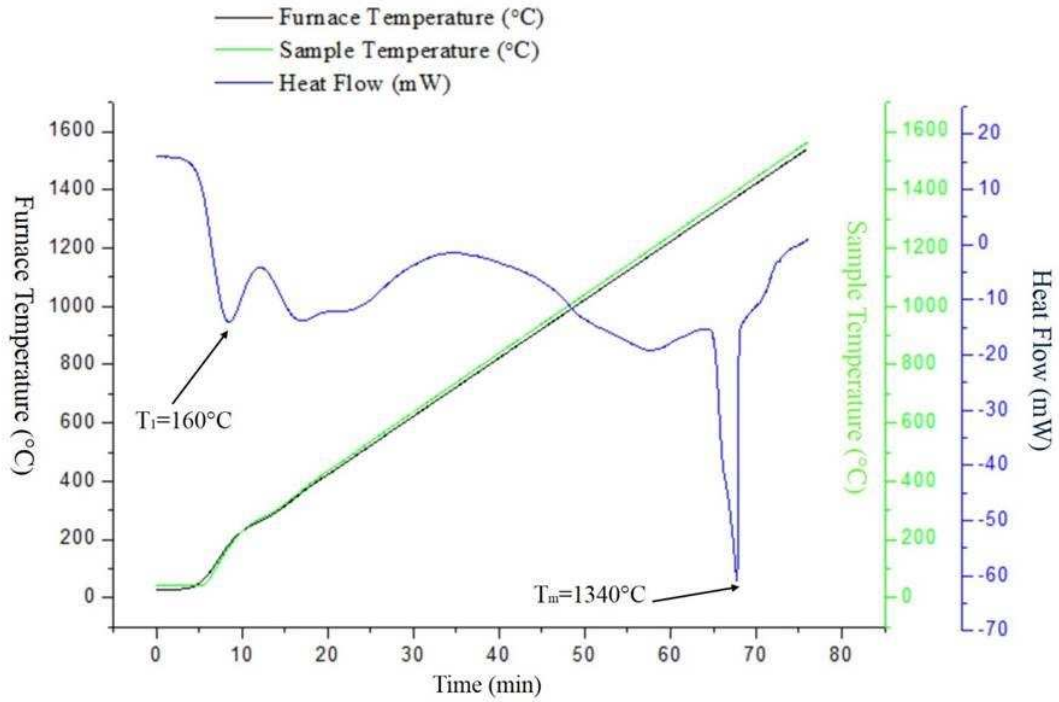


Figure 5.45 DTA curve of the as-cast FeCoNi(AlSi)<sub>0.2</sub> HEA

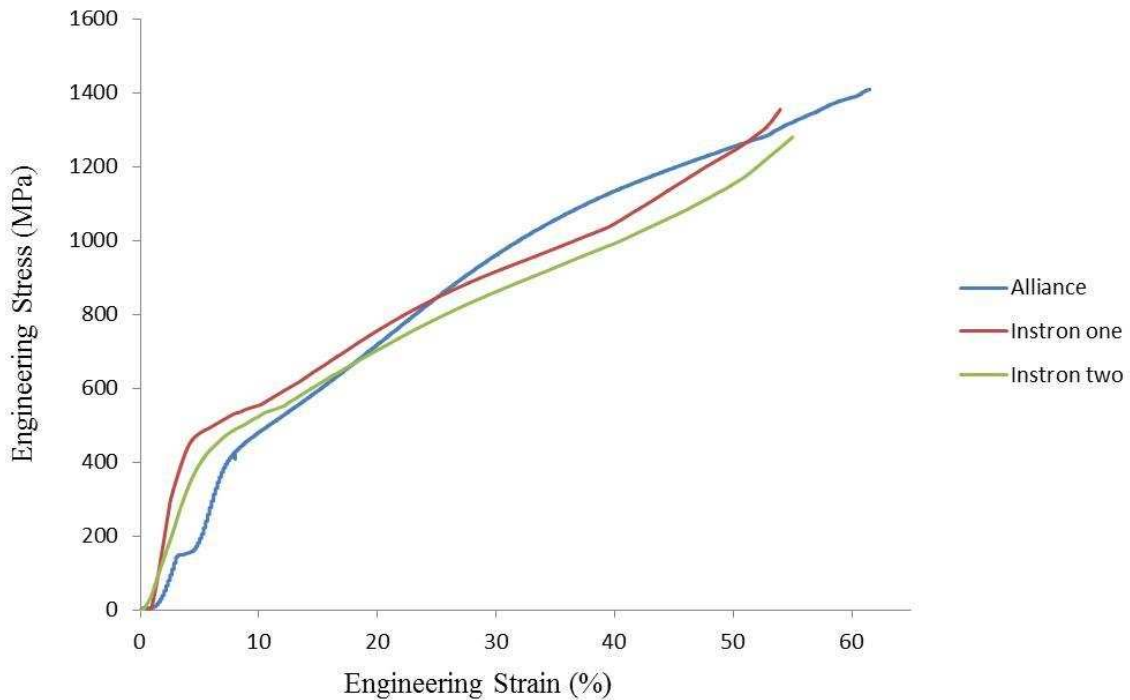


Figure 5.46 Engineering stress-strain curves of the as-cast FeCoNi(AlSi)<sub>0.2</sub> HEA during compression tests on Alliance and Instron machine. Strain rate is fixed at  $4 \times 10^{-4}$ /s.

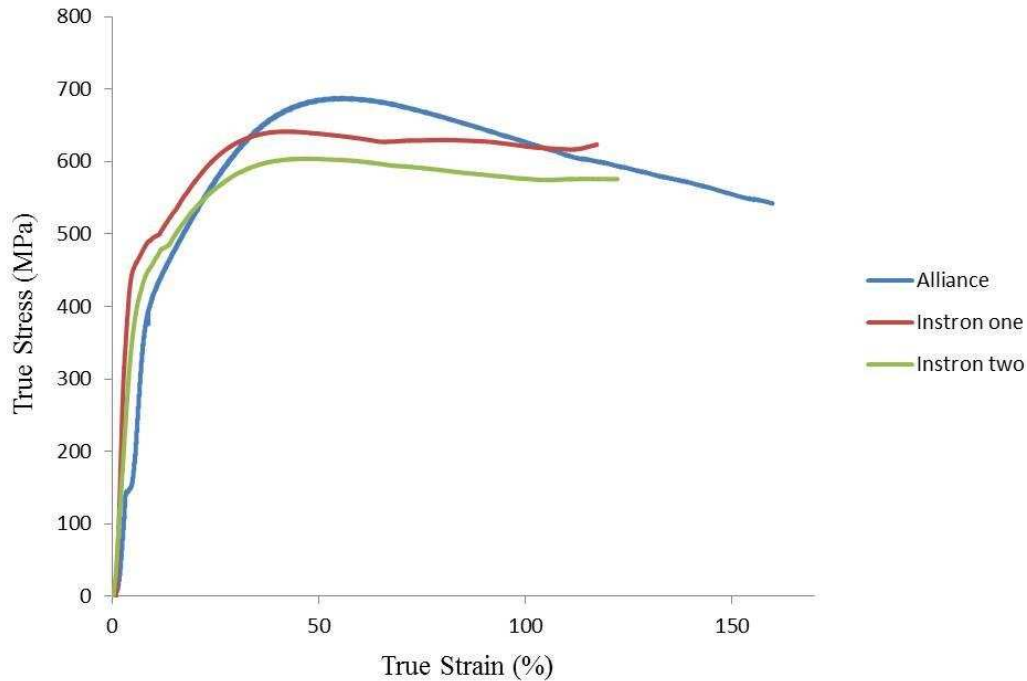


Figure 5.47 True stress-strain curves of the as-cast FeCoNi(AlSi)<sub>0.2</sub> HEA during compression tests on Alliance and Instron machine

### 5.3 Effect of temperature on the oxidation layer on the surface of FeCoNi(AlSi)<sub>0.2</sub> HEA

Figure 5.6 shows the microstructure and the composition of the oxidation layer on the surface of FeCoNi(AlSi)<sub>0.2</sub> alloy after 5 hours' oxidation treatment at 800 °C in a regular furnace. It can be observed the oxidation layer can be divided into two sub-layers with different microstructure and compositions, the inner layer close to HEA matrix and the outer layer close to the mount material. Some defects are found on the outer layer. The average thickness of inner layer is 15µm while the average thickness of the outer layer is 10 µm. EDS spotting tests were carried out on two layers in order to identify their compositions. The composition of the outer layer is O: 22.43 at%, Fe: 10.72 at%, Co: 5.40 at%, Ni: 18.35 at%, Al: 20.04 at%, Si: 23.07 at% and the composition of the inner layer is O: 54.07 at%, Fe: 0.18 at%, Co: 0.18 at%, Ni: 30.14 at%, Al: 14.70 at%, Si: 0.74 at%. Comparing the composition of two layers, it can be seen that almost the concentration of Fe, Co and Si in the outer layer is much lower than the concentration of Fe, Co and Si in the inner layer. Nearly no Fe, Co or Si is detected in the outer layer. The outer layer is mainly consisted of O, Al and Ni. The concentration of Ni in the outer layer is higher than the inner layer while the concentration of Al in the outer layer is lower than the inner layer. It can be inferred that once the oxidation happens, the elements with lowest oxidation resistance, Al and Ni are oxidized first while the other elements with higher oxidation resistance, Fe, Co and Si are ejected into the outer layer and oxidized later. Except the formation

of oxidation layer on the surface, the HEA still maintains its uniform microstructure and composition, showing its good thermal stability.

Figure 5.7 shows the microstructure and the composition of the oxidation layer on the surface of FeCoNi(AlSi)<sub>0.2</sub> alloy after 5 hours' oxidation treatment at 1000 °C in a regular furnace. With the increase of the oxidation temperature, the total thickness of the oxidation layer has increased to 100 μm and its composition also becomes more complex. The layer is consisted of three sub layers, which are inner layer, middle layer, outer layer in the direction from the HEA side to mounting materials side. EDS spotting tests were carried out on three sub layers to identify the compositions. The compositions of three inner, middle, outer layers are O: 22.43 at%, Fe: 35.88 at%, Co: 5.05 at%, Ni: 3.77 at%, Al: 3.77 at%, Si: 3.45 at%, O: 44.62 at%, Fe: 4.08 at%, Co: 2.69 at%, Ni: 3.04 at%, Al: 16.79 at%, Si: 28.78 at% and O: 43.59 at%, Fe: 5.35 at%, Co: 3.78 at%, Ni: 3.40 at%, Al: 13.10 at%, Si: 30.78 at%. All the three sub layers have a similar oxygen concentration around 49 at%. The outer layer formed at 1000 °C has similar composition with the layer formed at 800 °C. The only difference is the content of Si has increased. But Si mainly concentrates in the middle layer. Fe and Co are nearly not detected in the outer layer. The outer layer is mainly consisted of O, Ni, Al, and Si. Ni shows the highest concentration in the outer layer, which means Ni is first oxidized when the reaction starts. Ni has the lowest oxidation resistance among all the elements. Al and Si shows the highest concentration in the middle layer, so it can be inferred that after Ni, Al and Si are then oxidized. Considering the fact that in the 800 °C Al is oxidized earlier than Si, it is judged that Al is the second lowest oxidation resistance element and Si is the third lowest oxidation resistance element. Fe and Co shows the highest in the inner layer, closet to the matrix. So Fe and Co are the two elements with highest oxidation resistance. Above all, the oxidation resistance of the elements can be ordered, Ni<Al<Si<Fe, Co, which is in an agreement with the thermal stability of Fe, Co and Ni. Like the 800 °C sample, except the oxidation layer, the HEA matrix still maintains its uniform microstructure and composition, indicating a good thermal stability even at 1000 °C.

Effect of temperature on the oxidation of HEA is investigated in this section. With the increase of temperature, the oxidation layer becomes thicker, the composition and microstructure become more complex. As for the application to be used as a mold material for aluminum alloy casting, a thick layer with the ability to protect the mold from attack of aluminum melt is needed. So the 800 °C oxidation treatment is chosen here to carry out the interface reaction experiment between oxidized HEA and aluminum melt.

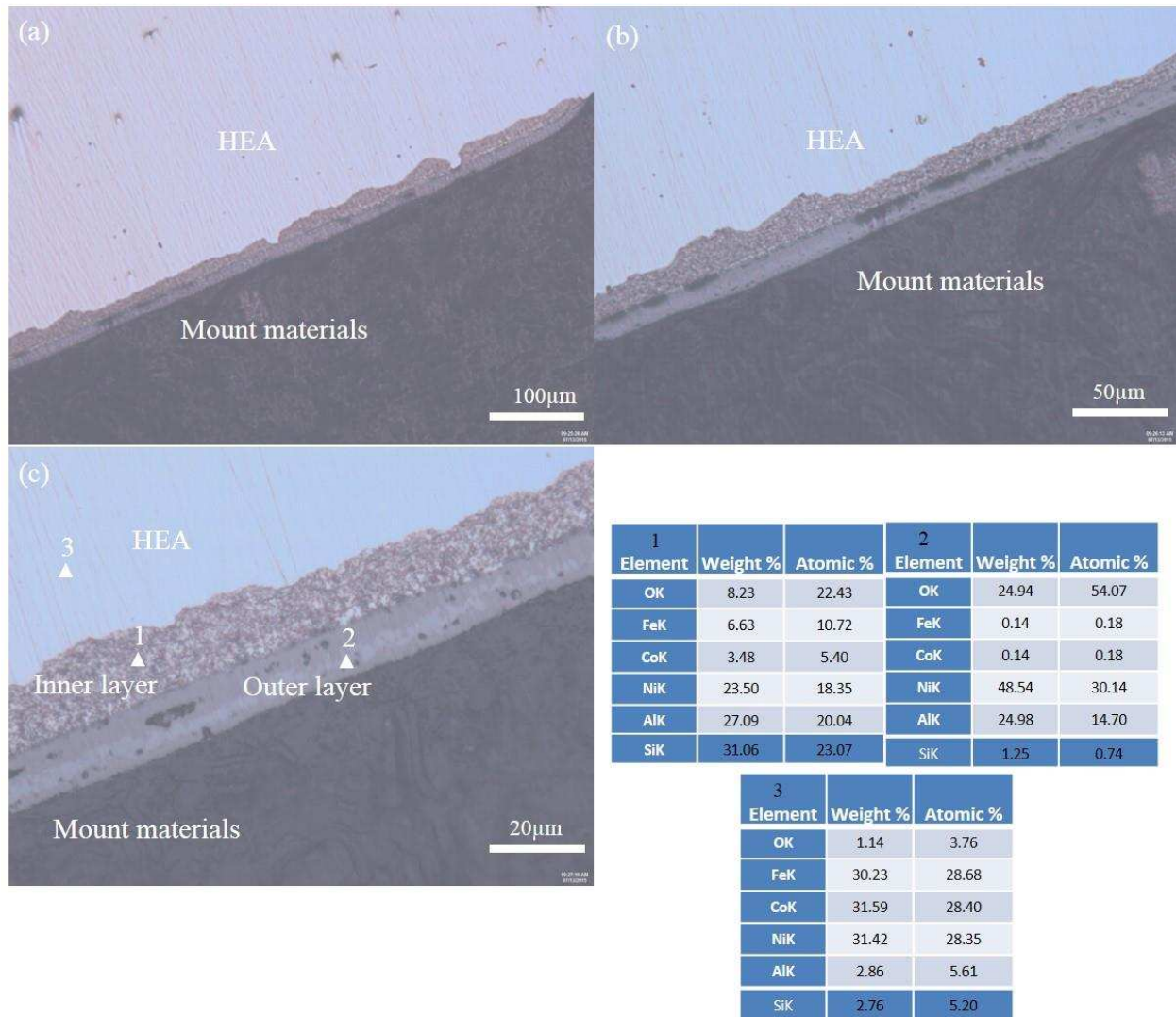


Figure 5.48 (a-c) Microstructure and composition of FeCoNi(AlSi)<sub>0.2</sub> HEA after oxidation at 800 °C after 5 hours in the regular furnace. The composition of the as-cast HEA is Fe:29.4at%, Co:29.4at%, Ni:29.4at%, Al: 5.9at%, Si: 5.9at%.

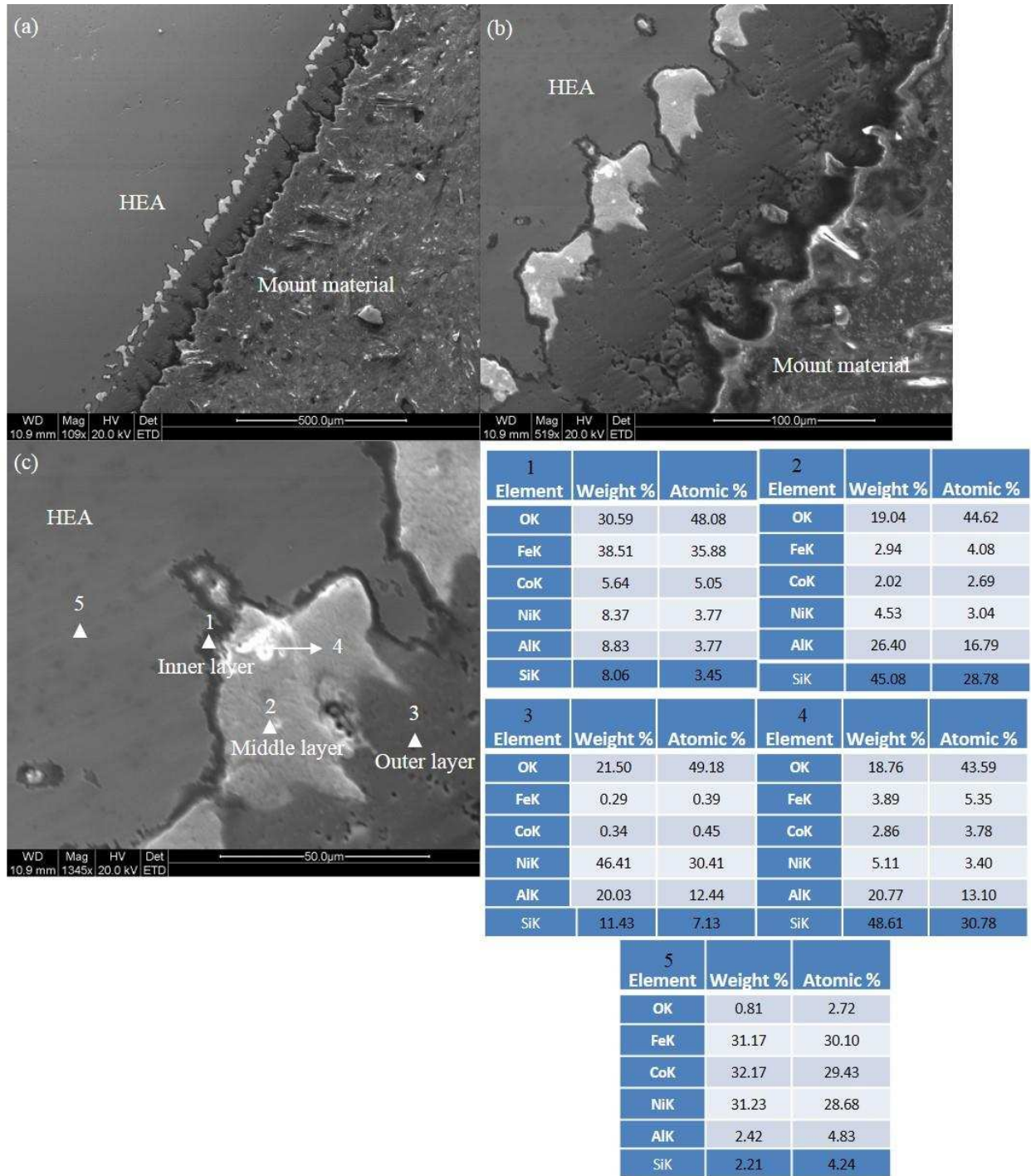
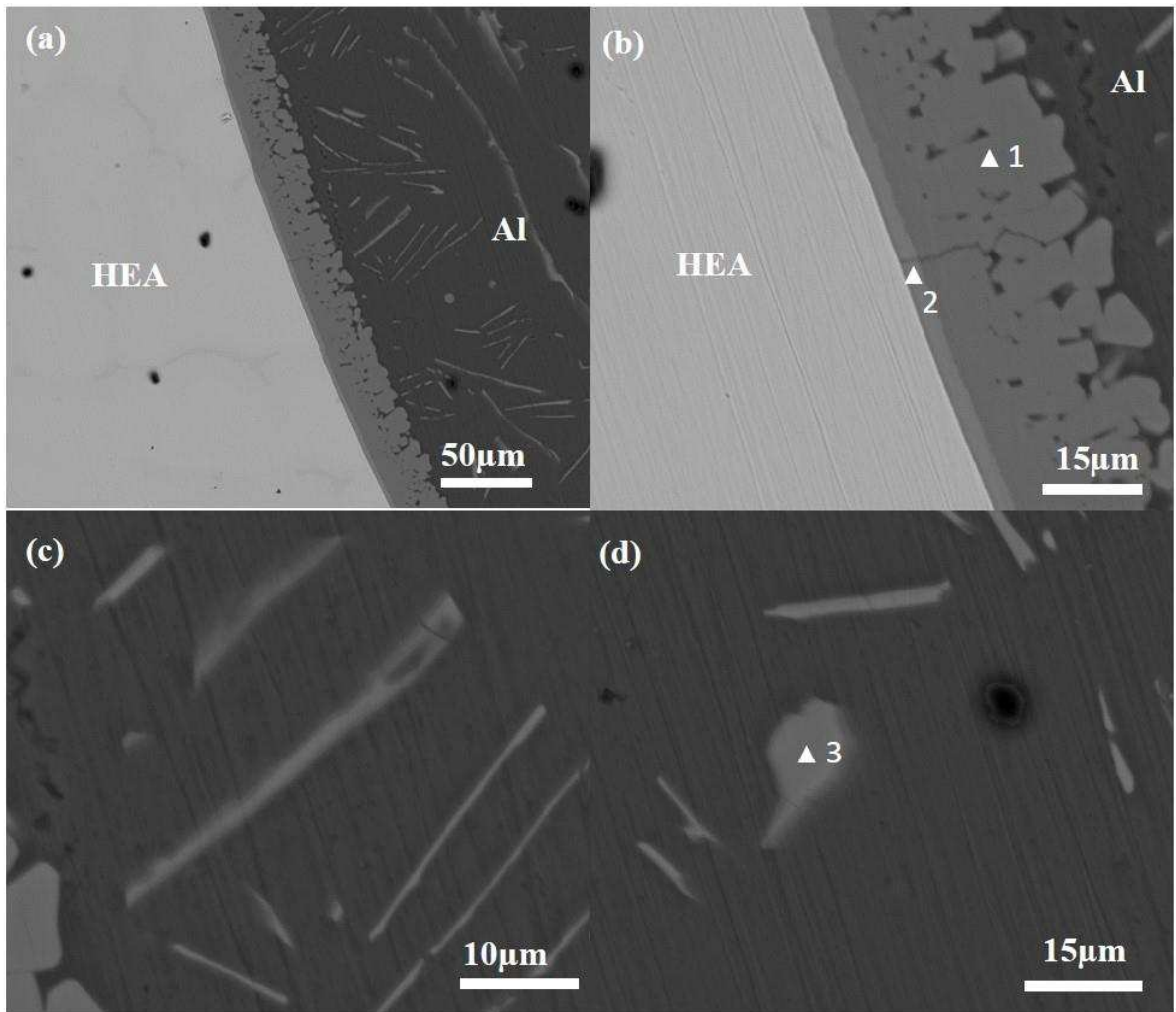


Figure 5.49 (a-c) Microstructure and composition of FeCoNi(AlSi)<sub>0.2</sub> HEA after oxidation at 1000C after 5 hours in the regular furnace. The composition of the as-cast HEA is Fe:29.4at%, Co:29.4at%, Ni:29.4at%, Al: 5.9at%, Si: 5.9at%.

#### 5.4 Interface reaction between Al melt and as-cast HEA, and oxidized HEA

In order to evaluate the potential of HEA to be used as the mold material for casting of aluminum alloys, the interface experiment between aluminum melt and as-cast HEA, oxidized HEA and pure Fe are carried out separately at 700 °C in the regular furnace for one hour. Figure 5.8 shows the microstructure and composition of the interface between as-cast HEA and Al melt after reacting at 730 °C for one hour. Two transition layers between HEA and Al are found. The inner layer close to HEA with a thickness of 6.1µm is a continuous and dense while the outer layer close to Al with a thickness of 22.5µm is non-continuous and loose. The inner layer has lower Al concentration and higher Si, Fe, Co and Ni concentration while the outer layer has higher Al concentration and lower Si, Fe, Co and Ni concentration. It can be inferred that the inner layer forms first and the outer layer forms later during the reaction between HEA and Al melt. The HEA still maintains a uniform microstructure and composition. However, precipitation phases were found in Al matrix, indicating diffusion of Fe, Co and Ni from HEA to Al melt. Figure 5.9 shows the microstructure and composition of the interface between pure Fe and Al after reacting at 730 °C for two hours. There are also two transition layers found. The inner layer close to Fe is FeAl<sub>3</sub> intermetallic compound while the outer layer close to Al is Fe<sub>2</sub>Al<sub>5</sub> intermetallic compound. The average thickness of the two transition layers is around 200 µm, more than 7 times of the thickness of the transition layer formed between as-cast HEA and Al melt. Figure 5.10 shows the microstructure and composition of the interface between oxidized HEA (800 °C-5h) and Al melt after reacting at 730 °C for one hour. A transition layer is also observed however the thickness of the transition layer has been reduced to less than 10 µm. The reaction between HEA and Al melt is weakened by the oxidation layer. Moreover, nearly no precipitation phases can be found in Al, indicating that the oxidation layer also prevents the diffusion of elements from HEA to Al melt. In some areas, the oxidation layer is broken so the HEA is attacked by aluminum melt directly.

In a word, the oxidized HEA has a better ability than as-cast HEA and pure Fe to protect the mold from being attacked by aluminum melt, showing the potential to be used as a mold material for casting or forging of aluminum alloys.



1			2			3		
Element	Weight %	Atomic %	Element	Weight %	Atomic %	Element	Weight %	Atomic %
OK	1.01	2.07	OK	1.06	2.36	OK	1.41	2.84
FeK	9.92	5.80	FeK	15.02	9.58	FeK	7.70	4.42
CoK	17.22	9.54	CoK	16.70	10.10	CoK	2.80	1.52
NiK	6.55	3.64	NiK	15.05	9.13	NiK	20.94	11.44
AlK	65.20	78.85	AlK	51.41	67.87	AlK	66.91	79.52
SiK	0.09	0.11	SiK	0.76	0.96	SiK	0.23	0.27

Figure 5.50 (a-d) Microstructure and composition of the interface between as-cast HEA and solidified pure Al

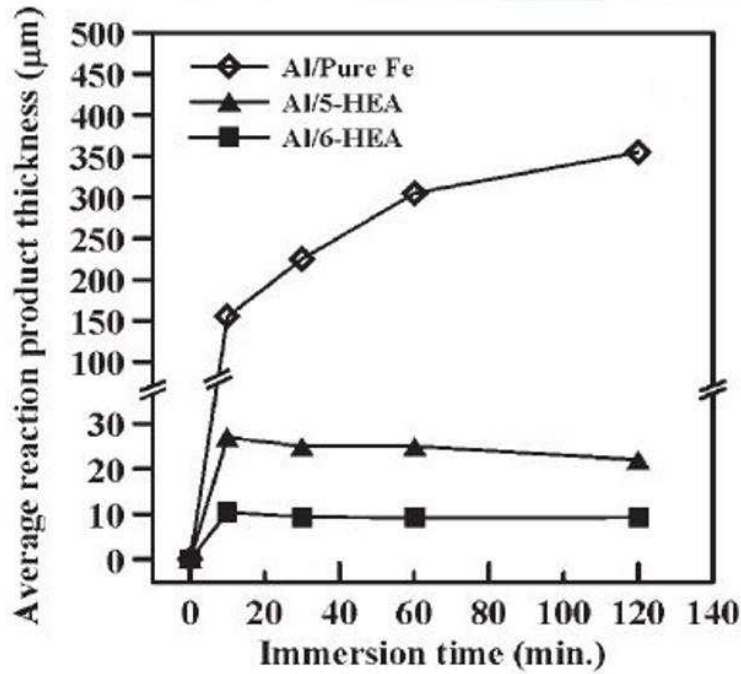
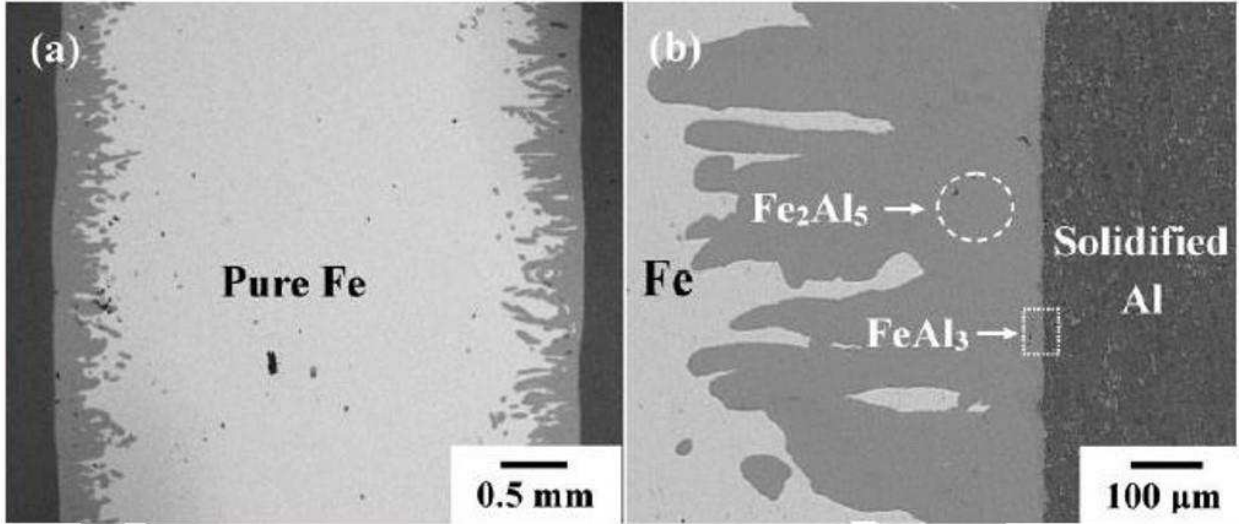


Figure 5.51 (a-b) Microstructure of the interface between pure Fe and solidified Al (c) average thickness of reaction layer varying with immersion time for pure Fe, FeCoNiMnCr (5-HEA) and FeCoNiCrMnAl (6-HEA)<sup>17</sup>.

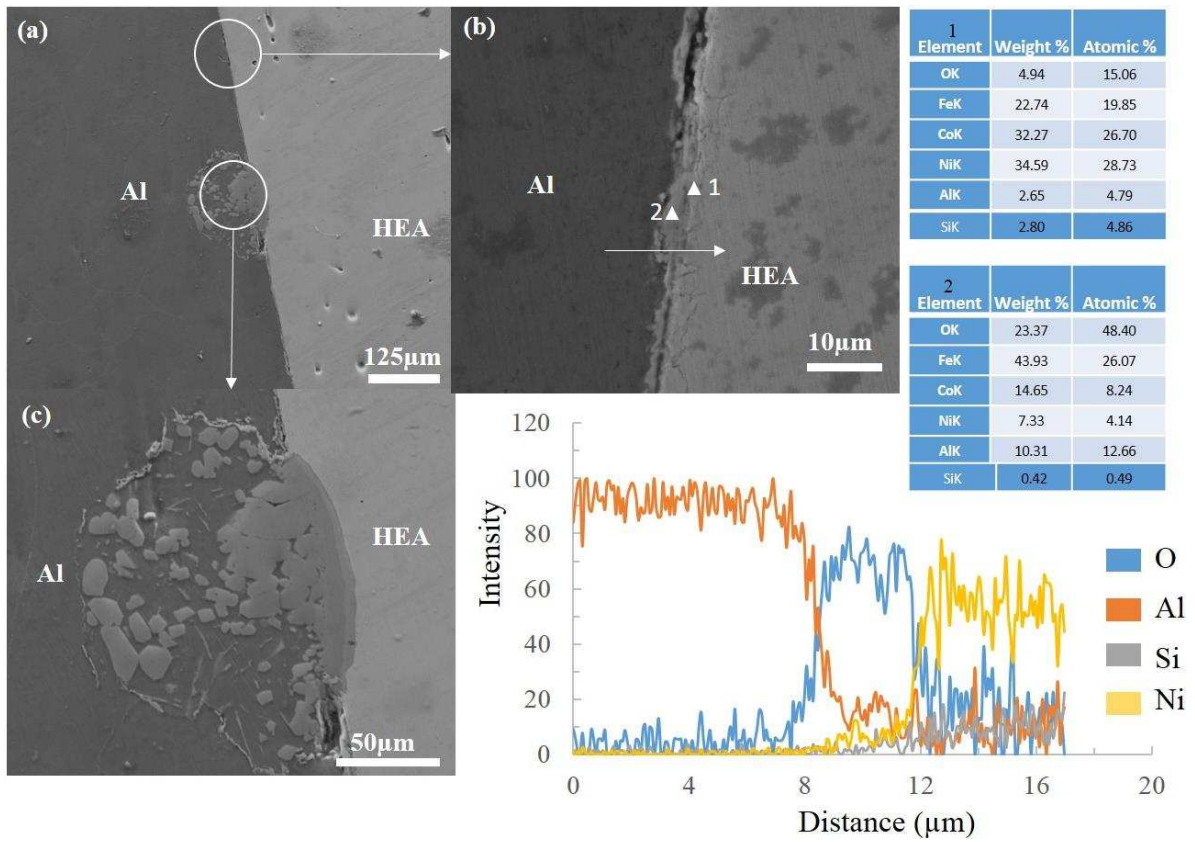


Figure 5.52 (a-c) Microstructure and composition of the interface between oxidized (800 °C, 5h) HEA and solidified pure Al

## CHAPTER 6

### RESEARCH SUMMARY AND CONCLUSIONS

A double FCC phase HEA with a composition of  $\text{Fe}_5\text{Co}_{20}\text{Ni}_{20}\text{Mn}_{35}\text{Cu}_{20}$  was designed by Thermo-Calc software using the HEA 1.0 database and fabricated by arc melting. The as-cast HEA shows a melting range of 1080-1150 °C, only 5 °C different from the melting range predicted by Thermo-Calc. It can be concluded that the newly published database HEA1.0 could provide a very accurate melting range and phase structure of HEA. It is a very useful tool to design the composition of HEA. The HEA has a similar strength, hardness and linear thermal expansion coefficient with Inconel 600 alloy, which is good for bonding between HEA and Inconel 600 during brazing.

Second, wetting angle tests of as-cast HEA on Inconel 600 alloy substrate were made at different temperatures (1160, 1180, 1200, and 1250 °C) for 30 min. HEA shows a good wetting (wetting angle 14.2°) on Inconel 600 without over spreading at 1200 °C. Thus, 1200 °C was chosen as the brazing temperature.

Third, as cast  $\text{Fe}_5\text{Co}_{20}\text{Ni}_{20}\text{Mn}_{35}\text{Cu}_{20}$  HEA buttons were rolled to different final thicknesses (300, 200, 100, and 50  $\mu\text{m}$ ). Inconel 600 alloy was brazed by HEA filler foil with different thickness at 1200 °C for different times (15, 30, 45, 60, 90, and 120 min). It was found that when the foil thickness is fixed at 300  $\mu\text{m}$ , a maximum shear strength of 530 MPa was achieved at 90 min. The Cu-Mn segregation zones were found in the center of all the brazed joints while Cr-Mn segregation zone is only found in the 120 min joint. The volume fraction of Cu-Mn rich phase decreases with the increase of brazing time. Co, Cu, and Mn diffused into base metal Inconel 600 alloy while Cr and Mn diffused into HEA from Inconel 600 alloy. Among Co, Cu and Mn, Mn has the largest diffusion distance because of its lowest activation energy. The inter-diffusion behavior between HEA is also promoted by the increase of brazing time. When the foil thickness was fixed at 50  $\mu\text{m}$ , a maximum shear strength of 310 MPa was achieved at a brazing time of 60 min. When the brazing time was fixed at 90 min, the shear strength of the brazed joint decreases with the decrease of foil thickness. Only Cu-Mn rich phases were found in the brazed joints. The volume fraction of Cu-Mn rich phase decreases with the decrease of foil thickness while the inter-diffusion behavior between HEA is also promoted by the decrease of foil thickness. DIC was also used to measure the strain distribution among the sample. It is shown that the HEA undertakes more deformation than base metal Inconel 600 alloy and the crack initiates at the interface between HEA and Inconel 600.

Fourth, another HEA with a composition of  $\text{FeCoNi}(\text{AlSi})_{0.2}$  was fabricated by arc melting, showing a single FCC phase structure and a melting point of 1340 °C. The as-cast HEA was oxidized at 800 °C and 1000 °C for 6 hours. Oxidation layers were found on the surface of HEA. The 800 °C oxidation

layer has two sub-layers with different compositions. The outer layer with a thickness of 20  $\mu\text{m}$  is rich in Fe and O while the inner layer with a thickness of 20  $\mu\text{m}$  is rich in Al, Si, Co and Ni. The 1000  $^{\circ}\text{C}$  oxidation layer has three sub-layers with different compositions. The outer layer is rich in Fe, the middle layer is rich in Co while the inner layer is rich in Al and Si. Fe is oxidized first while Al and Si are oxidized at last. The 800  $^{\circ}\text{C}$  has a total thickness of 40  $\mu\text{m}$  while the 1000  $^{\circ}\text{C}$  has a total thickness larger than 100  $\mu\text{m}$ . The oxidized HEA, as-cast HEA and pure Fe were incorporated into aluminum at 700  $^{\circ}\text{C}$  for 1 hour. It was found the oxidized HEA has the best resistance to aluminum corrosion while pure Fe has the worst resistance to aluminum corrosion.

## CHAPTER 7

### FUTURE WORK

There are many opportunities to development and application of HEA filler foils for brazing of different types of metallic materials and ceramics.

#### **7.1 Development of new HEA fillers**

The HEA developed in this study has a melting range of 1080-1150 °C. However, in order to braze other types of Ni-base superalloys with lower melting point than Inconel 600 alloy, such as Inconel625, Inconel 718 and Rene 108, HEA filler with lower melting point than 1150 °C should be developed. Also because the filler should have comparable hardness with base metal and Inconel 625, 718, Rene 108 have higher hardness than Inconel 600, the hardness of the HEA filler should be increased as well.

#### **7.2 Development of new phase diagram calculation software**

Although the newly published database, HEA1.0 could provide more accurate phase diagram than previous database, the difference between calculated and experimental results still exists. More accurate phase diagram calculation software should be introduced into the design of HEA filler.

#### **7.3 Brazing of Ni-bas superalloys, ceramics or other alloys**

The HEA filler foil was used for brazing of Inconel 600 Ni-base superalloys in this study. However, more types of Ni-base superalloys such as Inconel 625, Inconel718, Rene 108 could also be brazed by HEA filler foil if the melting range and the hardness of HEA filler foil could be reasonably adjusted according to melting range and hardness of Ni-base superalloy. Moreover, HEA can also be used to braze ceramics to Ni-base superalloy, Stainless steel to Ni-base superalloy or titanium alloy to Ni-base superalloys.

#### **7.4 New method to test the shear strength of the brazed joint**

The shear strength of the brazed joint was successfully tested in this study. However, the deformation of the brazed joint used in this study is not pure shearing deformation, bending deformation has also been introduced into the brazed joint during test. In the future, a new fixture preventing the joint from bending or rotating should be designed and machined so that the brazed joint has only pure shearing deformation during test to get a more accurate value of shear strength. Micro DIC should also be used to measure the strain distribution.

### **7.5 Microstructure characterization of the brazed joint**

It is interesting to note that diffusion affected zone has the highest hardness value and the most complex distribution of elements. The mechanism of the formation of the diffusion affected zone should be investigated further. Outstanding questions include (1) whether the diffusion affected zone is from HEA or Inconel 600 alloy, (2) does it form from liquid state, and (3) what is the difference of strain distribution during shear test between diffusion affected zone and coarse grain zone.

### **7.6 Development of HEA nanoscale powder for brazing**

There is also another solution to reduce the melting point of HEA. Nanoscale HEA could be fabricated by laser radiation or powder metallurgy method. Nanoscale HEA powder with an average size of 100  $\mu\text{m}$  has a melting point 200  $^{\circ}\text{C}$  lower than bulk HEA. With the decrease of the melting point of the filler foil, the brazing temperature could be decreased, saving the heat and energy.

### **7.7 Development of mold materials for Al alloy casting**

The HEA with a composition of  $\text{FeCoNi}(\text{AlSi})_{0.2}$  shows better ability than traditional mold steel to prevent itself from the corrosion of aluminum melt. It is also found that the oxidation of HEA could further improve the resistance of HEA to corrosion of aluminum melt. The composition and the surface treatment parameters of HEA can still be optimized in order to achieve a better resistance to aluminum melt corrosion.

## REFERENCES

1. Yeh J W, Chen S K, Lin S J, et al. Nanostructured High-Entropy Alloys with Multiple Principal Elements: Novel Alloy Design Concepts and Outcomes [J]. *Advanced Engineering Materials*, 2004, 6(5): 299-303.
2. Cantor B. High-entropy alloys. In: Buschow KHJ, Cahn RW, Flemings MC, Ilschner B, Kramer EJ, Mahajan S, Veyssiere Peditors. *Encyclopedia of materials: science and technology*. ISBN 978-0-08 043152-9 (last update October 2011).
3. Zhou Y J, Zhang Y, Wang Y L, et al. Solid solution alloys of AlCoCrFeNiTix with excellent room-temperature mechanical properties[J]. *Applied physics letters*, 2007, 90(18): 1904.
4. Senkov ON, Wilks GB, Scott JM, Miracle DB. Mechanical properties of Nb<sub>25</sub>Mo<sub>25</sub>Ta<sub>25</sub>W<sub>25</sub> and V<sub>20</sub>Nb<sub>20</sub>Mo<sub>20</sub>Ta<sub>20</sub>W<sub>20</sub> refractory high entropy alloys, *Intermetallics* 2011,19:698–706.
5. Senkov O N, Wilks G B, Miracle D B, et al. Refractory high-entropy alloys [J]. *Intermetallics*, 2010, 18(9): 1758-1765.
6. Zhang Y. Mechanical properties and structures of high entropy alloys and bulk metallic glasses composites [C]. *Materials Science Forum*. 2010,654: 1058-1061.
7. Lin C M, Tsai H L. Evolution of microstructure, hardness, and corrosion properties of high-entropy Al<sub>0.5</sub>CoCrFeNi alloy [J]. *Intermetallics*, 2011, 19(3): 288-294.
8. Kennedy R L. ALLVAC® 718PLUS™, superalloy for the next forty years [J]. *Superalloys*, 2005, 718: 625-706.
9. Antony, K. C., and G. W. Goward. "Aircraft gas turbine blade and vane repair." *Superalloys The Metallurgical Society* (1988): 745.
10. Chen G, Zhang B, Lü T, et al. Causes and control of welding cracks in electron-beam-welded super-alloy GH4169 joints [J]. *Transactions of Nonferrous Metals Society of China*, 2013, 23(7): 1971-1976.
11. Kim D Y, Hwang J H, Kim K S et al. A study on fusion repair process for a precipitation hardened IN738 Ni-based super-alloy [C] ASME 1999 International Gas Turbine and Aeroengine Congress and Exhibition. American Society of Mechanical Engineers, 1999: V004T01A004-V004T01A004.
12. Ma G, Wu D, Niu F, et al. Microstructure evolution and mechanical property of pulsed laser welded Ni-based superalloy[J]. *Optics and Lasers in Engineering*, 2015, 72: 39-46.
13. Montazeri M, Ghaini F M, Ojo O A. Heat input and the liquation cracking of Laser welded IN738LC superalloy[J]. *Weld. J*, 2013, 92(9): 258s-264s.
14. Suharno A S, Buntario R E, Widagdo D, et al. Advantage of SWET Technique on Joining Inconel 792 Material [J]. *Global Journal of Researches In Engineering*, 2012, 12(6-A).
15. Shapiro A, Rabinkin A. State of the art of titanium-based brazing filler metals [J]. *Welding Journal*, 2003, 82(10): 36-43.
16. Huang, Xiao, and Warren Miglietti. "Wide gap braze repair of gas turbine blades and vanes—a review." *Journal of Engineering for Gas Turbines and Power* 134.1 (2012): 010801.
17. McDermid, J. R., M. D. Pugh, and R. A. L. Drew. "The interaction of reaction-bonded silicon carbide and Inconel 600 with a nickel-based brazing alloy." *Metallurgical Transactions A* 20.9 (1989): 1803-1810.
18. Laik, A., et al. "Microstructural evolution during reactive brazing of alumina to Inconel 600 using Ag-based alloy." *Acta Materialia* 61.1 (2013): 126-138.

19. Chang, S. Y., Y. T. Hung, and T. H. Chuang. "Joining alumina to Inconel 600 and UMCo-50 superalloys using an Sn10Ag4Ti active filler metal." *Journal of materials engineering and performance* 12.2 (2003): 123-127.
20. Chen, J. H., et al. "The metallurgical behaviour during brazing of Ni-base alloy Inconel 600 to Si<sub>3</sub>N<sub>4</sub> with Ag<sub>71</sub>Cu<sub>27</sub>Ti<sub>2</sub> filler metal." *Journal of materials science* 28.11 (1993): 2933-2942.
21. Zaharinie, Tuan, et al. "Effect of brazing temperature on the shear strength of Inconel 600 joint." *The International Journal of Advanced Manufacturing Technology* 73.5-8 (2014): 1133-1140.
22. Yan M, Fan Z. Review durability of materials in molten aluminum alloys[J]. *Journal of materials science*, 2001, 36(2): 285-295.
23. Yang H H, Tsai W T, Kuo J C. Effect of pre-oxidation on increasing resistance of Fe–Al–Ni–Cr–Co–Mn high entropy alloys to molten Al attack[J]. *Corrosion Engineering, Science and Technology*, 2014, 49(2): 124-129.
24. Yan M, Fan Z, Bevis M J. The erosion behaviour of Inconel 718 in molten A380 alloy[J]. *Scripta materialia*, 1999, 40(11): 1255-1261.
25. Barbier F, Manuelli D, Bouche K. Characterization of aluminide coatings formed on 1.4914 and 316L steels by hot-dipping in molten aluminium[J]. *Scripta materialia*, 1997, 36(4): 425-431.
26. Yan M, Fan Z. The erosion of H21 tool steel in molten A380 alloy[J]. *Journal of materials science*, 2000, 35(7): 1661-1667.
27. Yeh J W, Chen S K, Lin S J, et al. Nanostructured High-Entropy Alloys with Multiple Principal Elements: Novel Alloy Design Concepts and Outcomes[J]. *Advanced Engineering Materials*, 2004, 6(5): 299-303.
28. Cantor B. High-entropy alloys. In: Buschow KHJ, Cahn RW, Flemings MC, Ilschner B, Kramer EJ, Mahajan S, Veyssiere Peditors. *Encyclopedia of materials: science and technology*. ISBN 978-0-08 043152-9 (last update October 2011).
29. Zhou Y J, Zhang Y, Wang Y L, et al. Solid solution alloys of AlCoCrFeNiTi<sub>x</sub> with excellent room-temperature mechanical properties[J]. *Applied physics letters*, 2007, 90(18): 1904.
30. Senkov ON, Wilks GB, Scott JM, Miracle DB. Mechanical properties of Nb<sub>25</sub>Mo<sub>25</sub>Ta<sub>25</sub>W<sub>25</sub> and V<sub>20</sub>Nb<sub>20</sub>Mo<sub>20</sub>Ta<sub>20</sub>W<sub>20</sub> refractory HEAs, *Intermetallics* 2011,19:698–706.
31. Senkov O N, Wilks G B, Miracle D B, et al. Refractory high-entropy alloys[J]. *Intermetallics*, 2010, 18(9): 1758-1765.
32. Zhang Y. Mechanical properties and structures of HEAs and bulk metallic glasses composites [C]. *Materials Science Forum*. 2010,654: 1058-1061.
33. Lin C M, Tsai H L. Evolution of microstructure, hardness, and corrosion properties of high-entropy Al<sub>0.5</sub>CoCrFeNi alloy [J]. *Intermetallics*, 2011, 19(3): 288-294.
34. Ma S G, Zhang Y. Effect of Nb addition on the microstructure and properties of AlCoCrFeNi HEA [J]. *Materials Science and Engineering: A*, 2012, 532: 480-486.
35. Tang Z, Gao M C, Diao H, et al. Aluminum alloying effects on lattice types, microstructures, and mechanical behavior of high-entropy alloys systems [J]. *JOM*, 2013, 65(12): 1848-1858.
36. Zhou Y J, Zhang Y, Wang Y L, et al. Solid solution alloys of AlCoCrFeNiTi<sub>x</sub> with excellent room-temperature mechanical properties[J]. *Applied physics letters*, 2007, 90(18): 1904.

37. Hume-Rothery, W., 1967. Factors affecting the stability of metallic phases. In: Rudman, P.S., Stringer, J., Jaffee, R.I. (Eds.), *Phase Stability in Metals and Alloys*. McGraw-Hill, New York, NY.
38. Massalski, T. B. "Phase diagrams in materials science." *Metallurgical Transactions A* 20.8 (1989): 1295-1323.
39. Smith, W. F., and J. Hashemi. "Engineering alloys." *Foundations of Materials Science and Engineering* 4th ed., McGraw-Hill Book Company, New York (2006).
40. Darken, L.S., Gurry, R.W., 1953. *Physical Chemistry of Metals*. McGraw-Hill, New York, NY.
41. Fang, S. S., et al. "The maximum solid solubility of the transition metals in palladium." *International journal of hydrogen energy* 27.3 (2002): 329-332.
42. Gschneidner Jr., K.A., 1980. L. S (Larry) Darken's contributions to the theory of alloy formation and where we are today. In: Bennett, L.H. (Ed.), *Theory of Alloy Phase Formation*. The Metallurgical Society of AIME, Warrendale, pp. 1-39.
43. Miedema, A. R. "The electronegativity parameter for transition metals: heat of formation and charge transfer in alloys." *Journal of the less common metals* 32.1 (1973): 117-136.
44. Chelikowsky, J. R. "Solid solubilities in divalent alloys." *Physical Review B* 19.2 (1979): 686.
45. Alonso, J. A., and S. Simozar. "Prediction of solid solubility in alloys." *Physical Review B* 22.12 (1980): 5583.
46. Ranganathan, S., 2003. Alloyed pleasures: multimetallc cocktails. *Curr. Sci.* 85, 1404-1406.
47. Yeh, J-W., et al. "Nanostructured high-entropy alloys with multiple principal elements: novel alloy design concepts and outcomes." *Advanced Engineering Materials* 6.5 (2004): 299-303.
48. Tong, Chung-Jin, et al. "Microstructure characterization of Al<sub>x</sub>CoCrCuFeNi high-entropy alloy system with multiprincipal elements." *Metallurgical and Materials Transactions A* 36.4 (2005): 881-893.
49. Yeh, J.W., 2006. Recent progress in high-entropy alloys. *Ann. Chim. Sci. Mat.* 31, 633-648.
50. Zhang, Yong, et al. "Solid-solution phase formation rules for multi-component alloys." *Advanced Engineering Materials* 10.6 (2008): 534-538.
51. Takeuchi, Akira, et al. "Entropies in alloy design for high-entropy and bulk glassy alloys." *Entropy* 15.9 (2013): 3810-3821.
52. Zhang, Y., X. Yang, and P. K. Liaw. "Alloy design and properties optimization of high-entropy alloys." *Jom* 64.7 (2012): 830-838.
53. Yang, X., and Y. Zhang. "Prediction of high-entropy stabilized solid-solution in multi-component alloys." *Materials Chemistry and Physics* 132.2 (2012): 233-238.
54. Sheng, GUO, and Chain Tsuan LIU. "Phase stability in HEAs: formation of solid-solution phase or amorphous phase." *Progress in Natural Science: Materials International* 21.6 (2011): 433-446.
55. Guo, Sheng, et al. "More than entropy in high-entropy alloys: forming solid solutions or amorphous phase." *Intermetallics* 41 (2013): 96-103.
56. Ren, Ming-xing, Bang-sheng Li, and Heng-zhi Fu. "Formation condition of solid solution type high-entropy alloy." *Transactions of Nonferrous Metals Society of China* 23.4 (2013): 991-995.
57. Wang, F. J., Y. Zhang, and G. L. Chen. "Atomic packing efficiency and phase transition in a HEA." *Journal of Alloys and Compounds* 478.1 (2009): 321-324.

58. Raghavan, R., KC Hari Kumar, and B. S. Murty. "Analysis of phase formation in multi-component alloys." *Journal of Alloys and Compounds* 544 (2012): 152-158.
59. Bhatt, Jatin, et al. "Optimization of bulk metallic glass forming compositions in Zr–Cu–Al system by thermodynamic modeling." *Intermetallics* 15.5 (2007): 716-721.
60. Otto, Frederik, et al. "Relative effects of enthalpy and entropy on the phase stability of equiatomic high-entropy alloys." *Acta Materialia* 61.7 (2013): 2628-2638.
61. Sriharitha, R., B. S. Murty, and Ravi S. Kottada. "Phase formation in mechanically alloyed  $\text{Al}_x\text{CoCrCuFeNi}$  ( $x= 0.45, 1, 2.5, 5\text{mol}$ ) HEAs." *Intermetallics* 32 (2013): 119-126.
62. Pettifor, D.G., 1984. A chemical scale for crystal-structure maps. *Solid State Commun.*51, 31\_34.
63. Pettifor, D.G., 1988. Structure maps for pseudobinary and ternary phases. *Mater. Sci. Technol.* 4, 675\_691.
64. Jeevan, H. S., and S. Ranganathan. "A new basis for the classification of quasicrystals." *Journal of non-crystalline solids* 334 (2004): 184-189.
65. Biswas, Tripti, and Srinivasa Ranganathan. "Multicomponent alloys visualized as lower order alloys: Examples of quasicrystals and metallic glasses." *Annales de chimie*. Vol. 31. No. 6. Lavoisier, 2006.
66. Villars, P., Cenzual, K., Daama, J., Chen, Y., Iwata, S., 2004. Data-driven atomic environment prediction for binaries using the Mendeleev number: Part 1. Composition AB. *J. Alloys Compd.* 367, 167\_175.
67. Tsai, Che-Wei, et al. "Deformation and annealing behaviors of high-entropy alloy  $\text{Al}_{0.5}\text{CoCrFeNi}$ ". *Journal of Alloys and compounds* 486.1 (2009): 427-435.
68. Yeh J W, Chen Y L, Lin S J, et al. High-entropy alloys—a new era of exploitation[C]. *Materials Science Forum*. 2007, 560: 1-9.
69. Zhang Y, Zhou Y J, Lin J P, et al. Solid-solution phase formation rules for multi-component alloys[J]. *Advanced Engineering Materials*, 2008,10(6): 534-538.
70. Kaffuman, L., Cohen, M. (1956). "The martensitic transformation in the Fe-Ni system." *Trans.AIME* 206: 1393-1401
71. Muggianu, Y. M., et al. (1975). "Enthalpies of formation of liquid alloys bismuth-gallium-tin at 723k-choice of an analytical representation of integral and partial thermodynamic functions of mixing for this ternary-system." *Journal de Chimie Physique et de Physico-Chimie Biologique* 72(1): 83-88.
72. Palumbo, M. and L. Battezzati (2008). "Thermodynamics and kinetics of metallic amorphous phases in the framework of the CALPHAD approach." *Calphad* 32(2): 295-314.
73. Durga, A., et al. (2012). "Phase formation in equiatomic HEAs: Calphad approach and experimental studies." *Transactions of the Indian Institute of Metals* 65(4): 375-380.
74. Raghavan, R., et al. (2012). "Analysis of phase formation in multi-component alloys." *Journal of Alloys and Compounds* 544: 152-158.
75. Zhang, C., et al. (2012). "Computational thermodynamics aided high-entropy alloy design." *JOM* 64(7): 839-845.
76. Manzoni, A., et al. (2013). "Investigation of phases in  $\text{Al}_{23}\text{Co}_{15}\text{Cr}_{23}\text{Cu}_8\text{Fe}_{15}\text{Ni}_{16}$  and  $\text{Al}_8\text{Co}_{17}\text{Cr}_{17}\text{Cu}_8\text{Fe}_{17}\text{Ni}_{33}$  HEAs and comparison with equilibrium phases predicted by Thermo-Calc." *Journal of Alloys and Compounds* 552: 430-436.
77. Li, C., et al. (2008). "B2 structure of high-entropy alloys with addition of Al." *Journal of applied physics* 104(11): 113504.

78. Wang, S. Q. and H. Q. Ye (2011). First-principles studies on the component dependences of High-entropy alloys. *Advanced Materials Research*, Trans Tech Publ.
79. Tian, F., et al. (2013). "Ab initio investigation of high-entropy alloys of 3 d elements." *Physical Review B* 87(7): 075144.
80. Wei S H, Ferreira L G, Bernard J E, et al. Electronic properties of random alloys: Special quasirandom structures[J]. *Physical Review B*, 1990, 42(15): 9622.
81. Rowlands D A, Staunton J B, Györffy B L. Korringa-Kohn-Rostoker nonlocal coherent-potential approximation[J]. *Physical Review B*, 2003, 67(11): 115109.
82. Gao M C, Alman D E, Searching for next single-phase high-entropy alloy compositions [J]. *Entropy*, 2013, 15(10): 4504-4519.
83. Zhang C, Zhang F, Chen S et.al. Computational thermodynamics aided high-entropy alloy design [J]. *JOM*, 2012, 64(7): 839-845.
84. Kim K B, Warren P J, Cantor B, et al. Enhanced thermal stability of the devitrified nanoscale icosahedral phase in novel multicomponent amorphous alloys [J]. *Journal of materials research*, 2006, 21(04): 823-831.
85. Guo, Sheng, et al. "Effect of valence electron concentration on stability of fcc or bcc phase in HEAs." *Journal of applied physics* 109.10 (2011): 103505.
86. NONG, Zhi-sheng, et al. "First principles calculation of intermetallic compounds in FeTiCoNiVCrMnCuAl system HEA." *Transactions of Nonferrous Metals Society of China* 22.6 (2012): 1437-1444.
87. Jasiewicz, K., et al. "Superconductivity of Ta<sub>34</sub>Nb<sub>33</sub>Hf<sub>8</sub>Zr<sub>14</sub>Ti<sub>11</sub> HEA from first principles calculations." *physica status solidi (RRL)-Rapid Research Letters* 10.5 (2016): 415-419.
88. Wang, Shao Qing, and Heng Qiang Ye. "First-principles studies on the component dependences of High-entropy alloys." *Advanced Materials Research*. Vol. 338. Trans Tech Publications, 2011.
89. Shang, Shun-Li, Yi Wang, and Zi-Kui Liu. "Thermodynamic fluctuations between magnetic states from first-principles phonon calculations: The case of bcc Fe." *Physical Review B* 82.1 (2010): 014425.
90. Ma, Duancheng, et al. "Ab initio thermodynamics of the CoCrFeMnNi HEA: Importance of entropy contributions beyond the configurational one." *Acta Materialia* 100 (2015): 90-97.
91. Gao, Michael C., and David E. Alman. "Searching for next single-phase high-entropy alloy compositions." *Entropy* 15.10 (2013): 4504-4519.
92. Senkov O N, Zhang F, Miller J D. Phase composition of a CrMo<sub>0.5</sub>NbTa<sub>0.5</sub>TiZr HEA: Comparison of experimental and simulated data[J]. *Entropy*, 2013, 15(9): 3796-3809.
93. Ng C, Guo S, Luan J, et al. Entropy-driven phase stability and slow diffusion kinetics in an Al<sub>0.5</sub>CoCrFeNi alloy HEA[J]. *Intermetallics*, 2012, 31: 165-172.
94. Wang, Shaoqing. "Atomic structure modeling of multi-principal-element alloys by the principle of maximum entropy." *Entropy* 15.12 (2013): 5536-5548.
95. Kuznetsov A V, Shaysultanov D G, Stepanov N D, et al. Tensile properties of an AlCrCuNiFeCo high-entropy alloy in as-cast and wrought conditions[J]. *Materials Science and Engineering: A*, 2012, 533: 107-118.
96. Senkov O N, Wilks G B, Miracle D B, et al. Refractory high-entropy alloys[J]. *Intermetallics*, 2010, 18(9): 1758-1765.
97. Senkov O N, Wilks G B, Scott J M, et al. Mechanical properties of Nb<sub>25</sub>Mo<sub>25</sub>Ta<sub>25</sub>W<sub>25</sub> and V<sub>20</sub>Nb<sub>20</sub>Mo<sub>20</sub>Ta<sub>20</sub>W<sub>20</sub> refractory HEAs[J]. *Intermetallics*, 2011, 19(5): 698-706.

98. Senkov O N, Woodward C F. Microstructure and properties of a refractory NbCrMo<sub>0.5</sub>Ta<sub>0.5</sub>TiZr alloy[J]. *Materials Science and Engineering: A*, 2011, 529: 311-320.
99. Senkov O N, Scott J M, Senkova S V, et al. Microstructure and elevated temperature properties of a refractory TaNbHfZrTi alloy[J]. *Journal of Materials Science*, 2012, 47(9): 4062-4074.
100. Li, Xiaoqing, et al. "Ab initio-predicted micro-mechanical performance of refractory high-entropy alloys." *Scientific reports* 5 (2015).
101. Gludovatz B, Hohenwarter A, Catoor D, et al. A fracture-resistant high-entropy alloy for cryogenic applications[J]. *Science*, 2014, 345(6201): 1153-1158.
102. Qiao J W, Ma S G, Huang E W, et al. Microstructural characteristics and mechanical behaviors of AlCoCrFeNi high-entropy alloys at ambient and cryogenic temperatures[C]. *Materials Science Forum*. 2011,688: 419-425.
103. Laktionova M A, Tabchnikova E D, Tang Z, et al. Mechanical properties of the high-entropy alloy Al<sub>10</sub>.5CoCrCuFeNi at temperatures of 4.2–300 K[J]. *Low Temperature Physics*, 2013, 39(7): 630-632.
104. Hemphill M A, Yuan T, Wang G Y, et al. Fatigue behavior of Al 0.5 CoCrCuFeNi HEAs[J]. *Acta Materialia*, 2012, 60(16): 5723-5734.
105. Chuang M H, Tsai M H, Wang W R, et al. Microstructure and wear behavior of Al<sub>x</sub>Co<sub>1.5</sub>CrFeNi<sub>1.5</sub>Ti<sub>y</sub> high-entropy alloys[J]. *Acta Materialia*, 2011, 59(16): 6308-6317.
106. Wu J M, Lin S J, Yeh J W, et al. Adhesive wear behavior of Al<sub>x</sub>CoCrCuFeNi high-entropy alloys as a function of aluminum content[J]. *Wear*, 2006, 261(5): 513-519.
107. Schuh C A, Hufnagel T C, Ramamurty U. Mechanical behavior of amorphous alloys[J]. *Acta Materialia*, 2007, 55(12): 4067-4109.
108. Dahmen K, Ertas D, Ben-Zion Y. Gutenberg-Richter and characteristic earthquake behavior in simple mean-field models of heterogeneous faults[J]. *Physical Review E*, 1998, 58(2): 1494.
109. Ma S G, Zhang Y. Effect of Nb addition on the microstructure and properties of AlCoCrFeNi high-entropy alloy[J]. *Materials Science and Engineering: A*, 2012, 532: 480-486.
110. Wang X F, Zhang Y, Qiao Y, et al. Novel microstructure and properties of multicomponent CoCrCuFeNiTi<sub>x</sub> alloys[J]. *Intermetallics*, 2007, 15(3): 357-362.
111. Zhang K B, Fu Z Y, Zhang J Y, et al. Annealing on the structure and properties evolution of the CoCrFeNiCuAl high-entropy alloy[J]. *Journal of Alloys and Compounds*, 2010, 502(2): 295-299.
112. Chen S K, Kao Y F. Near-constant resistivity in 4.2-360 K in a B<sub>2</sub>Al<sub>2.08</sub>CoCrFeNi[J]. *AIP Advances*, 2012, 2(1): 012111.
113. Kao Y F, Chen S K, Sheu J H, et al. Hydrogen storage properties of multi-principal-component CoFeMnTi<sub>x</sub>V<sub>y</sub>Zr<sub>z</sub> alloys[J]. *international journal of hydrogen energy*, 2010, 35(17): 9046-9059.
114. Zhang Y, Zuo T T, Tang Z, et al. Microstructures and properties of high-entropy alloys[J]. *Progress in Materials Science*, 2014, 61: 1-93.
115. Poletti M G, Battezzati L. Electronic and thermodynamic criteria for the occurrence of HEAs in metallic systems[J]. *Acta Materialia*, 2014, 75: 297-306.
116. Singh, Sheela, et al. "Decomposition in multi-component AlCoCrCuFeNi high-entropy alloy." *Acta Materialia* 59.1 (2011): 182-190.
117. Ma, S. G., et al. "A successful synthesis of the CoCrFeNiAl<sub>0.3</sub> single-crystal, high-entropy alloy by Bridgman solidification." *JOM* 65.12 (2013): 1751-1758.

118. Feuerbacher, M., et al. "Single-crystal growth of a FeCoCrMnAl high-entropy alloy." *Materials Research Letters* (2016): 1-7.
119. Chen, Yu-Liang, et al. "Amorphization of equimolar alloys with HCP elements during mechanical alloying." *Journal of Alloys and Compounds* 506.1 (2010): 210-215.
120. Zhou, G. F., and H. Bakker. "Influence of mechanical milling on magnetic properties of intermetallic compounds (Overview)." *Materials Transactions, JIM* 36.2 (1995): 329-340.
121. Chang, Shou-Yi, et al. "Mechanical properties, deformation behaviors and interface adhesion of (AlCrTaTiZr)<sub>Nx</sub> multi-component coatings." *Surface and Coatings Technology* 204.20 (2010): 3307-3314.
122. Lin, Miao-I., et al. "Evolution of structure and properties of multi-component (AlCrTaTiZr)<sub>Ox</sub> films." *Thin Solid Films* 518.10 (2010): 2732-2737.
123. Zhang H, Pan Y, He Y, et al. Microstructure and properties of 6FeNiCoSiCrAlTi high-entropy alloy coating prepared by laser cladding [J]. *Applied Surface Science*, 2011, 257(6): 2259-2263.
124. Yao, Chen-Zhong, et al. "Electrochemical preparation and magnetic study of Bi-Fe-Co-Ni-Mn HEA." *Electrochimica Acta* 53.28 (2008): 8359-8365.
125. Qu Q, Xu J. Patent CN101554686-A.
126. Chen K, Xu J, Zhai Q. Patent CN101590574-A; CN101590574-B.
127. Chen S T, Tang W Y, Kuo Y F, et al. Microstructure and properties of age-hardenable Al<sub>x</sub>CrFe<sub>1.5</sub>MnNi<sub>0.5</sub> alloys[J]. *Materials Science and Engineering: A*, 2010, 527(21): 5818-5825.
128. Zhang Y, Zuo T T, Tang Z, et al. Microstructures and properties of high-entropy alloys[J]. *Progress in Materials Science*, 2014, 61: 1-93.
129. Qu Q, Xu J. Patent CN101554686-A.
130. Chen K, Xu J, Zhai Q. Patent CN101590574-A; CN101590574-B.
131. Chen S T, Tang W Y, Kuo Y F, et al. Microstructure and properties of age-hardenable Al<sub>x</sub>CrFe<sub>1.5</sub>MnNi<sub>0.5</sub> alloys[J]. *Materials Science and Engineering: A*, 2010, 527(21): 5818-5825.
132. Zhang Y, Zuo T T, Tang Z, et al. Microstructures and properties of high-entropy alloys[J]. *Progress in Materials Science*, 2014, 61: 1-93.
133. Kennedy R L. ALLVAC® 718PLUS™, superalloy for the next forty years[J]. *Superalloys*, 2005, 718: 625-706.
134. Muralidharan B G, Shankar V, Gill T P S, Weldability of Inconel 718-A review [R]. Indira Gandhi Centre for Atomic Research, 1996.
135. Lingenfelter A. Welding of Inconel alloy 718: A historical overview[J]. *Superalloy*, 1989, 718: 673-683.
136. Collier J P, Wong S H, Tien J K, et al. The effect of varying Al, Ti, and Nb content on the phase stability of INCONEL 718 [J]. *Metallurgical Transactions A*, 1988, 19(7): 1657-1666.
137. Furrer D, Fecht H. Ni-based superalloys for turbine discs[J]. *JOM*, 1999, 51(1): 14-17.
138. Chen G, Zhang B, Lü T, et al. Causes and control of welding cracks in electron-beam-welded super-alloy GH4169 joints [J]. *Transactions of Nonferrous Metals Society of China*, 2013, 23(7): 1971-1976.
139. Kim D Y, Hwang J H, Kim K S et al. A study on fusion repair process for a precipitation hardened IN738 Ni-based super-alloy [C] ASME 1999 International Gas Turbine and Aeroengine Congress and Exhibition. American Society of Mechanical Engineers, 1999: V004T01A004-V004T01A004.

140. Ma G, Wu D, Niu F, et al. Microstructure evolution and mechanical property of pulsed laser welded Ni-based superalloy[J]. *Optics and Lasers in Engineering*, 2015, 72: 39-46.
141. Montazeri M, Ghaini F M, Ojo O A. Heat input and the liquation cracking of Laser welded IN738LC superalloy[J]. *Weld. J*, 2013, 92(9): 258s-264s.
142. Suharno A S, Buntario R E, Widagdo D, et al. Advantage of SWET Technique on Joining Inconel 792 Material [J]. *Global Journal of Researches In Engineering*, 2012, 12(6-A).
143. Wang S. *Welding and Repair of Single Crystal Ni-based Superalloys*[D]. Carleton University Ottawa, 2005.
144. Shapiro A, Rabinkin A. State of the art of titanium-based brazing filler metals [J]. *Welding Journal*, 2003, 82(10): 36-43.
145. Zaharinie T, Yusof F, Hamdi M, et al. Effect of brazing temperature on the shear strength of Inconel 600 joint[J]. *The International Journal of Advanced Manufacturing Technology*, 2014, 73(5-8): 1133-1140.
146. Zaharinie T, Moshwan R, Yusof F, et al. Vacuum brazing of sapphire with Inconel 600 using Cu/Ni porous composite interlayer for gas pressure sensor application[J]. *Materials & Design*, 2014, 54: 375-381.
147. Chen J H, Wang G Z, Nogi K, et al. The metallurgical behaviour during brazing of Ni-base alloy Inconel 600 to Si<sub>3</sub>N<sub>4</sub> with Ag<sub>71</sub>Cu<sub>27</sub>Ti<sub>2</sub> filler metal[J]. *Journal of materials science*, 1993, 28(11): 2933-2942.
148. Miyazawa Y, Ariga T. Brazing of Inconel 600 and SUS304 stainless steel with used of rapidly solidified nickel-base brazing foil[J]. *Materials Transactions, JIM*, 1992, 33(5): 509-518.
149. Moore T J, Glasgow T K. Diffusion welding of MA 6000 and a conventional nickel-base superalloy[J]. 1985.
150. Chaturvedi M C, Ojo O. Diffusion brazing of cast inconel 738 superalloy[J]. *Advances in Technology of Materials and Materials Processing Journal(ATM)*, 2004.
151. Wu X, Chandel R S, Li H, et al. Induction brazing of Inconel 718 to Inconel X-750 using Ni–Cr–Si–B amorphous foil[J]. *Journal of materials processing technology*, 2000, 104(1): 34-43.
152. Yeh M S, Chuang T H. Effects of applied pressure on the brazing of superplastic INCONEL 718 superalloy[J]. *Metallurgical and Materials Transactions A*, 1997, 28(6): 1367-1376.
153. Chen W S, Shiue R K. Brazing Inconel 625 using two Ni/(Fe)-based amorphous filler foils[J]. *Metallurgical and Materials Transactions A*, 2012, 43(7): 2177-2182.
154. Ojo O A, Richards N L, Chaturvedi M C. Effect of gap size and process parameters on diffusion brazing of Inconel 738[J]. *Science and Technology of Welding & Joining*, 2013.
155. Xiong H P, Mao W, Xie Y H, et al. Brazing of SiC to a wrought nickel-based superalloy using CoFeNi (Si, B) CrTi filler metal[J]. *Materials Letters*, 2007, 61(25): 4662-4665.
156. Chen W S, Wang C Y, Shiue R K. Brazing Inconel 625 Using the Copper Foil [J]. *Metallurgical and Materials Transactions A*, 2013, 44(13): 5724-5731.
157. Zhang Y, Zuo T T, Cheng Y Q, et al. High-entropy alloys with high saturation magnetization, electrical resistivity, and malleability[J]. *Scientific reports*, 2013, 3.
158. Gali A, George E P. Tensile properties of high-and medium-entropy alloys[J]. *Intermetallics*, 2013, 39: 74-78.

APPENDIX A  
SUPPLEMENTAL ELECTRONIC FILES

Two videos are uploaded in order to show the strain distribution during shear test in the specimen brazed by Fe<sub>5</sub>Co<sub>20</sub>Ni<sub>20</sub>Mn<sub>35</sub>Cu<sub>20</sub> HEA with a thickness of 50μm for 15min (Video 1) and 60min (Video 2). Pictures in the video were taken every one second.

<b>Strain distribution files</b>	Files containing the strain distribution during the shear test of specimen brazed for different time. Both of the two files are in VLC media player format. Comparison of the two videos shows the effect of brazing time on the shear strength of the brazed joint.
Video 1.avi	Video shows the strain distribution during the shear test of the specimen brazed by 50μm HEA foil at 1200°C for 15min. It is included as part of these electronic supplementary files.
Video 2.avi	Video shows the strain distribution during the shear test of the specimen brazed by 50μm HEA foil at 1200°C for 15min. It is included as part of these electronic supplementary files.